NOTTINGHAM TRENT UNIVERSITY

Numerical Modelling for Detecting Delamination in Layered Waveguides

Jagdeep Singh Tamber

Supervisory team: Dr Matt Tranter and Dr David Chappell

A thesis submitted in partial fulfillment of the requirements for Doctor of Philosophy at Nottingham Trent University.

July 2025

Copyright statement

Abstract

The investigation into nonlinear bulk strain wave propagation within layered elastic waveguides offers numerous practical applications, notably in the domain of non-destructive testing. In situations where even a minor flaw in the bonding between waveguide layers can trigger a catastrophic structural failure, the utilisation of strain solitons in a waveguide of large domain holds significant promise in detecting a lack of bonding and structural fault. Experimental findings reveal that strain solitons propagate over considerably greater distances in comparison to the waves employed in existing methodologies, such as linear wave methods. In this thesis, we investigate the impact of delamination, the lack of bonding between structural layers, aiming to detect its presence and identify its location.

We consider three scattering problems. First, we study the scattering of a nonlinear bulk strain wave in a two-layered waveguide with a delaminated region 'sandwiched' between soft bonded regions, where soft bonding refers to weak adhesive contact. The lower layer is assumed to be much denser than the upper layer. The longitudinal displacement of the waves within this structure are modelled by a system of Boussinesq equations with continuity conditions at the interface. Given the complexity of the equations, we develop both direct numerical and semi-analytical methods, detailed in the appendices.

We vary the delamination length and analyse the phase shift of the wave packet in the second soft bonded region, comparing to the case of no delamination. Generally, across various small wave parameters, ε, as the delamination length increases so does the phase shift. We also use theoretical predictions, such as the linear dispersion relation, to validate the numerical simulation findings.

Next, we consider the same two-layered structure, but with layers made of different materials, but without a significant contrast in densities, resulting in distinct characteristic wave speeds in each layer. We model this by a system of coupled Boussinesq equations. We vary the delamination length and analyse the leading wave packet in the

second soft bonded region, which is easier to locate. Examining various soft bonded region lengths, we find that increasing the delamination length generally causes a phase shift to increase/decrease in correlation. These results allow us to determine the delamination length solely based on the observed phase shift, even without prior knowledge of the structure configuration.

The final structures that we considered were an n-layered waveguide with delamination between perfectly bonded regions, and a two-layered waveguide with delamination between soft bonded regions. As with the other structures, we vary the delamination length but focus on the change in amplitude of the leading wave peak. For the perfectly bonded case, we introduced a measure comparing the wave peak to the theoretical prediction of the Inverse Scattering Transform. In the soft bonded region, a similar measure was used, but only with the leading wave packet from the first and second soft bonded region. We observe that increasing the delamination length results in a decrease in wave amplitude.

Acknowledgements

Firstly, I extend my sincere gratitude to my lead supervisor, Matt Tranter, for his invaluable advice and unwavering encouragement throughout my academic journey, from my BSc and MRes to my PhD. His approach to research has not only inspired me but also propelled me to think innovatively in pursuit of my own research goals. Without his guidance, the accomplishment of this PhD would have been an unattainable feat.

I express my heartfelt appreciation to my secondary supervisor, David Chappell, for his insightful comments and engaging discussions during our regular supervisory meetings. David's expertise in linear waves brought a unique perspective to nonlinear waves.

I am grateful to the faculty members and fellow research students within the Department of Physics and Mathematics, notably Tuan Bohoran, Suliman Almansour, Rob Lockett, David Jenkins, and Iain Pinder, whose invaluable assistance within the office has been truly instrumental.

Finally, my deepest gratitude goes to my parents, whose unwavering support has been the cornerstone of my journey. Their belief in me has been the driving force behind this endeavour, and I owe the realisation of this work to their encouragement and devotion.

Declarations

I hereby declare that this thesis is my original work and has not been submitted for any other academic degree or professional certification. I confirm that all content is my own, except where contributions from jointly authored publications have been incorporated.

The results of this thesis are partially summarised in the following papers:

1. J.S. Tamber and M.R. Tranter. *Scattering of an Ostrovsky wave packet in a delaminated waveguide.* Wave Motion, 114:103023, 07 (2022).
   (This work relates to Chapter 3).

2. J.S. Tamber and M.R. Tranter. *Studying the effect of delamination on Ostrovsky wave packet propagation in waveguides.* Journal of Physics: Conference Series, 2647:252019 (2024).
   (This work relates to Chapter 3).

3. J.S. Tamber, D.J. Chappell, J.C. Poore, and M.R. Tranter. *Detecting delamination via nonlinear wave scattering in a bonded elastic bar.* Nonlinear Dynamics, 112:023033 (2024).
   (This work relates to Chapter 5).

4. J.S. Tamber, D.J. Chappell, and M.R. Tranter. *Delamination Detection via Ostrovsky Wave Packets in Layered Waveguides.* Proceedings of the Royal Society A: Mathematical, Physical and Engineering Sciences, 481:20240574 (2025).
   (This work relates to Chapter 4).

Abbreviations

BKG	Boussinesq-Klein-Gordon
cKG	coupled Klein-Gordon
cRB	coupled Regularised Boussinesq
DDE	Doubly Dispersive Equation
DFFT	Discrete Fast Fourier Transform
DFT	Discrete Fourier Transform
FFT	Fast Fourier Transform
FPU	Fermi-Pasta-Ulam
FWHM	Full Width at Half Magnitude
IDFT	Inverse Discrete Fourier Transform
IST	Inverse Scattering Transform
IVP	Initial-Value Problem
KdV	Korteweg-de Vries
NLS	Nonlinear Schrödinger
PDE	Partial Differential Equation
PMMA	Polymethylmethacrylate

Contents

Chapter 1

Introduction

1.1 Historical background

Solitons, or a solitary waves, are stable waves that maintain their form and energy during propagation. They were first observed by Scottish mathematician, John Scott Russell, in 1834 [1]. Russell's encounter with what he termed the 'great wave of translation' birthed the modern theory of solitons [2].

Driven by curiosity, Russell began a mathematical investigation into the nature of solitons. To deepen his understanding of them he constructed wave tanks within his home. Russell observed the exceptional stability and the ability to traverse long distances, which differed from conventional waves. Another revelation was that in stark contrast to nonlinear waves, solitons would neither merge nor superimpose. Rather, waves of lower amplitude would be overtaken by waves of higher amplitude, instead of combining together. Russell observed the velocity of these waves is largely determined by their width and the depth of the water [3].

Russell's findings were met with scepticism due to their contradiction with established hydrodynamic theories. Nevertheless, Russell deducing that the wave's total volume and the displaced water's volume being equivalent, remained a focal point. Crucially, he derived an equation for the speed, c, of solitary waves as follows:

$$c^2 = g(h + a), \tag{1.1}$$

where a represents the wave's amplitude, h signifies the water depth, and g denotes gravitational acceleration [4]. This relationship founded a pivotal observation that waves of higher amplitude propagate faster than waves of lower amplitude.

Russell's ideas led to the development of mathematical models for this phenomenon. French math-

ematician Joseph Valentine Boussinesq presented the first explicit derivations in 1872 and 1877 [5, 6], followed closely by the work of British scientist Lord Rayleigh [7].

Both Boussinesq and Rayleigh made the assumption that the horizontal length scale of the solitary wave far exceeds the depth of the water, an assumption derived from the shallow water equations [8]. Using equations of motion for an inviscid, incompressible fluid, they derived the formula for wave speed in line with Russell's concept. They denoted the profile of these solitary waves as $z = \zeta(x,t)$ at position x and time t expressed as

$$\zeta(x,t) = a \operatorname{sech}^2(\beta(x-ct)). \tag{1.2}$$

The constant β is defined via

$$\frac{1}{\beta^2} = \frac{4h^2(h+a)}{3a}, \tag{1.3}$$

where $\frac{a}{h} \ll 1$ is assumed. Boussinesq and Rayleigh however could not find a straightforward equation for $\zeta(x,t)$ that yielded the solution (1.2). However, in 1895, mathematicians Kortweg and de Vries formulated a nonlinear partial differential equation (PDE) whose solution mirrored the profile in equation (1.2). This equation is known as the Korteweg-de Vries (KdV) equation, which can be formulated as

$$u_t - 6uu_x + u_{xxx} = 0. \tag{1.4}$$

The KdV equation has been derived within many different contexts, including from the Fermi-Pasta-Ulam (FPU) lattice model [9]. Enrico Fermi, John Pasta and Stan Ulam decided to study the rate at which a system comprised of multiple particles attains thermal equilibrium. The FPU problem, also referred to as the Fermi-Pasta-Ulam-Tsingou problem acknowledging the numerical work of computer programmer Mary Tsingou (now Mary T. Menzel) [10], was first written up in a Los Alamos report in May 1955, and marked a new development in nonlinear physics.

In 1965, Zabusky and Kruskal were motivated by the FPU lattice model's lack of equipartition of energy among harmonic modes and thus explored the long-wave approximation, resulting in a re-derivation of the Boussinesq and KdV equations for solid mechanics [11]. They explicitly solved the KdV equation

$$u_t + uu_x + \delta^2 u_{xxx} = 0 \tag{1.5}$$

for $\delta = 0.022$ and the initial condition $u(x,0) = \cos(\pi x)$. Initially, the dispersive term is small, thus placing primary emphasis on the nonlinear term's effect and leading to the emergence of a discontinuity at $t = t_b = 1/\pi$. They demonstrated the emergence of solitons through a cosine initial condition, generating multiple solitons for this specific value of $\delta^2 = 0.022^2$. Their study showed that the interaction of solitons

is an elastic process where, post-interaction, the amplitude remains constant, and a phase shift occurs, rather than the amplitude changing. This phenomenon is known as 'recurrence' where solitons converge at a common point, almost reconstructing the initial condition. Furthermore, their investigation showed that with the subsequent recurrences, the precision of the reconstruction tended to diminish compared to the initial recurrence.

In 1967, Gardner, Green, Kruskal, and Miura developed the Inverse Scattering Transform (IST) for the KdV equation [12] and importantly, the IST offers a method to solve a large class of initial-value problems on the infinite line. These models possess useful mathematical properties, such as infinitely many conservation laws and compatibility conditions known as the Lax pair [13], which, within the theory of integrable systems and functional analysis, refers to a pair of time-dependent operators satisfying a corresponding differential equation termed the Lax equation. A restriction to the Hilbert space of square-integrable functions, $L^2(\mathbb{R})$ [14], enables us to rewrite the KdV equation as the following Lax's equation:

$$\frac{\mathrm{d}L}{\mathrm{d}t} = L_t = [P, L] = PL - LP. \tag{1.6}$$

Here, $[P, L]$ denotes the commutator, with the operators L and P denoted as

$$L = -\frac{\partial^2}{\partial x^2} + u, \quad P = -4\frac{\partial^3}{\partial x^3} + 6u\frac{\partial}{\partial x} + 3u_x. \tag{1.7}$$

Thus, the KdV equation possesses a Lax pair and infinitely many conservation laws, which together establish its integrability.

Subsequent extensions by Zakharov and Shabat in 1972 [15] provided a method to solve the Nonlinear Schrödinger (NLS) equation. In 1974, Ablowitz, Kaup, Newell, and Segur [16] suggested a more general scheme which solved the KdV and NLS equations and by extension this solved a broader class of equations, including the sine-Gordon equation, which had established a foundation for the study of integrable systems. This integrability was previously identified due to Albert Backlund's investigation on surfaces with consistently negative Gaussian curvature in the 19th century [17]. Since then, the integrability of many other PDEs, such as the Boussinesq and KdV equations, has been deduced in both singular and multi-dimensional spatial frameworks, as well as the derivation of corresponding soliton solutions [18].

In 1967, Toda introduced another lattice model involving a chain of particles with exponential interaction potentials, revealing the emergence of exact soliton solutions [19]. Stable envelope solitons are crucial to the behaviour of a modified Toda lattice that includes an additional linear term [20]. This modified lattice is linked to the two-directional generalisation of the Ostrovsky equation, which was introduced by Ostrovsky in 1978 to model oceanic waves influenced by Earth's rotation, and further explored in [21].

The Ostrovsky equation is given by

$$(u_t + uu_x + u_{xxx})_x = \gamma u, \tag{1.8}$$

where γ represents the strength of rotational effects [22, 23]. This equation is typically used to account for the background rotation of the Earth and the influence of shear flow in oceanic wave dynamics. In oceanographic scenarios (where $u > 0$), the presence of rotation eliminates the solitary wave solutions of the KdV equation due to terminal radiation damping [24, 25]. Numerical simulations have revealed that a stable localised wave packet becomes the dominant solution in the Ostrovsky equation [26, 27]. Employing a modified Toda lattice with an added linear elastic term [20] portrays the behaviour of a solid waveguide on an elastic foundation.

The weakly-nonlinear description of the emerging wave packet in the Ostrovsky equation as a higher-order NLS equation has been developed in [26] establishing a connection between the carrier wave's wavenumber and the group velocity's maximum [20, 26].

In 2007, Karima Khusnutdinova formulated a model of coupled Klein–Gordon (cKG) chains and their respective equations to represent long longitudinal waves in two-layers characterised by nonlinearity stemming solely from the bonding material [28]. In 2009, Khusnutdinova et al. examined a lattice model within layered elastic waveguides featuring soft bonding between layers [29]. The pivotal aspect of this model is that it relies on a complex chain of oscillating mechanical dipoles, which was previously considered in a linear context [28]. This model represents a natural extension of prior linear [30] and nonlinear [31] models. By deriving a system of coupled Boussinesq-type equations, an accurate asymptotic model was obtained from this complex chain. This model accounts for the essential degrees of freedom for the elastic waveguide, capturing both geometrical and physical sources of nonlinearity.

In conclusion, the Boussinesq and KdV equations, originating from fluid dynamics, have found applications in the study of nonlinear waves in solid systems. Solitons and tools such as the IST have improved our understanding of wave behaviour. Their behaviour in layered structures continues to provide valuable insights in nonlinear dynamics and material properties.

1.2 Applications

Wave propagation in solid materials holds significant relevance in modern applications, as demonstrated by various studies [32–39]. For instance, when bonding two PMMA waveguides using cyanoacrylate adhesive, the propagation of long longitudinal bulk strain solitary waves in elastic waveguides, can be effectively modelled using Boussinesq-type equations [22, 32, 33], despite these equations being typically

associated with fluid mechanics [36, 40–44]. Bulk strain solitons have demonstrated stability in layered waveguides with delamination, thus making them an effective tool for inspecting such structures alongside existing methods [45–49]. Analysing waveguides using linear waves can be problematic due to their limited range, requiring the use of exceedingly complex imaging techniques to capture specific behaviours. Nonlinear waves, on the other hand, offer a broader range of observation, thus identifying delamination more effectively [50]. The study of nonlinear waves has grown rapidly in recent years, finding promising applications in fluid and solid mechanics, mathematical biology, nonlinear optics, and various other fields [51–56]. Namely, solitary waves frequently emerge as solutions to nonlinear equations, such as the KdV equation in shallow water dynamics [52, 53, 57, 58]. They are also found in the Benjamin-Ono equation, which describes internal waves in stratified fluids [59, 60], the nonlinear Schrödinger equation governing optical phenomena [61, 62], and in the context of flexural waves described by the beam equation [63], among others.

Layered structures, employed in industry, heavily rely on the integrity of their bonding. Inadequate bonding or the occurrence of delamination, i.e. the absence of bonding, within waveguides such as rods, bars, shells, and plates can cause an entire structure to collapse, presenting significant risks. For instance, gas pipes often feature a protective layer that is welded on; however, if delamination is present between the gas pipe and protective layer, then this can lead to gas leaking [64]. Similarly, aeroplane wings with delamination could potentially detach during flight [65]. Thus, theoretical insights and imaging techniques on waveguides are crucial for the early detection of delamination within protective layering. This is particularly pivotal for ensuring the absence of delamination, as theoretical findings serve as valuable guides for practical experiments [44,46,66]. An experiment that provided an important perspective for observing nonlinear wave behaviour within layered structures involved the laser generation of a compression solitary wave with holographic interferomentry logging the wave pattern [44]. These practical experiments aim to capture the propagation of waves, such as solitons, within layered waveguides with the aim of confirming theoretical findings [67, 68].

The dynamic behaviour of layered structures depends on both the material of the layers and the type of the bonding between them. In scenarios where the bonding between the layers is sufficiently soft and the material of the layers are similar, the bulk strain solitons are replaced by radiating solitary waves, which are solitary waves with a one-sided, co-propagating oscillatory tail [29, 46, 48]. As these radiating solitary waves contain a co-propagating oscillatory tail, theoretical estimates of this tail can be formulated [69]. The longitudinal displacement of the waves is modeled by a system of coupled Boussinesq equations. Two numerical schemes are applied to understand how these waves propagate in layered waveguides with varying densities and bondings: a finite difference method, detailed in Appendix A, and a semi-

analytical scheme, outlined in Appendix B. Conversely, when the layer materials are distinctly different, the propagating waves become Ostrovsky wave packets instead of bulk strain solitons [48], which are described by the Ostrovsky equation (1.8). The evolution of wave packets originating from initial pulses has been extensively examined by Grimshaw and Helfrich [26, 70]. The longitudinal displacement is modelled by uncoupled Boussinesq equations in this case and, similarly as mentioned for the radiating solitary waves case, numerical methods are used to gain an understanding of the wave propagation. These two cases are outlined in Section 2.3.5. However, many other structure configurations are explored within this thesis.

In summary, layered structures are highly important in industrial applications where delamination can lead to severe consequences. Nonlinear waves, observed within these structures experimentally, can be used to detect structural faults. The propagation of the wave packet within the waveguide depends on the type of bonding and density of the layers.

1.3 Structure of thesis

In this thesis, we will explore the behaviour of long longitudinal bulk strain waves, focusing on wave amplitude, speed, and position, in multi-layered structures with various bonding types and configurations. Using two numerical approaches, a finite difference method and a semi-analytical scheme, we will analyse how variations in bonding affect wave propagation, with the aim of detecting delamination. In Chapter 2, we will review the existing literature in the area by examining historical cases. In the first case, we will focus on a single elastic waveguide, using nonlinear elasticity theory to derive a Boussinesq equation for the longitudinal displacement of waves [29, 45]. We will then construct a weakly-nonlinear solution to obtain leading order solutions and initial conditions. The second case will examine a two-layered waveguide with perfect bonding on the left and delamination on the right [47, 71]. Using nonlinear elasticity theory, we will derive a Boussinesq-type equation for the longitudinal displacement of waves for each section of the structure, rather than a single Boussinesq equation as in the single waveguide case. We will then establish equations governing the leading order propagation of waves in both directions for each region, along with the initial conditions, and derive the continuity conditions specifically at the boundary between the bonded and delaminated regions. In the third case, we will consider an initial-value problem for coupled Boussinesq equations and explicitly show how they are derived from a coupled Klein-Gordon chain model and a coupled Fermi-Pasta-Ulam chain model [72, 73]. We will then derive the dispersion relation for a symmetric case and, for a scattering problem involving coupled Boussinesq equations, establish the leading order equations describing left and right propagating waves in each layer of the structure.

In Chapter 3, we will examine a two-layered structure consisting of an initial delaminated region, followed by a soft bonded region, then a second delaminated region, and finally a second soft bonded region. The characteristic wave speeds in the two layers differ substantially, due to the significantly greater density of the lower layer compared to the upper one, hence, our focus will be on wave propagation in the upper layer. We will develop weakly-nonlinear solutions to derive the leading order transmitted and reflected strain waves, which are described by KdV equations in the delaminated regions and Ostrovsky equations in the soft bonded region, while also deriving the initial and continuity conditions [48]. We will outline the numerical schemes from Appendices A and B and perform simulations, expecting strong agreement between the methods. In the soft bonded region, we anticipate the leading peak will form an Ostrovsky wave packet, while in the delaminated region, it should evolve into a leading solitary wave with secondary solitons and some radiation. We will then obtain theoretical predictions for wave speed and amplitude using the IST method and the linear dispersion relation, aiming for strong agreement with the simulations. Next, we will compare structures with varying delamination lengths to a fully bonded structure, examining two aspects: one focusing on wave amplitude, using the leading wave peak, and the other on phase shift, with the front of the wave packet as a reference point. This approach allows us to estimate the delamination length without needing prior knowledge of its exact value. For the amplitude, we anticipate a percentage decrease as the delamination length increases, consistent with observations in [48]. The final part of our analysis in this chapter will involve simulations using experimental parameters for the waveguide's properties and geometry, aiming to gain insights into anticipated real-world behaviour. We expect to observe an Ostrovsky wave packet in the soft bonded region and solitons in the delaminated region, consistent with findings in this chapter and prior studies, though not be fully separated as a smaller bar may be being used due to the experimental geometry [45, 72].

Next, in Chapter 4, we now examine a structure similar to that in Chapter 3, but with a less dense lower layer. This lower layer will have a characteristic wave speed c, while the wave speed in the upper layer remains $c = 1$, so the characteristic speed difference will be $c - 1 = \mathcal{O}(1)$. As before, we will develop weakly-nonlinear solutions to derive the leading order strain waves and establish continuity conditions, now applied to each layer individually. Numerical simulations using the schemes outlined in Appendices A and B will be performed again, and we expect good agreement between the methods. However, the waves in the lower layer are anticipated to evolve more slowly than those in the upper layer due to its higher wave speed. Next, we will use the IST method to obtain theoretical predictions for the wave amplitude, and the linear dispersion relation to predict the wave speed, both for the lower layer, considering various c values. We expect strong alignment between these theoretical predictions and the simulation results [74]. Building on the analysis from Chapter 3, which focused on the phase shift of waves in delaminated structures by

varying the delamination length (using the front of the wave packet as a reference point), we will now extend the analysis to include both the delamination length and position, using the leading wave peak as the reference point. This approach, to our knowledge, has not been explored in previous literature. By using phase shift plots, we will aim to identify a common delamination length and position in both layers for arbitrary phase shift values, allowing us to estimate the delamination length and position without prior knowledge of these values. This analysis will be further extended by considering varying c values in the lower layer. We will also examine waves propagating right-to-left in the upper layer and compare them to left-to-right propagation. Similarly to the lower layer, we will determine a common delamination length and location for both propagation scenarios for a set of phase shift values. This approach will provide an additional tool for detecting delamination and its location within a structure. To conclude, we will briefly examine the positions of the leading wave peak and the front of the wave packet for structures of varying delamination lengths, confirming the forward motion of the overall wave packet as reiterated in the literature [75].

In Chapter 5, we will examine wave behaviour within two distinct multi-layered structures. The first multi-layered structure consists of a delaminated region 'sandwiched' between perfectly bonded regions. This configuration can extend to any number of layers, as each layer is made of the same material. The second structure is similar to that in Chapter 4, but here both layers are of similar materials. For both structures, we will construct weakly-nonlinear solutions and establish the initial conditions, following the approach of previous chapters. For the structure with perfect bonding, we will employ the IST method to predict the wave amplitude. However, for the soft bonded structure, the leading order equations are expected to be described by coupled Ostrovsky equations [76], which do not permit the application of the IST method. For the structure with perfect bonding, we will define a measure based on the simulated wave amplitudes in the two bonded regions and the predicted amplitude in the second bonded region. This measure will allow us to study the impact of various parameters, including delamination lengths, incident soliton widths (measured as Full Width at Half Maximum, or FWHM), and different waveguide configurations and geometries. Similar analysis was conducted in [77], where, as the delamination length increased, the measure approached a theoretical limit representing the maximum relative change in wave amplitude between the bonded regions, although the progression was nonlinear. For the soft bonded structure, we will apply a similar process without using the IST method, instead basing our measure on the wave amplitudes in the first and third bonded regions. We will then scale this measure to achieve overlap across all FWHM curves, allowing us to derive results for a single FWHM and then use scaling to extrapolate findings for other FWHM cases. Finally, we will scale our Boussinesq equations to a dimensional form, using experimental data parameters to provide estimates for practical delamination

lengths in real-world applications.

In Chapter 6, we will summarise the results from previous chapters and discuss possible future work that could improve and extend the analysis conducted in this thesis.

In Appendix A, we apply a finite difference method to numerically solve a single Boussinesq equation, then extend this approach to an initial value problem for a system of M coupled Boussinesq equations. In Appendix B, we use a pseudospectral scheme to solve the KdV, single Ostrovsky, and coupled Ostrovsky equations numerically.

Chapter 2

Propagation of nonlinear waves in waveguides

This chapter will review existing work and foundational concepts that inform the research developed in Chapters 3 – 5. It will not present original contributions but will provide essential context and highlight key gaps addressed in later chapters.

In this chapter we will discuss three problems. Firstly, in Section 2.1 we discuss a scattering problem for a single elastic waveguide, which will involve deriving a Boussinesq equation that describes the longitudinal displacements within the waveguide using nonlinear elasticity theory [45]. We will then consider a weakly-nonlinear solution and derive its leading order solutions including appropriate initial conditions.

Next, in Section 2.2 we will review a two-layered waveguide with delamination on the right and bonding on the left. We will again use nonlinear elasticity theory and derive the leading order weakly-nonlinear solutions [47].

Finally, in Section 2.3 we will explore two different lattice models, starting with coupled Klein-Gordon (cKG) chains to derive cKG equations [29, 72, 78] and then a coupled FPU model to derive coupled regularised Boussinesq (cRB) equations. We will then consider the symmetric case of these equations to understand the asymptotic behaviour of the dispersion relation. Following that, we derive the weakly-nonlinear solution as before but for different characteristic speeds resulting in coupled Ostrovsky equations.

2.1 Single elastic waveguide

In this section, we will be considering the elastic waveguide displayed in Figure 2.1. Firstly, we will use nonlinear elasticity theory to derive the respective doubly dispersive equation (DDE), which is an equation of Boussinesq type with two kinds of dispersive terms [45] describing the long longitudinal displacements in the waveguide. Then, considering the Boussinesq equation, we derive leading order equations described by the KdV equation using a weakly-nonlinear solution. Finally, we find the respective initial conditions for the derived KdV equations.

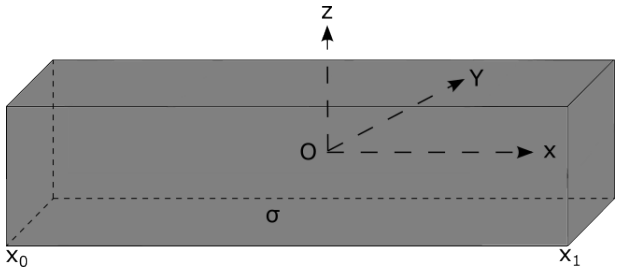

Figure 2.1: Elastic bar of rectangular cross section

2.1.1 Nonlinear elasticity theory

We consider long longitudinal bulk solitary waves in a single elastic waveguide of rectangular cross section $\sigma = \{-a \leq y \leq a; -b \leq z \leq b\}$, that are governed by the DDE. We denote the Lagrangian Cartesian coordinates (x, y, z), where the origin O is positioned along the bar at the centre of the cross-section σ and we assume the bar is in the initial equilibrium state. Here, x represents the position along the bar in the interval $[x_0, x_1]$, where x_0 is the starting point and x_1 is the ending point, and t represents the time. We study the problem in the scheme of nonlinear dynamic elasticity with the functional S expressed as

$$S = \int_{t_0}^{t_1} \mathcal{L}\left(U, U_t, U_x, ..., x, t\right) \mathrm{d}\Omega \mathrm{d}t, \tag{2.1}$$

where $\mathcal{L}(U, U_t, U_x, ..., x, t)$ is the Lagrangian density per unit volume, t is time, Ω is a space domain occupied by the waveguide, and $U = \{u, v, w\}$ is the displacement vector confined in the Lagrangian Cartesian coordinates (x, y, z) [32]. We denote the Lagrangian density $\mathcal{L}$ written in material variables as

$$\mathcal{L} = K - \Pi = \frac{\rho}{2}\left(\frac{\partial \mathrm{U}}{\partial t}\right)^2 - \rho\Pi(I_k), \tag{2.2}$$

where K is the kinetic energy density, Π is the density of potential energy, ρ is the density, and $I_k = I_k(\mathrm{C})$ are the invariants of Cauchy-Green deformation tensor [79]

$$\mathrm{C} = \frac{\nabla U + (\nabla U)^T + \nabla U \cdot (\nabla U)^T}{2}. \tag{2.3}$$

The invariants are explicitly written as

$$I_1 = \mathrm{tr}(\mathrm{C}), \quad I_2 = \frac{(\mathrm{tr}(\mathrm{C}))^2 - \mathrm{tr}(\mathrm{C}^2)}{2}, \quad I_3 = \det(\mathrm{C}). \tag{2.4}$$

We use the Murnaghan's model for Π [80] and the following energy expansion up to the 5-constant approximation

$$\Pi = \frac{(\lambda + 2\mu)I_1^2}{2} - 2\mu I_2 + \frac{(l + 2m)I_1^3}{3} - 2mI_1I_2 + nI_3 + ... \tag{2.5}$$

to consider the compressible isotropic nonlinearly elastic materials where λ and μ are Lame's coefficients, two material-dependent quantities that emerge in strain-stress relationships, and l, m, n are Murnaghan's moduli [80,81]. To simplify the problem to a nonlinear equation for the longitudinal displacement we shall use the planar cross-section hypothesis and the approximate relations for the transverse displacements via the linear longitudinal strain component as

$$u \approx u(x,t), \quad v \approx -y\nu u_x, \quad w \approx -z\nu u_x, \tag{2.6}$$

where

$$\nu = \frac{\lambda}{2(\lambda + \mu)}, \tag{2.7}$$

is Poisson's ratio [82, 83]. A cylindrical rod with a circular cross-section has similar relation [84, 85]. K and Π can be simplified using the relations (2.6) giving the approximate expressions of the invariants valid for the small amplitude long longitudinal elastic waves as

$$K = \frac{\rho}{2}\left(u_t^2 + v_t^2 + w_t^2\right) = \frac{\rho}{2}\left[u_t^2 + (y^2 + z^2)\nu^2 u_{xt}^2\right] + ..., \tag{2.8}$$

and

$$\Pi = \frac{1}{2}\left(Eu_x^2 + \frac{\beta}{3}u_x^3 + \mu\nu^2(y^2 + z^2)u_{xx}^2\right) + ..., \tag{2.9}$$

where the nonlinear coefficient

$$\beta = 3E + 2l(1 - 2\nu)^3 + 4m(1 + \nu)^2(1 - 2\nu) + 6n\nu^2, \tag{2.10}$$

depends on Murnaghan's moduli l, m, n, Young's modulus $E = \mu(3\lambda + 2\mu)/(\lambda + \mu)$, and Posson's ratio ν. Utilising (2.1) and (2.2) we express the Euler-Lagrange equation as

$$\frac{\partial \mathcal{L}_\sigma}{\partial u} - \left(\frac{\partial}{\partial t}\frac{\partial \mathcal{L}_\sigma}{\partial u_t} + \frac{\partial}{\partial x}\frac{\partial \mathcal{L}_\sigma}{\partial u_x} \right) + \frac{\partial^2}{\partial x^2}\frac{\partial \mathcal{L}_\sigma}{\partial u_{xx}} + \frac{\partial^2}{\partial x \partial t}\frac{\partial \mathcal{L}_\sigma}{\partial u_{xt}} + ... = 0, \tag{2.11}$$

where $\mathcal{L}_\sigma = \int_\sigma \mathcal{L} \mathrm{d}\sigma$ is the Lagrangian density per unit length. Substituting the expressions of (2.8) and (2.9) into the integral of (2.2) with respect to σ gives

$$\mathcal{L}_\sigma = \frac{1}{2}\int_\sigma \rho \left[u_t^2 + (y^2 + z^2)\nu^2 u_{xt}^2 \right] + \left(E u_x^2 + \frac{\beta}{3}u_x^3 + \mu\nu^2(y^2 + z^2)u_{xx}^2 \right) + ... \, \mathrm{d}\rho. \tag{2.12}$$

Substituting this expression into (2.11) produces the DDE for long nonlinear longitudinal displacement waves within the waveguide in a form

$$u_{tt} - c^2 u_{xx} = \frac{\beta}{\rho} u_x u_{xx} + \frac{J\nu^2}{\sigma}(u_{tt} - c_1^2 u_{xx})_{xx}. \tag{2.13}$$

We differentiate (2.13) with respect to x, introducing $u_x = f$, to find the Boussinesq equation

$$f_{tt} - c^2 f_{xx} = \frac{\beta}{2\rho}(f^2)_{xx} + \frac{J\nu^2}{\sigma}(f_{tt} - c_1^2 f_{xx})_{xx}, \tag{2.14}$$

which describes the longitudinal strain in an elastic waveguide of rectangular cross section. Here the linear longitudinal wave velocity is $c = \sqrt{E/\rho}$, the linear shear wave velocity (shear stress written in terms of velocity) is $c_1 = \sqrt{\mu/\rho} = c/\sqrt{2(1+\nu)}$, and the polar moment of inertia of the rectangular cross section σ, is given by

$$J = \int_\sigma (y^2 + z^2)\mathrm{d}\sigma = \frac{4ab(a^2 + b^2)}{3}. \tag{2.15}$$

Considering the change of variables

$$\tilde{t} = \frac{t}{T}, \quad \tilde{x} = \frac{x}{X}, \quad \tilde{u} = \frac{u}{U}, \tag{2.16}$$

and substituting the respective partial derivatives into (2.13) gives

$$\tilde{u}_{\tilde{t}\tilde{t}} - c^2 \frac{T^2}{X^2}\tilde{u}_{\tilde{x}\tilde{x}} = \frac{\beta}{\rho}\frac{UT^2}{X^3}\tilde{u}_{\tilde{x}}\tilde{u}_{\tilde{x}\tilde{x}} + \frac{J\nu^2}{\rho}\frac{1}{X^2}\tilde{u}_{\tilde{x}\tilde{x}\tilde{t}\tilde{t}}. \tag{2.17}$$

We compare this to the regularised Boussinesq equation

$$u_{tt} - c^2 u_{xx} = \varepsilon(-12 u_x u_{xx} + 2u_{ttxx}), \tag{2.18}$$

to give

$$cT = X, \quad U = \frac{-12\varepsilon EX}{\beta}, \quad X = \sqrt{\frac{J\nu^2}{2\varepsilon\sigma}\left(1 - \frac{c_1^2}{c^2}\right)}. \tag{2.19}$$

The parameters $\alpha, c, \frac{E}{\beta}$ and c_1 describe the physical and geometrical properties of the waveguide, and $\varepsilon \ll 1$ is the small wave amplitude parameter. Equation (2.18) is in a regularised manner to facilitate straightforward application of numerical schemes.

2.1.2 Weakly-nonlinear solution

Let us consider a generalised version of (2.18), given by

$$u_{tt} - c^2 u_{xx} = \varepsilon(\alpha u_x u_{xx} + \beta u_{ttxx}). \tag{2.20}$$

Differentiating (2.20) with respect to space and denoting $u_x = f$ yields the longitudinal strain of the elastic waveguide as

$$f_{tt} - c^2 f_{xx} = \varepsilon\left(\frac{\alpha}{2}(f^2)_{xx} + \beta f_{ttxx}\right). \tag{2.21}$$

To attain accurate results with minimal algebraic rearrangement, we consider the following weakly-nonlinear solution of (2.21) as

$$f(x,t) = f^-(\xi,T) + f^+(\eta,T) + \varepsilon P(\xi,\eta,T) + \mathcal{O}(\varepsilon^2), \tag{2.22}$$

where the functions $f^-(\xi,T)$ and $f^+(\eta,T)$ represent a leading order solution that describes wave propagation in the left and right directions, respectively. The fast characteristic variables are given by $\xi = x - ct$ and $\eta = x + ct$ and the slow time variable is given by $T = \varepsilon t$. The term $P(\xi,\eta,T)$ is the higher-order correction describing the propagation in both the left and right directions. The principle of incorporating characteristic variables to describe the interactions of solitons was introduced by Miles in 1977 [86]. As ξ contains $-ct$ the wave in the characteristic reference frame moves at a speed c to the right, conversely as η contains $+ct$ the wave in the characteristic frame moves at a speed c to the left.

The configuration of the system given by (2.21), which incorporates a mixed fourth-order derivative in place of a fourth-order spatial derivative, proves advantageous for numerical simulations due to the mitigation of short wave instability as highlighted in [87,88]. Differentiating $f(x,t)$ to find f_{tt}, f_{xx}, $(f^2)_{xx}$ and f_{ttxx} and substituting these terms into equation (2.21) will ultimately yield an equation describing the terms in the expansion. The partial derivative of $f(x,t)$ with respect to t can be expressed by

$$f_t = \frac{\partial f}{\partial t} = \frac{\partial}{\partial t}(f^- + f^+ + \varepsilon P). \tag{2.23}$$

The partial derivative $\frac{\partial}{\partial t}$ can expressed as a differential operator in conjunction with the three characteristic variables. Using the chain rule, we can write this as

$$f_t = (\frac{\partial \xi}{\partial t} \times \frac{\partial}{\partial \xi} + \frac{\partial \eta}{\partial t} \times \frac{\partial}{\partial \eta} + \frac{\partial T}{\partial t} \times \frac{\partial}{\partial T})(f^- + f^+ + \varepsilon P) \tag{2.24}$$

$$= (-c\frac{\partial}{\partial \xi} + c\frac{\partial}{\partial \eta} + \varepsilon\frac{\partial}{\partial T})(f^- + f^+ + \varepsilon P). \tag{2.25}$$

Applying partial differentiation to each respective term yields

$$f_t = -cf_\xi^- + cf_\eta^+ + \varepsilon(-cP_\xi + cP_\eta + f_T^- + f_T^+) + \mathcal{O}(\varepsilon^2). \tag{2.26}$$

By using a similar approach, we can derive the remaining partial derivatives for (2.21). Substituting these derivatives into (2.21) yields

$$\begin{aligned}
&\left(c^2 f_{\xi\xi}^- + c^2 f_{\eta\eta}^+ + \varepsilon\left(-2cf_{T\xi}^- + 2cf_{T\eta}^+ - 2c^2 P_{\eta\xi} + c^2 P_{\eta\eta} + c^2 P_{\xi\xi}\right)\right) \\
&\quad - c^2\left(f_{\xi\xi}^- + f_{\eta\eta}^+ + \varepsilon\left(P_{\eta\eta} + P_{\xi\xi} + 2P_{\eta\xi}\right)\right) \\
=&\varepsilon\left(\frac{\alpha}{2}\left(2\left(f^- f_\xi^-\right)_\xi + 2\left(f^+ f_\eta^+\right)_\eta + 2f_{\xi\xi}^- f^+ + 2f^- f_{\eta\eta}^+ + 4f_\xi^- f_\eta^+\right) + \beta\left(c^2 f_{\xi\xi\xi\xi}^- + c^2 f_{\eta\eta\eta\eta}^+\right)\right) + \mathcal{O}(\varepsilon^2),
\end{aligned} \tag{2.27}$$

which can be simplified to

$$\begin{aligned}
-4c^2 P_{\xi\eta} = 2cf_{T\xi}^- + \alpha(f^- f_\xi^-)_\xi + \beta c^2 f_{\xi\xi\xi\xi}^- - 2cf_{T\eta}^+ + \alpha(f^+ f_\eta^+)_\eta \\
+ \ \beta c^2 f_{\eta\eta\eta\eta}^+ + \alpha f_{\xi\xi}^- f^+ + \alpha f^- f_{\eta\eta}^+ + 2\alpha f_\xi^- f_\eta^+.
\end{aligned} \tag{2.28}$$

We now perform time averaging at constant η to (2.28). This involves fixing η while integrating (2.28) over time, t, defined as follows:

$$\lim_{\tau\to\infty} \frac{1}{\tau}\int_0^\tau P_{\xi\eta}\ \mathrm{d}t. \tag{2.29}$$

where τ is a dummy variable. To facilitate the evaluation, we rewrite the time integral by transforming the variables while ensuring that η remains constant throughout the process to give

$$\lim_{\tau\to\infty} \frac{1}{\tau}\int_0^\tau P_{\xi\eta}\ \mathrm{d}t = \lim_{\tau\to\infty} \frac{1}{\tau}\int_\xi^{2c\tau+\xi} P_{\xi\eta}\ \frac{\mathrm{d}\eta}{2c}. \tag{2.30}$$

Next we assume that the incident, reflected, and transmitted functions, along with their derivatives, are bounded and sufficiently rapidly decaying at infinity for any fixed T (in line with numerical experiments

[89, 90]), under these conditions, the integral simplifies to

$$\lim_{\tau\to\infty}\frac{1}{\tau}\int_0^{\tau} P_{\xi\eta}\,\mathrm{d}t = \frac{1}{2c}\lim_{\tau\to\infty}\frac{1}{\tau}[P_\xi]_{\xi}^{2c\tau+\xi} = 0, \tag{2.31}$$

as all P terms are required to be bounded. The same principle of time averaging applied to the right-hand side of (2.28) yields

$$\begin{aligned} 0 = &\left(2cf_T^- + \alpha(f^-f_\xi^-) + \beta c^2 f_{\xi\xi\xi}^-\right)_\xi \lim_{\tau\to\infty}\left[\frac{\eta}{2c\tau}\right]_\xi^{2c\tau+\xi} \\ &+ \lim_{\tau\to\infty}\frac{1}{2c\tau}\left[-2cf_T^+ + \alpha(f^+f_\eta^+) + \beta c^2(f_{\eta\eta\eta}^+)\right]_\xi^{2c\tau+\xi} \\ &+ \lim_{\tau\to\infty}\frac{1}{2c\tau}\int_\xi^{2c\tau+\xi}\left(2\alpha f_{\xi\xi}^- f^+ + 2\alpha f^- f_{\eta\eta}^+ + 4\alpha f_\xi^- f_\eta^+\right)d\eta, \end{aligned} \tag{2.32}$$

where f^- and f^+ are bounded and sufficiently rapidly decaying at infinity. Under these assumptions, the terms in the second and third lines of (2.32) become zero upon averaging. Thus, only the first line of (2.32) remains non-zero, and the resulting expression simplifies to

$$\left(2cf_T^- + \alpha(f^-f_\xi^-) + \beta c^2 f_{\xi\xi\xi}^-\right)_\xi = 0, \tag{2.33}$$

which via integration with respect to ξ yields the right-propagating leading order solution

$$2cf_T^- + \alpha(f^-f_\xi^-) + \beta c^2 f_{\xi\xi\xi}^- = 0, \tag{2.34}$$

which corresponds to the Korteweg-de Vries (KdV) equation. Applying a similar process with respect to ξ, we also garner the left-propagating leading order equation

$$-2cf_T^+ + \alpha f^+ f_\eta^+ + \beta c^2 f_{\eta\eta\eta}^+ = 0. \tag{2.35}$$

Now substituting (2.34) and (2.35) into (2.28) gives

$$-4c^2 P_{\xi\eta} = \alpha f_{\xi\xi}^- f^+ + \alpha f^- f_{\eta\eta}^+ + 2\alpha f_\xi^- f_\eta^+. \tag{2.36}$$

Integrating equation (2.36) with respect to η and ξ gives the higher-order correction function

$$P = \phi^-(\xi,T) + \phi^+(\eta,T) - \frac{\alpha}{4c^2}\left(f^-\int_{-L}^{\eta} f^+\,\mathrm{d}\eta + f^+\int_{-L}^{\xi} f^-\,\mathrm{d}\xi + 2f^-f^+\right), \tag{2.37}$$

where $\phi^-(\xi, T)$ and $\phi^+(\eta, T)$ are integration constants. Now we consider the initial conditions

$$f(x,0) = \hat{f}(x) \quad f_t(x,0) = g(x). \tag{2.38}$$

Multiplying the derivative of $\hat{f}(x)$ by c with respect to x and adding this to $g(x)$ gives

$$cf'(x) + g(x) = 2cf^+_\eta|_{t=0} \implies f^+|_{t=0} = \frac{1}{2c}\left[cf(x) + \int_{-L}^{x} g(s)\ \mathrm{d}s\right], \tag{2.39}$$

and conversely subtracting the equations gives

$$cf'(x) - g(x) = 2cf^-_\xi|_{t=0} \implies f^-|_{t=0} = \frac{1}{2c}\left[cf(x) - \int_{-L}^{x} g(s)\ \mathrm{d}s\right], \tag{2.40}$$

where $f^+|_{t=0}$ and $f^-|_{t=0}$ are the initial positions of the left and right propagating waves respectively [91].

2.2 Scattering problem - two-layered elastic waveguide with delamination

Building upon the work established in Section 2.1, we now shift our focus to the structure in Figure 2.2 which is a two-layered waveguide with delamination on the right. The presence of delamination is a type

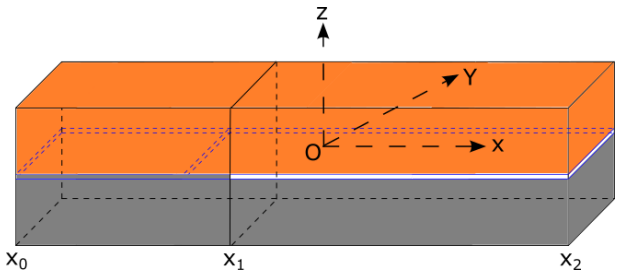

Figure 2.2: Two-layered symmetric waveguide with delamination at x_1 to x_2

of damage in multi-layer structures and is commonly encountered in civil and mechanical engineering applications as outlined in Section 1.2. In areas where delamination is present solitons undergo fission, providing a valuable indicator of delamination. In this section, we will use nonlinear elasticity theory to derive a system of DDEs for the longitudinal displacement of the nonlinear waves within the waveguide and then find a weakly-nonlinear solution.

2.2.1 Nonlinear elasticity theory

Consider a two-layered waveguide with perfect bonding on the left, x_0 to x_1, and delamination on the right, x_1 to x_2 as shown in Figure 2.2 and [45,47], where $x_1 = 0$. Due to the delamination, the generated long longitudinal strain waves scatter within the delaminated region. We make the assumption that the cross section x_1 is a perfect interface, meaning that at the boundary of the two regions, the interface is smooth and free of geometric irregularities. Similarly to the single elastic waveguide in Section 2.1, we consider the problem for the scheme of nonlinear dynamic elasticity and assume the delamination area is $\{x_1 \leq x \leq x_2, -a < y < a, z = 0\}$ and the perfect bonded region has identical layers with a width of $2a$ and height b.

Let us consider (2.13), where the wave displacement in the bonded region (x_0 to x_1) is $u^-(x,t)$, and in the delaminated region (x_1 to x_2) is $u^+(x,t)$. We use $u^\pm(x,t)$ to denote the displacement in both regions, leading to the two DDEs in the form

$$u^\pm_{tt} - c^2_\pm u^\pm_{xx} = \delta_\pm (u^\pm_{tt} - c^2_{1\pm} u^\pm_{xx})_{xx} + \frac{\beta_\pm c^2_\pm}{E_\pm} u^\pm_x u^\pm_{xx}, \tag{2.41}$$

and write the continuity condition for normal stress as

$$c^2_- u^-_x + \left(\delta_- (u^-_{tt} - c^2_{1-} u^-_{xx})_x + \frac{1}{2} \frac{\beta_- c^2_-}{E_-} u^{-2}_x \right) \Big|_{x=0} = c^2_+ u^+_x + \left(\delta_+ (u^+_{tt} - c^2_{1+} u^+_{xx})_x + \frac{1}{2} \frac{\beta_+ c^2_+}{E_+} u^{+2}_x \right) \Big|_{x=0}, \tag{2.42}$$

which is generated by the waveguides applying pressure against each other. The $\delta_\pm$ term is a dispersion coefficient, typically used within the context of oceanic waves to factor in the Earth's curvature [92]. The difference in bonding between the regions (x_0, x_1) and (x_1, x_2) results in varying normal stresses. Consequently, we denote the normal stress as

$$f^\pm_{tt} = \frac{\partial \sigma^\pm}{\partial x}. \tag{2.43}$$

When the soliton reaches the $x = 0$ boundary, the stress between the two waveguides is denoted by the continuity of longitudinal stress

$$\sigma^-|_{x=0} = \sigma^+|_{x=0}. \tag{2.44}$$

We define the dimensionless variables as

$$\tilde{t} = \frac{t}{T^*}, \quad \tilde{x} = \frac{x}{X^*}, \quad \tilde{u}^\pm = \frac{u^\pm}{U^*}, \tag{2.45}$$

where

$$T^* = \frac{X^*}{c_-}, \quad U^* = -\varepsilon \frac{12E_-}{\beta_-} X^*, \quad X^* = \sqrt{\varepsilon^{-1} \frac{\delta_-}{2} \left(1 - \frac{c_{1-}^2}{c_-^2}\right)}, \tag{2.46}$$

in order to reduce the number of parameters in the problem. To develop the weakly-nonlinear theory, we define the small parameter

$$\varepsilon = \frac{\delta_-}{2X^{*2}} \left(1 - \frac{c_{1-}^2}{c_-^2}\right) = \frac{\delta_-}{(X^*)^2} \frac{1 + 2\nu_-}{4(1 + \nu_-)}, \tag{2.47}$$

which is consistent when the considered waves are assumed to be long ($\delta_-/(X^*)^2 \ll 1$). The nonlinearity balances the linear dispersion which is consistent with the assumption of small deformation ($U^*/X^* \ll 1$) [32]. The governing wave problem thus takes the following form up to $\mathcal{O}(\varepsilon)$:

$$u_{tt}^- - u_{xx}^- = 2\varepsilon(-6u_x^- u_{xx}^- + u_{xxxx}^-), \ x < 0, \tag{2.48}$$

$$u_{tt}^+ - c^2 u_{xx}^+ = 2\varepsilon(-6\beta u_x^+ u_{xx}^+ + \gamma u_{xxxx}^+), \ x > 0, \tag{2.49}$$

with the continuity of longitudinal displacement as

$$u^-|_{x=0} = u^+|_{x=0}, \tag{2.50}$$

and the initial conditions $u^\pm(x, 0) = F^\pm(x)$. The associated strain continuity conditions are given by

$$u_x^- + 2\varepsilon[-3(u_x^-)^2 + u_{xxx}^-]|_{x=0} = c^2 u_x^+ + 2\varepsilon[-3\beta(u_x^+)^2 + \gamma u_{xxx}^+]|_{x=0}. \tag{2.51}$$

In the equations above, we use the asymptotic relations $u_{ttxx}^- = u_{xxxx}^- + \mathcal{O}(\varepsilon)$ and $u_{ttxx}^+ = c^2 u_{xxxx}^+ + \mathcal{O}(\varepsilon)$, along with introducing the following dimensionless parameters:

$$c^2 = \frac{c_+^2}{c_-^2}, \quad \beta = \frac{\beta_+ c_+^2/E_+}{\beta_- c_-^2/E_-}, \quad \gamma = \frac{\delta_+(c_+^2 - c_{1+}^2)}{\delta_-(c_-^2 - c_{1-}^2)}, \tag{2.52}$$

(note the c and β here are different to the ones in the previous section). We assume the dimensionless parameters to be of $\mathcal{O}(1)$. Equations (2.48) – (2.51) follow the notation in [45], whereas [47], which does not use asymptotic expansions, presents a slightly different form. However, the methodology applied in Section 2.2.2 will remain unchanged, differing only in parameter representation.

2.2.2 Model formulation

The weakly-nonlinear solutions are expressed as

$$u^-(x,t) = I(\xi_-, X) + R(\eta_-, X) + \varepsilon P(\xi_-, \eta_-, X) + \mathcal{O}(\varepsilon^2), \tag{2.53}$$

$$u^+(x,t) = T(\xi_+, X) + \varepsilon Q(\xi_+, \eta_+, X) + \mathcal{O}(\varepsilon^2), \tag{2.54}$$

where I and R represent the incident and reflected waves, respectively, within the left region of the waveguide, and T represents the transmitted wave within the right region of the waveguide which is generated at the $x = 0$ boundary by the incident wave. The incident and reflective wave behave in a similar manner as in Section 2.1. P is the higher-order correction of the wave at $x < 0$ and Q is the higher-order correction to the wave at $x > 0$. The characteristic variables are described by $\xi_- = x - t$, $\xi_+ = x - ct$, $\eta_- = x + t$, $\eta_+ = x + ct$ and $X = \varepsilon x$. Substituting the respective weakly-nonlinear solutions into (2.48) gives

$$-2P_{\xi_-\eta_-} = (I_X - 3(I^2)_{\xi_-} + I_{\xi_-\xi_-\xi_-})_{\xi_-} + (R_X - 3(R^2)_{\eta_-} + R_{\eta_-\eta_-\eta_-})_{\eta_-} - 6(IR_{\eta_-} + RI_{\xi_-})_{\xi_-\eta_-}. \tag{2.55}$$

We now apply space averaging to (2.55) with respect to η_-, similarly to the time averaging detailed in Section 2.1. While time averaging involved averaging over the time domain axis t to find higher-order terms, space averaging is performed over the spatial domain $x \in (-\infty, 0]$. To average the $P_{\xi_-\eta_-}$ term on the left-hand side of (2.55) with respect to a dummy variable τ, as was done in time averaging, we integrate over x while holding η_- constant, this gives

$$\lim_{\tau\to-\infty} \frac{1}{\tau - 0} \int_0^\tau P_{\xi_-\eta_-}\, \mathrm{d}x. \tag{2.56}$$

Next, by transforming to characteristic variables, where the integration is performed along η_-, the expression becomes

$$\lim_{\tau\to-\infty} \frac{1}{\tau - 0} \int_0^\tau P_{\xi_-\eta_-}\, \mathrm{d}x = \lim_{\tau\to-\infty} \frac{1}{\tau} \int_{-\xi_-}^{2\tau-\xi_-} P_{\xi_-\eta_-} \frac{\mathrm{d}\eta_-}{2}. \tag{2.57}$$

Using the boundedness and rapid decay of the higher-order corrections and their derivatives as $\tau \to -\infty$, we obtain

$$\lim_{\tau\to-\infty} \frac{1}{2\tau} [P_{\xi_-}]_{-\xi_-}^{2\tau-\xi_-} = 0. \tag{2.58}$$

Now averaging the right-hand side of (2.55) gives

$$\begin{aligned} 0 = &\left(I_X - 3(I^2)_{\xi_-} + I_{\xi_-\xi_-\xi_-}\right)_{\xi_-} \lim_{\tau\to-\infty}\left[\frac{\eta_-}{2\tau}\right]_{-\xi_-}^{2\tau-\xi_-} \\ &+ \lim_{\tau\to-\infty}\frac{1}{2\tau}\left[R_X - 3(R^2)_{\eta_-} + R_{\eta_-\eta_-\eta_-}\right]_{-\xi_-}^{2\tau-\xi_-} \\ &- \lim_{\tau\to-\infty}\frac{1}{2\tau}\int_{-\xi_-}^{2\tau-\xi_-} 6(IR_{\eta_-} + RI_{\xi_-})_{\xi_-\eta_-}d\eta_-. \end{aligned} \tag{2.59}$$

As I and R are bounded this summation is reduced to the leading order equation

$$\tilde{I}_X - 6\tilde{I}\tilde{I}_{\xi_-} + \tilde{I}_{\xi_-\xi_-\xi_-} = 0, \tag{2.60}$$

where $\tilde{I} = I_{\xi_-}$. Now similarly applying space averaging with respect to ξ_- gives the following leading order equation

$$\tilde{R}_X - 6\tilde{R}\tilde{R}_{\eta_-} + \tilde{R}_{\eta_-\eta_-\eta_-} = 0, \tag{2.61}$$

where $\tilde{R} = R_{\eta_-}$. Substituting our leading order solutions into (2.55) and applying integration with respect to ξ_- and η_- gives the higher-order corrections

$$P(\xi_-.\eta_-, X) = \phi(\xi_-, X) + \psi(\eta_-, X) - 6\left(\int I_{\xi_-}R\mathrm{d}\eta_- + \int IR_{\eta_-}\mathrm{d}\xi_- + 2IR\right), \tag{2.62}$$

where $\phi(\xi_-, X)$ and $\psi(\eta_-, X)$ are arbitrary integration constants. Now applying a similar process for (2.49), we obtain the following leading order equation

$$\tilde{T}_X - \frac{6\alpha}{c^2}\tilde{T}\tilde{T}_{\xi_+} + \frac{\beta}{c^2}\tilde{T}_{\xi_+\xi_+\xi_+} = 0, \tag{2.63}$$

where $\tilde{T} = T_{\xi_-}$ and the corresponding higher-order correction is

$$Q(\xi_+, \eta_+, X) = q(\xi_+, X) + r(\eta_+, X), \tag{2.64}$$

where $q(\xi_+, X)$ and $r(\eta_+, X)$ are arbitrary integration constants. Differentiating (2.50) with respect to t gives

$$u_t^-|_{x=0} = u_t^+|_{x=0}. \tag{2.65}$$

Substituting our weakly-nonlinear solutions at leading order into (2.65) yields

$$I_{\xi_-}|_{x=0} - R_{\eta_-}|_{x=0} = cT_{\xi_+}|_{x=0}. \tag{2.66}$$

Similarly, substituting our weakly-nonlinear solution into (2.51) and applying some mathematical rearrangement gives

$$I_{\xi_-}|_{x=0} + R_{\eta_-}|_{x=0} = c^2 T_{\xi_+}|_{x=0}. \tag{2.67}$$

Now applying simultaneous equations techniques to solve (2.66) and (2.67) gives

$$T_{\xi_+}|_{x=0} = C_T I_{\xi_-}|_{x=0} \quad \text{and} \quad R_{\eta_-}|_{x=0} = C_R I_{\xi_-}|_{x=0}, \tag{2.68}$$

where $C_R = \frac{c-1}{c+1}$ and $C_T = \frac{2}{c(1+c)}$ are the reflection and transmission coefficients respectively. When $c = 1$, i.e. the materials are the same in the bonded and delaminated regions, we see $C_T = 1$ and $C_R = 0$ and thus the leading order reflective wave is zero.

2.3 Initial-value problem - coupled Boussinesq equations

In the following section, we will investigate a cKG model [28]. Then we will explore the FPU chains, specifically by incorporating two weakly coupled FPU chains to derive coupled Boussinesq equations, which has been examined in detail in the work of [29]. Next we will consider the symmetric case for our coupled Boussinesq equation to obtain and analyse the linearised dispersion relation. Finally we will be observing the work done in [48] where they investigated the propagation of radiating solitary waves within a two-layered structure containing soft bonding, which was described by coupled Boussinesq equations. We will examine two scenarios in which the weakly-nonlinear solution assumes distinct forms based on the value of the parameter c. The bonding between the waveguides in [48] varied, but we will only be considering a soft bonded region [72].

2.3.1 Coupled Klein–Gordon chains

In [78] a model of cKG chains is studied as shown in Figure 2.3. We consider two interconnected linear periodic chains of particles where each particle in the upper and lower chain possesses a mass denoted as m_1 and m_2, respectively, as illustrated in Figure 2.3. Similar to the FPU model, the inter-particle separation within each chain at of a distance a, where the particles are moving solely along the x-axis. The interaction between neighbouring particles within each chain adheres to the harmonic model

$$\begin{aligned} m_1 \ddot{u}_n &= \beta_1 \left(u_{n+1} - 2u_n + u_{n-1}\right) - \frac{\partial H\left(u_n, w_n\right)}{\partial u_n}, \\ m_2 \ddot{w}_n &= \beta_2 \left(w_{n+1} - 2w_n + w_{n-1}\right) - \frac{\partial H\left(u_n, w_n\right)}{\partial w_n}, \end{aligned} \tag{2.69}$$

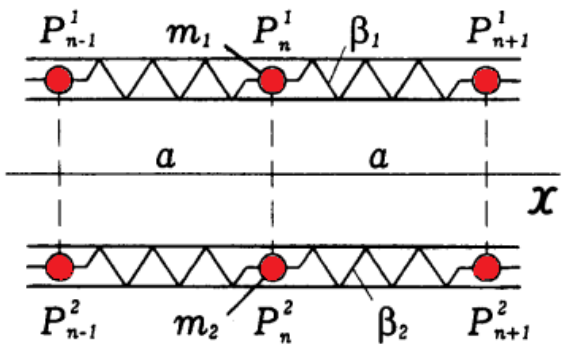

Figure 2.3: Illustration of the cKG chain model.

with distinct interaction constants β_1 and β_2 and the dot representing differentiation with respect to time and $H(u_n, w_n)$ denoting the energy associated with the interaction between P^1_n and P^2_n. The displacements of particles P^1_n and P^2_n, denoted as u_n and w_n respectively, determine the interaction between the two chains. We define dimensionless variables as

$$\begin{gathered}\tilde{t} = \frac{c_1}{a}t, \quad \tilde{x} = \frac{x}{a}, \quad \tilde{u} = \frac{u}{a}, \quad \tilde{w} = \sqrt{\frac{m_2}{m_1}}\frac{w}{a}, \quad \tilde{H} = \frac{H}{m_1 c_1^2}, \\ c^2\frac{c_2^2}{c_1^2} = \frac{\beta_2 m_1}{\beta_1 m_2}, \quad c_i^2 = \frac{\beta_i a^2}{m_i}, \quad i = 1, 2.\end{gathered} \tag{2.70}$$

By introducing a force function as $f(\tilde{u}, \tilde{w}) = -\tilde{H}(\tilde{u}, \tilde{w})$ and applying the long-wave approximation to (2.69), we obtain the following system of PDEs

$$u_{tt} - u_{xx} = f_u(u, w), \quad w_{tt} - c^2 w_{xx} = f_w(u, w), \tag{2.71}$$

where the tildes are omitted for simplicity [28]. More recent work instead implemented coupled Boussinesq equations for coupled problems [48], which will be discussed in Section 2.3.2.

2.3.2 Fermi-Pasta-Ulam model

In this section we will consider the original FPU chain model outlined in [9] and shown in Figure 2.4. Both sides of the chain are assumed to be clamped at equilibrium, and the equilibrium distance between particles is a. We assume $u_0 = u_N = 0$ when a chain contains $N+1$ particles. Firstly we want to describe the displacements of these particles from their state of rest using the equations of motion. We denote the kinetic and potential energies of the individual particles as

$$E_k = \frac{1}{2}mv^2, \quad E_P = \frac{1}{2}kx^2, \tag{2.72}$$

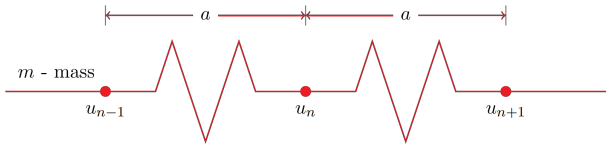

Figure 2.4: FPU chain model consisting of a chain of equidistant particles connected to their nearest neighbours by weakly-nonlinear springs, where u_n represents the displacement of the n^{th} particle from the equilibrium.

where k denotes the linear spring constant, v is the velocity of the particle, m is the mass of the particle and x is the particle's displacement. Then, we calculate the kinetic energy, T, and potential energy, U within the system where we sum up the kinetic (or potential) energy from each individual chain to obtain the total (or potential) system's kinetic energy. These total energy is expressed as

$$T = \sum_n \frac{m\dot{u}_n^2}{2}. \tag{2.73}$$

Now, the total potential energy, represented by U, can be denoted in a similar manner. However, we must consider the weakly-nonlinear nature of the springs, thus we incorporate a nonlinear spring constant term, denoted by α. Namely, we have

$$U = \sum_n \left(\frac{k}{2}(u_{n+1} - u_n)^2 + \frac{\alpha}{3}(u_{n+1} - u_n)^3 \right). \tag{2.74}$$

As the Lagrangian of the system is denoted as

$$L = T - U = \sum_n \frac{m\dot{u}_n^2}{2} - \sum_n \left(\frac{k}{2}(u_{n+1} - u_n)^2 + \frac{\alpha}{3}(u_{n+1} - u_n)^3 \right), \tag{2.75}$$

we can substitute T and U into the equations of motion, given by the Euler-lagrange equations

$$\frac{\mathrm{d}}{\mathrm{d}t}\left(\frac{\partial L}{\partial \dot{u}_n}\right) - \frac{\partial L}{\partial u_n} = 0. \tag{2.76}$$

In doing so, we obtain the system

$$m\ddot{u}_n = (u_{n+1} - 2u_n + u_{n-1})[k + \alpha(u_{n+1} - u_{n-1})]. \tag{2.77}$$

The motion of the particles in the chain is described by the discrete system (2.77), which will later be extended to a continuous model for the displacement [11]. We introduce the continuum approximation as

$$u_n(t) = u(x_n, t) = u(na, t), \quad u_{n\pm1} = u(x_n \pm a, t), \tag{2.78}$$

where the displacement field u slowly varies. Substituting the Taylor expansions

$$u_{n\pm1}(t) = u(x_n, t) \pm au'(x_n, t) + \frac{a^2}{2}u''(x_n, t) + \frac{a^3}{6}u'''(x_n, t) + \frac{a^4}{24}u''''(x_n, t) + ..., \tag{2.79}$$

into (2.77) allows us to transform the following discrete model to this continuous differential equation

$$mu_{tt} = ka^2u_{xx} + 2\alpha a^3u_xu_{xx} + \frac{ka^4}{12}u_{xxxx}, \tag{2.80}$$

which excludes higher-order terms by truncating the Taylor series. This equation is of the form of a Boussinesq equation which describes the long wave propagation in the chain model (2.77). Equation (2.80) can be rescaled as

$$u_{tt} - c^2u_{xx} = \varepsilon c^2(u_xu_{xx} + \delta^2u_{xxxx}), \tag{2.81}$$

where

$$c^2 = \frac{ka^2}{m}, \quad \varepsilon = \frac{2\alpha a}{k}, \quad \delta^2 = \frac{a^2}{12\varepsilon}. \tag{2.82}$$

Equation (2.81) can then be regularised using the asymptotic relation $u_{ttxx} = c^2u_{xxxx}$, giving

$$u_{tt} - c^2u_{xx} = \varepsilon c^2\left(u_xu_{xx} + \frac{\delta^2}{c^2}u_{ttxx}\right). \tag{2.83}$$

2.3.3 Coupled Fermi-Pasta-Ulam model

Now let us consider the coupled FPU chain model as shown in Figure 2.5 [9]. The individual particles and the kinetic energy are denoted similarly as in Section 2.3.3, but the potential energy expression is derived with the inclusion of a coupling term. The kinetic and potential energy are denoted as

$$\begin{aligned} T &= \sum_n \frac{1}{2}\left(m\dot{u}_n^2 + M\dot{w}_n^2\right), \\ U &= \sum_n \left(\frac{1}{2}\alpha(u_{n+1} - u_n)^2 + \frac{1}{3}\beta(u_{n+1} - u_n)^3 + \frac{1}{2}A(w_{n+1} - w_n)^2\right. \\ &\qquad \left. + \frac{1}{3}B(w_{n+1} - w_n)^3 + \frac{1}{2}\gamma(u_n - w_n)^2\right), \end{aligned} \tag{2.84}$$

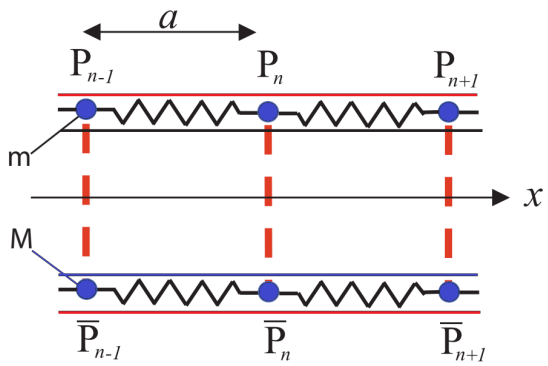

Figure 2.5: Coupled FPU chain model consisting of a chain of equidistant particles connected to their nearest neighbours by weakly-nonlinear springs, where u_n and w_n represent the displacement of the n^{th} particle from the equilibrium in the upper and lower layers respectively

respectively, where α and A are the nonlinear spring constant, β and B denote the nonlinearity coefficients for the chain and γ represents the coupling coefficient. Now we apply a similar process as outlined in Section 2.3.2 with the Lagrangian denoted as $L = T - U$, which is substituted into the Euler-Lagrange relations

$$\frac{\mathrm{d}}{\mathrm{d}t}\left(\frac{\partial L}{\partial \dot{u}_n}\right) - \frac{\partial L}{\partial u_n} = 0, \quad \frac{\mathrm{d}}{\mathrm{d}t}\left(\frac{\partial L}{\partial \dot{w}_n}\right) - \frac{\partial L}{\partial w_n} = 0 \tag{2.85}$$

to yield the following system

$$\begin{aligned} m\ddot{u}_n &= (u_{n+1} - 2u_n + u_{n-1})[\alpha + \beta(u_{n+1} - u_{n-1})] - \delta(u_n - w_n), \\ M\ddot{w}_n &= (w_{n+1} - 2w_n + w_{n-1})[A + B(w_{n+1} - w_{n-1})] + \delta(u_n - w_n). \end{aligned} \tag{2.86}$$

Using a Taylor expansion about the equilibrium point, for the derived difference-differential equations in each chain, as Section 2.3.2 garners the following cRB equations

$$\begin{aligned} u_{tt} - u_{xx} &= u_x u_{xx} + u_{ttxx} - \delta(u - w), \\ w_{tt} - c^2 w_{xx} &= \alpha w_x w_{xx} + \beta w_{ttxx} + \gamma(u - w). \end{aligned} \tag{2.87}$$

Here δ and γ denote the dispersion coefficients in the upper and lower layer, respectively, which factors in the soft bonding component between layered waveguides.

2.3.4 Symmetric case and dispersion relation

Differentiating the system (2.87) with respect to x and denoting $u_x = f$ and $w_x = g$, we obtain

$$\begin{aligned} f_{tt} - f_{xx} &= \frac{1}{2}(f^2)_{xx} + f_{ttxx} - \delta(f-g), \\ g_{tt} - c^2 g_{xx} &= \frac{1}{2}\alpha(g^2)_{xx} + \beta g_{ttxx} + \gamma(f-g). \end{aligned} \tag{2.88}$$

In the symmetric case, where $c = \alpha = \beta = 1$ and $g = f$, the system (2.88) reduces to

$$f_{tt} - f_{xx} = \frac{1}{2}(f^2)_{xx} + f_{ttxx}, \tag{2.89}$$

which has a particular solution in the form of the solitary wave

$$f(x,t) = A\text{sech}^{\,2}\left(\frac{x-ct}{\Lambda}\right), \tag{2.90}$$

where

$$A = -\frac{c^2-1}{4\varepsilon} \quad \text{and} \quad \Lambda = -\frac{c}{6\varepsilon\sqrt{c^2-1}}. \tag{2.91}$$

For (2.88), the linear waves propagating within this model are described by the dispersion relations $f \approx Ae^{ik(x-pt)}$ and $g \approx Be^{ik(x-pt)}$, where k represents the wavenumber and p represents the phase speed, the speed at which a wave propagates. It will be assumed that the coefficients in (2.88) are perturbed and compared to the symmetric case, but remain positive, thus resulting in the following linearised dispersion relations:

$$\left[k^2(1-p^2) - k^4p^2 + \delta\right]\left[k^2(c^2-p^2) - \beta k^4p^2 + \gamma\right] = \gamma\delta. \tag{2.92}$$

When the symmetry is broken, these pure solitary wave solutions are replaced with radiating solitary waves and are structurally unstable and their tail rapidly decays to zero. This occurs due to a possible resonance of the linear wave spectrum at some finite non-zero k. This resonance enables the solitary wave to emit energy, resulting in the formation of radiating solitary waves. These solutions are observed when the wave speeds are close between two waveguides [29]. Directly solving the biquadratic equation (2.92) is not very helpful, as the resulting formula is difficult to analyse. Fortunately, the analysis of (2.92) becomes considerably simplified through a change of variables [29]

$$S = k^2(1-p^2) - k^4p^2 + \delta, \quad \text{or} \quad p^2 = \frac{\delta + k^2 - S}{k^2(1+k^2)}. \tag{2.93}$$

Thus we may rewrite (2.92) as

$$S^2 - bS - c = 0, \tag{2.94}$$

where

$$b = \delta + k^2 - \kappa(\gamma + k^2 c^2), \quad c = \kappa\gamma\delta, \quad \kappa = \frac{1+k^2}{1+\beta k^2}. \tag{2.95}$$

Furthermore, we establish the following relation between the amplitudes A and B

$$B = \frac{S}{\delta}A = \frac{\kappa\gamma}{S-b}A, \tag{2.96}$$

which gives us

$$S_{1,2} = \frac{1}{2}(b \pm \sqrt{b^2 + 4ac}), \tag{2.97}$$

where S_1 corresponds to the positive square root and S_2 the negative square root. As c is positive, we find $S_1 > 0$ and $S_2 < 0$. We observe that $0 < S_1 \leq \delta + k^2$, supporting the existence of real values of p for any k. For fixed k, the inequality $S_2 < S_1$ holds, and hence using (2.93) we find that $P_2 > P_1$.

2.3.5 Two-layered elastic waveguide with soft bonding

Now let us consider two scattering problems for a two-layered waveguide containing soft bonding. The first case is when the waveguides have similar properties where the difference in the characteristic speeds is $c - 1 = \mathcal{O}(\varepsilon)$. When the properties within the waveguide are similar, a solitary wave within the bonded area transforms into a radiating solitary wave [48]. If we substitute

$$f = \varepsilon\tilde{f}, \quad g = \varepsilon\tilde{g}, \quad t = \sqrt{\varepsilon}\tilde{t}, \quad x = \sqrt{\varepsilon}\tilde{x}, \quad \delta = \varepsilon^2\tilde{\delta}, \quad \gamma = \varepsilon^2\tilde{\gamma}, \tag{2.98}$$

into (2.88), we can rewrite the cRB equations as

$$\begin{aligned} f_{tt} - f_{xx} &= \varepsilon[-6(f^2)_{xx} + 2f_{ttxx} - 2\delta(f-g)], \\ g_{tt} - c^2 g_{xx} &= \varepsilon[-6\alpha(g^2)_{xx} + 2\beta g_{ttxx} + 2\gamma(f-g)], \end{aligned} \tag{2.99}$$

where the tildes are omitted for simplicity of notation. The weakly-nonlinear solutions for the coupled system are given by

$$f(x,t) = I(\xi,T) + R(\eta,T) + \varepsilon P(\xi,\eta,T) + \mathcal{O}(\varepsilon^2), \tag{2.100}$$

$$g(x,t) = S(\xi,T) + G(\eta,T) + \varepsilon Q(\xi,\eta,T) + \mathcal{O}(\varepsilon^2), \tag{2.101}$$

where the characteristic variables are $\xi = x - t$, $\eta = x + t$ and $T = \varepsilon t$. I and S represent the incident waves in the upper and lower waveguides, respectively, and R and G represent the reflective waves in the upper and lower waveguides, respectively.

The term $c^2 - 1$ can be written as $c^2 - 1 = (c-1)(c+1)$. Since $c \approx 1$, it follows that $c + 1 \approx 2$. Additionally, as $c - 1 = \mathcal{O}(\varepsilon)$, we have

$$c^2 - 1 \approx 2(c-1) \approx 2\mathcal{O}(\varepsilon). \tag{2.102}$$

Thus, $c^2 - 1$ is of order $\mathcal{O}(\varepsilon)$, allowing us to add $(c^2-1)g_{xx}$ to both sides of the second equation in (2.99), enabling the system to be rewritten as

$$\begin{aligned} f_{tt} - f_{xx} &= \varepsilon\left[-6(f^2)_{xx} + 2f_{ttxx} - 2\delta(f-g)\right], \\ g_{tt} - g_{xx} &= \varepsilon\left[-6\alpha(g^2)_{xx} + 2\beta g_{ttxx} + 2\gamma(f-g) + \frac{c^2-1}{\varepsilon}g_{xx}\right]. \end{aligned} \tag{2.103}$$

Substituting the respective partial derivatives of (2.100) and (2.101) into (2.103) and applying time averaging as in Sections 2.1.2 and 2.2.2, gives the leading order coupled Ostrovsky equations

$$\begin{aligned} (I_T - 6II_\xi + \beta I_{\xi\xi\xi})_\xi - \delta(I-S) &= 0, \\ \left(S_T - 6\alpha(SS_\xi) + \beta S_{\xi\xi\xi} + \frac{c^2-1}{2\varepsilon}S_\xi\right)_\xi + \gamma(I-S) &= 0, \end{aligned} \tag{2.104}$$

and

$$\begin{aligned} (R_T - 6RR_\eta + \beta R_{\eta\eta\eta})_\eta - \delta(R-G) &= 0, \\ \left(G_T - 6\alpha(GG_\eta) + \beta G_{\eta\eta\eta} + \frac{c^2-1}{2\varepsilon}G_\eta\right)_\eta + \gamma(R-G) &= 0. \end{aligned} \tag{2.105}$$

The higher-order corrections are denoted as

$$\begin{aligned} P(\xi,\eta,T) &= 3\left(I_\xi \int R\ \mathrm{d}\eta + \int I\ \mathrm{d}\xi R_\eta + 2IR\right) + \phi_1(\xi,X) + \psi_1(\eta,X), \\ Q(\xi,\eta,T) &= 3\alpha\left(S_\xi \int G\ \mathrm{d}\eta + G_\eta \int S\ \mathrm{d}\xi + 2SG\right) + \phi_2(\xi,X) + \psi_2(\eta,X), \end{aligned} \tag{2.106}$$

where $\phi_1(\xi, X)$, $\psi_1(\eta, X)$, $\phi_2(\xi, X)$ and $\psi_2(\eta, X)$ are integration constants. At $t = 0$ the leading order weakly-nonlinear solutions (2.100) - (2.101) are represented as

$$f|_{t=0} = (I(\xi, T) + R(\eta, T))|_{t=0} = F(x), \quad \text{and} \quad g|_{t=0} = (S(\xi, T) + G(\eta, T))|_{t=0} = G(x). \tag{2.107}$$

Differentiating the leading order solutions (2.100) and (2.101) with respect to t at $x = 0$ gives

$$f_t(0, t) = (-cI_\xi + cR_\eta)|_{x=0} = f_1'(t) = V(x), \quad \text{and} \quad g_t(0, t) = (-cS_\xi + cG_\eta)|_{x=0} = f_2'(t) = W(x). \tag{2.108}$$

The f_x and g_x derivative terms at $x = 0$ can be denoted as

$$cf_x(0, t) = (cI_\xi + cR_\eta)|_{x=0} = cg_1(t) \quad \text{and} \quad cg_x(0, t) = (cS_\xi + cG_\eta)|_{x=0} = cg_2(t). \tag{2.109}$$

This leads to the leading order initial $t = \mathcal{O}(1)$ evolution of the Cauchy data, which is described by the classical d'Alembert's solution

$$\begin{aligned} R|_{x=0} &= \frac{1}{2c}\left(f_1(t) + c\int_{-l}^{t} g_1(s)\ \mathrm{d}s\right), \quad I|_{x=0} = \frac{1}{2c}\left(f_1(t) - c\int_{-l}^{t} g_1(s)\ \mathrm{d}s\right), \\ G|_{x=0} &= \frac{1}{2c}\left(f_2(t) + c\int_{-l}^{t} g_2(s)\ \mathrm{d}s\right), \quad S|_{x=0} = \frac{1}{2c}\left(f_2(t) - c\int_{-l}^{t} g_2(s)\ \mathrm{d}s\right). \end{aligned} \tag{2.110}$$

As we assume the initial conditions are sufficiently rapidly decaying at both $\pm\infty$, the slow variable $T = \varepsilon t$ helps describe the subsequent $t = \mathcal{O}(\varepsilon^{-1})$ evolution of the given initial data by looking for the weakly-nonlinear solution of the Cauchy problem (2.99), (2.107) and (2.108) in the form of asymptotic multiple-scales expansions. Similarly, initial conditions for $\mathcal{O}(\varepsilon)$ also yield initial evolution of the Cauchy data according to the classical d'Alembert solution. Another case explored in [72] was when the difference in speed between the two wave operators was $c - 1 = \mathcal{O}(1)$, and so two sets of characteristic variables were introduced instead. Applying a similar process as in the above case leads to uncoupled leading order solutions.

2.4 Summary

In this chapter we have discussed the motivation for considering nonlinear wave propagation in layered elastic waveguides. Firstly, in Section 2.1.1 we considered a single elastic waveguide and defined some of its properties such as its Poisson ratio, kinetic energy density and density of potential energy. From this we derived a Boussinesq equation describing the longitudinal displacement of the nonlinear wave propagating

within the elastic waveguide using nonlinear elasticity theory. Then in Section 2.1.2 we considered a weakly-nonlinear solution to describe the wave propagation in the left and right directions.

The next case we considered was a two-layered waveguide with delamination on the right in Section 2.2. We utilised the same nonlinear elasticity theory as for a single elastic waveguide from Section 2.2.1. Therefore, an interesting case that will be explored in a Chapter 5 is, what would the effect be on the entire structure if we add perfect bonding on the right thus effectively sandwiching the delaminated region? How would different lengths of delamination affect the wave propagation and consequently the integrity of the structure?

We then examined two models; FPU and cKG. The FPU model was used to derive the coupled Boussinesq equations in Section 2.3. We then explored the asymptotic behaviour and dispersion relation of the symmetric case for the coupled Boussinesq equations before finding the weakly-nonlinear solutions within the context of a scattering problem in Section 2.3.5. From this, in Chapter 4 we can now explore scattering problems where the longitudinal displacement in the lower waveguide is present and thus both parts of the structure are modelled by coupled Boussinesq equations. In Section 2.3.3 specifically, the coupled Boussinesq equations contained dispersion coefficient terms which factored in soft bonding within layered waveguides, and although this has been somewhat explored in [48] as mentioned previously, this was when the characteristic speeds were similar. We will explore what would happen in the case of distinct characteristic speeds in Chapters 3 and 4.

Chapter 3

Scattering of an Ostrovsky wave packet in a delaminated waveguide

In this chapter, we will investigate the scattering of an Ostrovsky wave packet within the upper waveguide of a two-layered structure. This structure consists of an initial small delaminated region, followed eventually by a second delaminated region, with soft bonded layers on either side of the second delaminated region. The lower waveguide is assumed to have a significantly higher density than the upper waveguide, resulting in a system described by Boussinesq and Boussinesq–Klein–Gordon (BKG) equations.

Next, we intend to derive and compare a direct numerical model with a semi-analytical approach, which consists of several matched asymptotic multiple-scale expansions. For the semi-analytical approach, we expect the leading order solution to be described by Ostrovsky equations in the soft bonded region and by Korteweg-de Vries (KdV) equations in the delaminated region, as shown in previous studies [47, 48]. We hope to demonstrate a strong agreement between the semi-analytical approach and the direct numerical simulation.

We will then seek theoretical predictions for wave speed using the dispersion relation and for wave amplitude using the Inverse Scattering Transform (IST) [48, 75]. We aim for strong agreement between these theoretical predictions and the numerical simulations to validate these methods as effective tools. We aim to plot the wave amplitude and phase shift in the final soft bonded region for structures of various delamination lengths. Finally we will demonstrate the process of scaling the non-dimensional results to a physical context, illustrating through an example involving a PMMA bar. The results of this chapter are partially summarised in [93].

3.1 Model formulation

Wave scattering within the upper waveguide of two distinct two-layered structures, as depicted in Figure 3.1 and inspired by the experimental setup arrangement outlined in [46], will be explored in this chapter. Figure 3.1(b) depicts a finite delamination case. In this scenario, a long longitudinal soliton is generated within the initial small delaminated region of the upper waveguide from x_0 to x_1 where the longitudinal displacement is denoted by $u^{(1)}$. The structure then includes two soft bonded regions from x_1 to x_2 and x_3 to x_4 where the longitudinal displacements are $u^{(2)}$ and $u^{(4)}$, respectively. These soft bonded regions 'sandwich' the delaminated region, which is from x_2 to x_3, where the longitudinal displacement is $u^{(3)}$. Figure 3.1(a) illustrates a semi-infinite delamination case, featuring the same structure as Figure 3.1(b), but without the final bonded region.

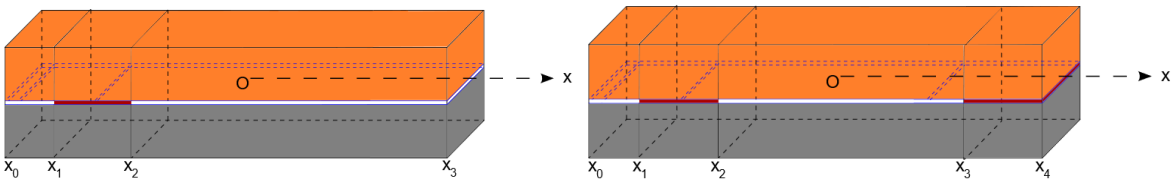

(a) Infinite delamination case. (b) Finite delamination case.

Figure 3.1: Examples of the bi-layer structure with an initial delaminated region for $x_0 < x < x_1$, a soft bonded region for $x_1 < x < x_2$ and either (a) a delaminated region for $x_2 < x < x_3$, or (b) a delaminated region for $x_2 < x < x_3$ followed by another soft bonded region for $x_3 < x < x_4$. In both cases we assume that the material in the lower layer has a significantly higher density than the material in the upper layer.

The scattering of long longitudinal solitary waves within a similar structure was examined in [48], focusing on cases where the wave characteristic speed in the lower layer was $c - 1 = \mathcal{O}(\varepsilon)$, with ε representing a small amplitude parameter. In that scenario, a radiating solitary wave was generated within the waveguides in the bonded sections of the structure and became separated from its co-propagating tail in the delaminated sections. In our study, each section of the waveguide is also made of the same material throughout, however, the lower layer is considered to be much denser, making the discrepancy in characteristic speeds more significant. Consequently, we assume that longitudinal displacements in the lower layer are essentially zero and thus negligible.

The longitudinal displacement within the upper waveguide can be modelled by the following system

of Boussinesq and Boussinesq-Klein-Gordan (BKG) equations

$$u_{tt}^{(1)} - u_{xx}^{(1)} = 2\varepsilon\left(-6u_x^{(1)}u_{xx}^{(1)} + \beta u_{ttxx}^{(1)}\right), \tag{3.1}$$

$$u_{tt}^{(2)} - u_{xx}^{(2)} = 2\varepsilon\left(-6u_x^{(2)}u_{xx}^{(2)} + \beta u_{ttxx}^{(2)} - \gamma u^{(2)}\right), \tag{3.2}$$

$$u_{tt}^{(3)} - u_{xx}^{(3)} = 2\varepsilon\left(-6u_x^{(3)}u_{xx}^{(3)} + \beta u_{ttxx}^{(3)}\right), \tag{3.3}$$

$$u_{tt}^{(4)} - u_{xx}^{(4)} = 2\varepsilon\left(-6u_x^{(4)}u_{xx}^{(4)} + \beta u_{ttxx}^{(4)} - \gamma u^{(4)}\right), \tag{3.4}$$

where β is a nonlinear coefficient describing the physical and geometrical properties of the waveguide. We set $\beta = 1$, and therefore, for most of the work in this chapter, we omit it for simplicity. The continuity of longitudinal displacement at the interfaces between the sections is given by

$$u^{(i)}\Big|_{x=x_i} = u^{(i+1)}\Big|_{x=x_i}, \;\; i = 1, 2, 3, \tag{3.5}$$

and the continuity of normal stress of these interfaces is

$$u_x^{(i)} + 2\varepsilon\left[-3\left(u_x^{(i)}\right)^2 + u_{ttx}^{(i)}\right]\Big|_{x=x_i} = u_x^{(i+1)} + 2\varepsilon\left[-3\left(u_x^{(i+1)}\right)^2 + u_{ttx}^{(i+1)}\right]\Big|_{x=x_i}, \;\; i = 1, 2, 3. \tag{3.6}$$

Equations (3.1)–(3.4) are scaled with coefficients chosen specifically to ensure that the leading order solutions derived from the weakly-nonlinear solution are in canonical form. Following the method outlined in [48], we differentiate (3.1)–(3.4) with respect to x and set $u_x^{(i)} = f^{(i)}$ to describe the longitudinal strain of the system as

$$f_{tt}^{(1)} - f_{xx}^{(1)} = 2\varepsilon\left(-3\left(f^{(1)^2}\right)_{xx} + f_{ttxx}^{(1)}\right), \tag{3.7}$$

$$f_{tt}^{(2)} - f_{xx}^{(2)} = 2\varepsilon\left(-3\left(f^{(2)^2}\right)_{xx} + f_{ttxx}^{(2)} - \gamma f^{(2)}\right), \tag{3.8}$$

$$f_{tt}^{(3)} - f_{xx}^{(3)} = 2\varepsilon\left(-3\left(f^{(3)^2}\right)_{xx} + f_{ttxx}^{(3)}\right), \tag{3.9}$$

$$f_{tt}^{(4)} - f_{xx}^{(4)} = 2\varepsilon\left(-3\left(f^{(4)^2}\right)_{xx} + f_{ttxx}^{(4)} - \gamma f^{(4)}\right). \tag{3.10}$$

The continuity conditions may also be expressed in terms of longitudinal strain as follows:

$$\int_{x_{i-1}}^{x_i} f^{(i)}\,\mathrm{d}x = -\int_{x_i}^{x_{i+1}} f^{(i+1)}\,\mathrm{d}x, \;\; i = 1, 2, 3, \tag{3.11}$$

and

$$f^{(i)} + 2\varepsilon \left[-3 \left(f^{(i)} \right)^2 + f_{tt}^{(i)} \right] \Big|_{x=x_i} = f^{(i+1)} + 2\varepsilon \left[-3 \left(f^{(i+1)} \right)^2 + f_{tt}^{(i+1)} \right] \Big|_{x=x_i}, \quad i = 1, 2, 3. \tag{3.12}$$

3.2 Weakly-nonlinear solution

For each region, we will construct a weakly-nonlinear solution based on asymptotic multiple-scale expansions, which describes the wave propagation. This solution includes a transmitted and reflected wave at leading order, along with higher-order corrections. Notably, in the final region, there is no reflected wave, while in the initial region, an incident wave is present instead of a transmitted wave. All functions in the expansion and their derivatives are assumed to be bounded and sufficiently rapidly decaying at infinity, consistent with assumptions in [47, 48] and physical observations. We will then substitute these expansions and their partial derivatives into the system of equations (3.7) – (3.10) and apply the space-averaging method to derive the leading order solutions. This approach parallels the methods developed in [45, 47, 48] for wave propagation in layered waveguides with perfect and soft bonding. Finally, we will apply the continuity conditions to obtain 'initial conditions' for these derived equations.

3.2.1 Region 1: first delaminated section

We consider the first region of the structures in Figure 3.1, where the two layers are delaminated. This region is governed by the Boussinesq equation (3.7). A solitary wave is generated within the waveguide in this region, consistent with the experiments described in [46]. Therefore, we construct an asymptotic multiple-scale expansion of the type

$$f^{(1)}(x,t) = I(\xi, X) + R^{(1)}(\eta, X) + \varepsilon P^{(1)}(\xi, \eta, X) + \mathcal{O}(\varepsilon^2),$$

where $\xi = x - t$ and $\eta = x + t$ represent the fast "spatial" characteristic variables, and $X = \varepsilon x$ denotes the slow "temporal" space variable. The leading order incident and reflected waves are represented by I and $R^{(1)}$ respectively, while the higher-order correction is represented by $P^{(1)}$. Substituting this asymptotic expansion into (3.7) gives

$$-2P_{\xi\eta}^{(1)} = (I_X - 6II_\xi + I_{\xi\xi\xi})_\xi + (R_X^{(1)} - 6R^{(1)}R_\eta^{(1)} + R_{\eta\eta\eta}^{(1)})_\eta - 6(2I_\xi R_\eta^{(1)} + R_{\eta\eta}^{(1)} I + I_{\xi\xi} R^{(1)}). \tag{3.13}$$

Assuming the left boundary at x_0 is far away from the boundary at x_1 and tends to negative infinity, we can take $x_0 \to -\infty$. We then average the left-hand side of equation (3.13) by holding ξ constant and we

integrating (3.13) with respect to the fast spatial variable x, yielding

$$\lim_{x_0\to-\infty}\frac{1}{x_1-x_0}\int_{x_0}^{x_1}-2P^{(1)}_{\xi\eta}\,\mathrm{d}x, \tag{3.14}$$

in the reference frame moving with the linear speed of right- and left-propagating waves (at constant ξ or η). As mentioned earlier, all functions and their derivatives are assumed to remain bounded and sufficiently rapidly decay at infinity. This assumption is necessary to avoid secular terms in the asymptotic expansions. When applying the averaging, similarly to Section 2.1.2, at constant ξ we obtain

$$\lim_{x_0\to-\infty}\frac{-2}{x_1-x_0}\int_{x_0}^{x_1}P^{(1)}_{\xi\eta}\,\mathrm{d}x=\lim_{x_0\to-\infty}\frac{-2}{2(x_1-x_0)}\int_{2x_0-\xi}^{2x_1-\xi}P^{(1)}_{\xi\eta}\,\mathrm{d}\eta=\lim_{x_0\to-\infty}\frac{-2}{2(x_1-x_0)}\left[P^{(1)}_{\xi}\right]_{2x_0-\xi}^{2x_1-\xi}=0. \tag{3.15}$$

Now, by averaging the right-hand side of (3.13), we get

$$0=\lim_{x_0\to-\infty}\frac{1}{2(x_1-x_0)}\left[I_X-6II_\xi+I_{\xi\xi\xi}\right]_{2x_0-\xi}^{2x_1-\xi} \tag{3.16}$$

$$+(R^{(1)}_X-6R^{(1)}R^{(1)}_\eta+R^{(1)}_{\eta\eta\eta})_\eta\lim_{x_0\to-\infty}\left[\frac{\eta}{2(x_1-x_0)}\right]_{2x_0-\xi}^{2x_1-\xi} \tag{3.17}$$

$$-\lim_{x_0\to-\infty}\frac{1}{2(x_1-x_0)}\int_{2x_0-\xi}^{2x_1-\xi}6(2I_\xi R^{(1)}_\eta+R^{(1)}_{\eta\eta}I+I_{\xi\xi}R^{(1)})\,\mathrm{d}\eta, \tag{3.18}$$

the terms in the first and third line become zero when evaluated, thus we obtain the following KdV equation

$$R^{(1)}_X-6R^{(1)}R^{(1)}_\eta+R^{(1)}_{\eta\eta\eta}=0. \tag{3.19}$$

A similar process is applied when averaging at constant η, yielding

$$I_X-6II_\xi+I_{\xi\xi\xi}=0. \tag{3.20}$$

Substituting (3.19) and (3.20) into (3.13), then rearranging and integrating with respect to the characteristic variables, gives

$$P^{(1)}=3\left(2IR^{(1)}+R^{(1)}_\eta\int I\mathrm{d}\xi+I_\xi\int R^{(1)}\mathrm{d}\eta\right)+\phi^{(1)}(\xi,X)+\psi^{(1)}(\eta,X), \tag{3.21}$$

where $\phi^{(1)}$, $\psi^{(1)}$ are arbitrary functions.

3.2.2 Region 2: first soft bonded section

Now, we consider the soft bonded region, where we derive Ostrovsky equations to govern the leading order wave behaviour through the constructed weakly-nonlinear solutions [23, 94]. The weakly-nonlinear solution is assumed to be

$$f^{(2)}(x,t) = T^{(2)}(\xi, X) + R^{(2)}(\eta, X) + \varepsilon P^{(2)}(\xi, \eta, X) + \mathcal{O}(\varepsilon^2),$$

where ξ, η and X are the same as the first region. The function $T^{(2)}$ represents the transmitted wave generated by the incident wave in the first region, while $R^{(2)}$ represents the reflected wave. The higher-order correction in this section is denoted by $P^{(2)}$. Substituting (3.2.2) and its respective partial derivatives into (3.8) gives

$$\begin{aligned} -2P^{(2)}_{\xi\eta} = &\left(T^{(2)}_X - 6T^{(2)}T^{(2)}_\xi + T^{(2)}_{\xi\xi\xi}\right)_\xi + \left(R^{(2)}_X - 6R^{(2)}R^{(2)}_\eta + R^{(2)}_{\eta\eta\eta}\right)_\eta - \gamma\left(T^{(2)} + R^{(2)}\right) \\ &- 6\left(2T^{(2)}_\xi R^{(2)}_\eta + T^{(2)}R^{(2)}_{\eta\eta} + T^{(2)}_{\xi\xi}R^{(2)}\right). \end{aligned} \tag{3.22}$$

The solution is considered over the period of time from when the wave enters the second region at the boundary $x = x_1$ to when it exits at the boundary $x = x_2$. As with the first region, we assume that the boundary at $x = x_2$ is sufficiently far from $x = x_1$, allowing us to apply averaging by integrating the left-hand side of (3.22) with respect to x, leading to the expression:

$$\lim_{x_1 \to -\infty} \frac{1}{x_2 - x_1} \int_{x_1}^{x_2} -2P^{(2)}\,\mathrm{d}x. \tag{3.23}$$

When averaging the left-hand side of (3.22) with respect to either constant ξ or η, the higher-order correction function $P^{(2)}$ becomes zero, similar to the observations in the first section. Therefore, applying the averaging to the right-hand side of (3.22) at constant ξ and η yields

$$\left(T^{(2)}_X - 6T^{(2)}T^{(2)}_\xi + T^{(2)}_{\xi\xi\xi}\right)_\xi = \gamma T^{(2)}, \tag{3.24}$$

$$\left(R^{(2)}_X - 6R^{(2)}R^{(2)}_\eta + R^{(2)}_{\eta\eta\eta}\right)_\eta = \gamma R^{(2)}, \tag{3.25}$$

respectively, where (3.24) and (3.25) are Ostrovsky equations [23]. Therefore, substituting (3.24) and (3.25) into (3.22), rearranging the resulting expression, and then integrating with respect to ξ and η

yields

$$P^{(2)} = 3\left(T^{(2)}_{\xi}\int R^{(2)}\ \mathrm{d}\eta + R^{(2)}_{\eta}\int T^{(2)}\ \mathrm{d}\xi + 2T^{(2)}R^{(2)}\right) + \phi^{(2)}(\xi, X) + \psi^{(2)}(\eta, X), \tag{3.26}$$

where $\phi^{(2)}(\xi, X)$ and $\psi^{(2)}(\eta, X)$ are arbitrary integration constants.

3.2.3 Region 3: second delaminated section

We now consider the third region of the bar, where the two layers are delaminated, using a similar methodology to Sections 3.2.1 - 3.2.2. Therefore, the calculations in this section can be summarised. We construct a weakly-nonlinear solution for (3.9) of the form

$$f^{(3)}(x,t) = T^{(3)}(\xi, X) + R^{(3)}(\eta, X) + \varepsilon P^{(3)}(\xi, \eta, X) + \mathcal{O}(\varepsilon^2),$$

where the characteristic variables have the same meaning as before. The averaging used in this region takes the form

$$\lim_{x_2\to-\infty}\frac{1}{x_3 - x_2}\int_{x_2}^{x_3}\ldots\,\mathrm{d}x. \tag{3.27}$$

Substituting the weakly-nonlinear expansion into (3.9) and then averaging at constant η and ξ, we obtain

$$T^{(3)}_X - 6T^{(3)}T^{(3)}_{\xi} + T^{(3)}_{\xi\xi\xi} = 0, \tag{3.28}$$

$$R^{(3)}_X - 6R^{(3)}R^{(3)}_{\eta} + R^{(3)}_{\eta\eta\eta} = 0, \tag{3.29}$$

respectively, and the higher-order correction is found as

$$P^{(3)} = 3\left(2T^{(3)}R^{(3)} + R^{(3)}_{\eta}\int T^{(3)}\,\mathrm{d}\xi + T^{(3)}_{\xi}\int R^{(3)}\,\mathrm{d}\eta\right) + \phi^{(3)}(\xi, X) + \psi^{(3)}(\eta, X). \tag{3.30}$$

where $\phi^{(3)}$, $\psi^{(3)}$ are arbitrary functions.

3.2.4 Region 4: second bonded section

Now, for the fourth region, we construct a weakly-nonlinear solution of the form

$$f^{(4)}(x,t) = T^{(4)}(\xi, X) + \varepsilon P^{(4)}(\xi, \eta, X) + \mathcal{O}(\varepsilon^2),$$

with the averaging in this region given as

$$\lim_{x_4\to\infty}\frac{1}{x_4-x_3}\int_{x_3}^{x_4}\ldots\,\mathrm{d}x. \tag{3.31}$$

We obtain the equation

$$\left(T_X^{(4)}-6T^{(4)}T_\xi^{(4)}+T_{\xi\xi\xi}^{(4)}\right)_\xi=\gamma T^{(4)}, \tag{3.32}$$

with higher-order correction

$$P^{(4)}=\phi^{(4)}(\xi,X)+\psi^{(4)}(\eta,X), \tag{3.33}$$

where $\phi^{(4)}$, $\psi^{(4)}$ are arbitrary functions. If the incident wave is right-propagating and there is no boundary to generate a reflected wave in this final region, then there should be no left-propagating wave field in this region [45, 47, 48]. Therefore we must have $\psi^{(4)}=0$. As mentioned earlier, in [48], the waveguides were of similar materials and had close characteristic speeds, which led to the weakly-nonlinear solution in the bonded regions being described by coupled Ostrovsky equations and in the delaminated regions by KdV equations. In contrast, for the limiting case considered here, the weakly-nonlinear solutions in the bonded regions are described by single Ostrovsky equations. This also occurred in [72, 94, 95] when using the time-averaged derivation for the initial-value problem for the coupled regularised Boussinesq (cRB) equations.

With the weakly-nonlinear solution now defined for each section of the structure shown in Figure 3.1(b), this structure could be extended by adding additional soft bonded or delaminated regions. The weakly-nonlinear solution in these new regions could be constructed similarly to the approach taken in sections 3.2.1 - 3.2.4. However, this is beyond the scope of this thesis.

3.3 Initial conditions

3.3.1 Matching at the boundaries

We now use the continuity conditions (3.11) and (3.12) to determine 'initial conditions' for the equations derived in Sections 3.2.1 - 3.2.4. By substituting the weakly-nonlinear solution into the continuity conditions, we can express the value of the functions in the subsequent region at the interface between the two regions in terms of the value of the corresponding function in the previous region.

Let's begin with the initial continuity condition at $x=x_1$, the interface between the first and second regions. We examine this condition for wave displacements during the time interval before the waves reach the boundary between the second and third regions. We also assume that the displacement at negative

infinity is zero, which corresponds to zero mean initial conditions, where zero mean refers to the average initial displacement over the entire domain being zero. By differentiating (3.11) with respect to time at x_1, we derive a relation between the strain rates of the form

$$\int_{x_0}^{x_1} f_t^{(1)} \, \mathrm{d}x = -\int_{x_1}^{x_2} f_t^{(2)} \, \mathrm{d}x. \tag{3.34}$$

Since we assume the waves haven't yet reached the interface between the second and third sections of the bar, we can exclude the reflected wave $R^{(2)}$ from the calculation at this boundary for right-propagating waves. By substituting the weakly-nonlinear solutions derived in Sections 3.2.1 and 3.2.2 into (3.34) we obtain at leading order

$$\int_{x_0}^{x_1} \left(I_\xi - R_\eta^{(1)} \right) \mathrm{d}x = -\int_{x_1}^{x_2} T_\xi^{(2)} \, \mathrm{d}x. \tag{3.35}$$

Recalling that $\xi = x - t$ and $\eta = x + t$, and noting that x appears linearly, we can obtain an expression at $x = x_1$ by integrating with respect to the characteristic variables. Given that the strain waves are localised and have zero mean, this expression will be zero when evaluated at $x = x_0$ or $x = x_2$. Therefore, from (3.35), we obtain

$$I|_{x=x_1} - R^{(1)}|_{x=x_1} = T^{(2)}|_{x=x_1}. \tag{3.36}$$

To establish a unique relation among the three wave quantities, we use the second continuity condition. By substituting the relevant weakly-nonlinear solutions into (3.12) at leading order, we obtain

$$I|_{x=x_1} + R^{(1)}|_{x=x_1} = T^{(2)}|_{x=x_1}. \tag{3.37}$$

We can now find 'initial conditions' for the reflected wave in the first section of the bar and the transmitted wave in the second section of the bar, expressed in terms of the given incident wave. Explicitly

$$R^{(1)}|_{x=x_1} = C_R^{(1)} I|_{x=x_1}, \quad T^{(2)}|_{x=x_1} = C_T^{(1)} I|_{x=x_1}, \tag{3.38}$$

where we have the reflection coefficient $C_R^{(1)} = 0$ and transmission coefficient $C_T^{(1)} = 1$, which is consistent with previous works for a perfectly bonded waveguide [45,47] and for a layered bar with soft bonding [48]. These coefficients indicate complete transmission of the incident wave at leading order, consistent with the material being uniform across each section of the bar.

The same approach can be applied to the interfaces between the second and third sections, as well as the third and fourth sections of the bar, assuming that the waves are traveling in these sections and have not yet reflected back to the left boundary. Therefore the 'initial conditions' for the reflected and

transmitted waves are

$$R^{(2)}|_{x=x_2} = C_R^{(2)} T^{(2)}|_{x=x_2}, \quad T^{(3)}|_{x=x_2} = C_T^{(2)} T^{(2)}|_{x=x_2}, \tag{3.39}$$

$$R^{(3)}|_{x=x_3} = C_R^{(3)} T^{(3)}|_{x=x_3}, \quad T^{(4)}|_{x=x_3} = C_T^{(3)} T^{(3)}|_{x=x_3}. \tag{3.40}$$

Since the material remains consistent across all sections of the bar also, $C_R^{(2,3)} = 0$ and $C_T^{(2,3)} = 1$. We consider the continuity conditions at leading order, but this approach could be extended to higher-order corrections.

3.4 Numerical methods

We will use a direct numerical method on the system of equations (3.1) - (3.4) along with the continuity conditions (3.5) and (3.6), following the methodology outlined in [77] and Appendix A.1, with grid resolutions of $\Delta x = 0.01$ in space x, and $\Delta t = 0.01$ in time t. We will compare these results with those from a semi-analytical approach, where we solve the KdV and Ostrovsky equations using a pseudospectral method as detailed in [48] and Appendices B.1 and B.2. For both the KdV and Ostrovsky equations, we use $\Delta\xi = 0.1$ for the step size in the characteristic variable ξ, and $\Delta X = 0.001$ the step size in X. The number of points in the domain for the Discrete Fast Fourier Transform (DFFT) in our pseudospectral method is expressed as

$$N = 2^d, \tag{3.41}$$

where d is a chosen parameter that ensures there are enough points in the domain.

3.4.1 Zero mean initial condition

The initial condition is assumed to be the solitary wave solution of the KdV equation within the first region of the waveguide. Since the leading order solution in the soft bonded section is governed by the Ostrovsky equation, which requires a zero mean initial condition, we use the approach outlined in [48, 96] to introduce a pedestal term that ensures this function has zero mean. Specifically, we take

$$I(\xi, x_0) = A\,\mathrm{sech}^2\left(\frac{\xi + x_0}{\Lambda}\right) - \alpha_0\left[A\,\mathrm{sech}^2\left(\frac{\xi + x_0 + x_1}{\Lambda S}\right) + A\,\mathrm{sech}^2\left(\frac{\xi + x_0 - x_1}{\Lambda S}\right)\right], \tag{3.42}$$

where $A = -v/2$, $\Lambda = 2/\sqrt{v}$, and we establish

$$\alpha_0 = \frac{\tanh\left(\frac{L}{\Lambda S}\right)}{S\left(\tanh\left(\frac{L+x_0}{\Lambda S}\right) + \tanh\left(\frac{L-x_0}{\Lambda S}\right)\right)}. \tag{3.43}$$

Here, x_0 represents the initial phase shift, x_1 is selected such that the pedestal terms lie close to the solitary wave, and S denotes a scale factor for the width of the pedestal. In all instances, we opt for $S = 10$ and $x_1 = 5$. Considering the initial conditions for equations (3.1) – (3.4), we integrate the strain solitary wave solution of the Boussinesq equation from (3.7), yielding

$$u(x,0) = \tilde{A}\tilde{\Lambda}\left[\tanh\left(\frac{x+x_0}{\tilde{\Lambda}}\right) - 1\right] - \alpha_0\tilde{A}\tilde{\Lambda}S\left[\tanh\left(\frac{x+x_0+x_1}{\tilde{\Lambda}S}\right) + \tanh\left(\frac{x+x_0-x_1}{\tilde{\Lambda}S}\right) - 2\right], \tag{3.44}$$

$$\begin{aligned} u(x,\kappa) = {} & \tilde{A}\tilde{\Lambda}\left[\tanh\left(\frac{x-\kappa v+x_0}{\tilde{\Lambda}}\right) - 1\right] \\ & - \alpha_0\tilde{A}\tilde{\Lambda}S\left[\tanh\left(\frac{x-\kappa v+x_0+x_1}{\tilde{\Lambda}S}\right) + \tanh\left(\frac{x-\kappa v+x_0-x_1}{\tilde{\Lambda}S}\right) - 2\right], \end{aligned} \tag{3.45}$$

where we have the coefficients

$$\tilde{A} = -\frac{v_1^2-1}{4\varepsilon}, \quad \tilde{\Lambda} = 2v_1\sqrt{\frac{2\varepsilon}{v_1^2-1}}, \tag{3.46}$$

and v_1 is related to v by the approximate relation $v_1 = 1+\varepsilon v+\mathcal{O}(\varepsilon^2)$ [48]. Note that the initial condition $u(x,0)$ pertains to the entire waveguide, while the initial condition for $u^{(i)}$ is extracted from $u(x,0)$ within the respective domain.

3.4.2 Amplitude of solitons in delaminated region

The IST theory [12] tells us that localised initial conditions for the KdV equation are known to result in either a series of solitons accompanied by dispersive radiation (unless the continuous spectrum is zero), or only generate dispersive radiation. When the initial condition is a soliton, the peak amplitudes of the resulting solitons can be determined analytically [45, 53]. In our case, we anticipate that the wave entering the delaminated region of the bar will form an Ostrovsky wave packet [23]. To derive quantitative predictions for the peak amplitudes of the generated solitons, we apply the IST to the KdV equation (3.28), derived in Section 3.2.3, following a methodology similar to that used in [48] for a radiating solitary wave.

Let us consider the solution of an initial-value problem (IVP) for the KdV equation

$$U_\tau - 6UU_\chi + U_{\chi\chi\chi} = 0, \quad U|_{\tau=0} = U_0(\chi), \tag{3.47}$$

on the infinite line, with a sufficiently rapidly decaying initial condition $U_0(\chi)$. The IVP (3.47) is associated

with the following spectral problem for the Schrödinger equation

$$\Psi_{\chi\chi} + [\lambda - U_0(\chi)]\,\Psi = 0, \tag{3.48}$$

where λ represents the spectral parameter [12]. The parameters of the solitons are defined by the discrete spectrum of (3.48), hence, our objective is to numerically describe this spectrum using a shooting method [97]. Given the negative nonlinear coefficient, the discrete spectrum is constrained by the minimum of the initial condition and zero [98], thus establishing a range within which to solve for the discrete eigenvalues. The eigenfunctions of the Schrödinger equation exhibit the asymptotic behaviour

$$\Psi(\chi) \sim \begin{cases} e^{r\chi}, & \text{as } \chi \to -\infty, \\ e^{-r\chi}, & \text{as } \chi \to \infty, \end{cases} \tag{3.49}$$

where $\lambda = -r^2$. Therefore we rewrite (3.48) as a boundary value problem in the form

$$\Psi_\chi = \Phi, \quad \Phi_\chi = (U_0(\chi) - \lambda)\,\Psi, \tag{3.50}$$

where we solve this system from $\chi = a$ to $\chi = b$. The solution is normalised by setting $\Psi(a) = 1$, $\Phi(a) = r$, and the system is solved using a fourth-order Runge-Kutta method. The ratio of Φ and Ψ is evaluated at the right boundary and compared with the relation $\Phi(b)/\Psi(b) = -r$ to determine whether r is an eigenvalue.

3.4.3 Base case simulations

Firstly, we examine the wave scattering within the upper waveguide of the structure with infinite delamination, as depicted in Figure 3.1(a), and compare the results from direct numerical simulations with the semi-analytical results. The comparative analysis of the waves in each region, using both methods, is illustrated in Figure 3.2, showing excellent agreement throughout. Notably, as the incident soliton from the initial delaminated region propagates into the bonded region, it evolves into an Ostrovsky wave packet, consistent with the anticipated outcomes from the initial-value problem detailed in [94]. This wave packet subsequently undergoes fission into solitons as it continues propagating through the delaminated region. At this point, the leading soliton is clearly separated from the trailing radiation. However, the remaining peaks have not yet separated and become distinct from one another and continue to move on a zero background, making it difficult to clearly identify them as solitons. This observation is consistent with findings in [47, 77] and experimental observations [44, 46, 99]. Enhanced agreement could potentially

be achieved through the incorporation of higher-order terms or the reduction of the ε value.

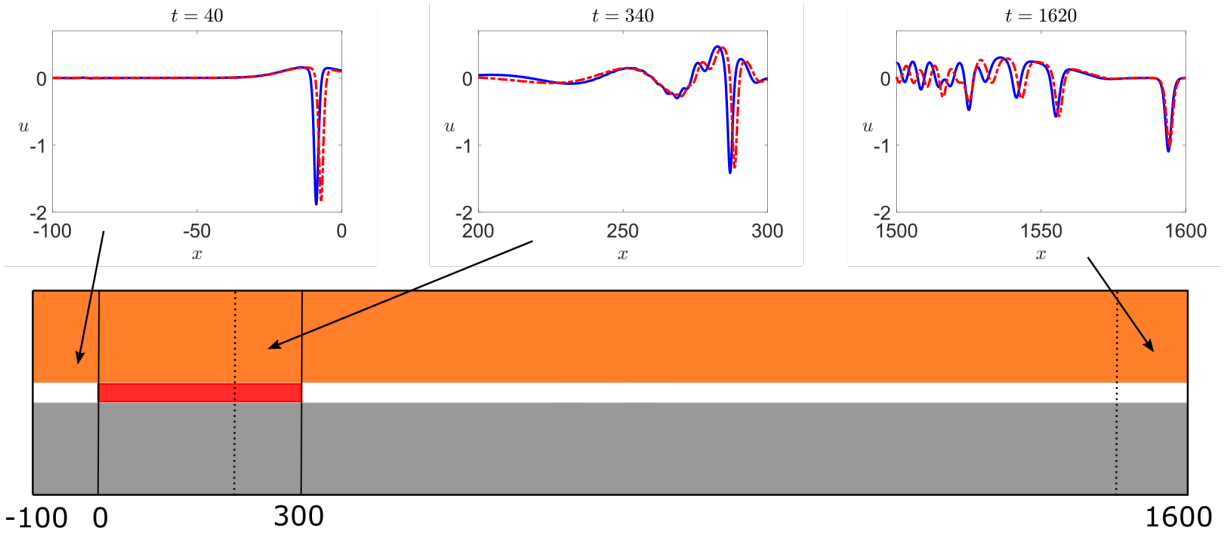

Figure 3.2: The waves in the upper waveguide with infinite delamination calculated using direct numerical simulations (blue, solid line) and the semi-analytical solution (red, dashed line). Parameters are $\varepsilon = 0.01$, $v = 4$, $v_1 = 1.04$ and $\gamma = 1$. For the finite difference method, the full computational domain is $[-100, 1600]$. In the pseudospectral method we have $N = 65,536$.

The theoretical prediction of the wave peaks' amplitudes, obtained using the IST as elaborated in Section 3.4.2, indicates the presence of three solitons. Specifically, the lead soliton's amplitude is predicted to be -1.016, agreeing with the semi-analytical results that the prediction is based upon. Meanwhile, the second and third solitons are predicted to have amplitudes of -0.392 and -0.042, respectively. In Figure 3.2, there appears to be a second soliton, exhibiting a larger amplitude than the prediction. However, it is yet to emerge entirely from the well, and as it does so, it is expected to lose some amplitude.

The next logical case to explore involves the scenario where the second delaminated region is not semi-infinite anymore, but rather sandwiched between two soft bonded regions as depicted in Figure 3.1b. Our objective is then to determine the presence of a delaminated region and, if confirmed, deduce its length based on the observed wave behaviour.

We now adjust the configuration from the infinite delamination case in Figure 3.2 by introducing an extra soft bonded region positioned at $1600 < x < 2400$. The resulting waves within this final soft bonded region are depicted in Figure 3.3. The plot shows that the leading solitary wave evolves into an Ostrovsky wave packet, upon propagating from the second delaminated region into the second soft bonded region, similar to the behaviour observed in the initial bonded region. There is also radiation trailing behind, which might mask any additional Ostrovsky wave packets originating from other solitons. Consequently, our analysis will primarily concentrate on the leading wave packet. It is worth noting that while the agreement is good around the leading wave packet, it diminishes further away from it due to the absence

of higher-order correction terms.

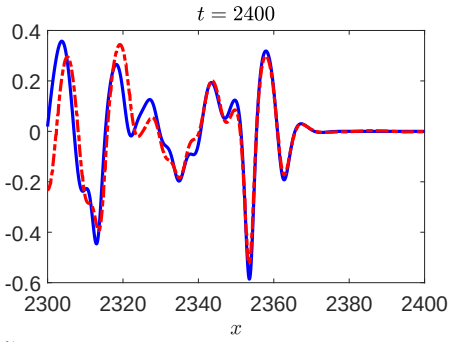

Figure 3.3: The solution in the final section of Figure 3.1(b), where $1600 < x < 2400$, using the same parameters stated in the caption for Figure 3.2 at $t = 2400$, for the direct numerical simulation (blue, solid line) and semi-analytical solution (red, dashed line).

3.4.4 Linear dispersion relations - KdV and Ostrovsky equations

To further understand the wave packet's behaviour, we will derive the linear dispersion relations for both the KdV and Ostrovsky equations. Previous studies, such as [26], have shown that the Ostrovsky wave packet travels at a velocity near the peak of the group speed, whereas solitary wave solutions of the KdV equation exist within the spectral gap, which is a range of frequencies where the solitary waves are stable and localised. Leveraging these insights can help us pinpoint the wave packet's location within the waveguide and assess if delamination has occurred. We proceed to derive the dispersion relations for a moving reference frame.

The linear dispersion relations are derived by seeking linear wave solutions of (3.20) and (3.24) (or equivalently, (3.28) and (3.32)). We look for solutions in the form $I \approx I_0 e^{i(k\xi - \omega X)}$ and $T^{(2)} \approx T_0 e^{i(k\xi - \omega X)}$, where ω represents the wave frequency and k denotes the wavenumber. Substituting these solutions into equations (3.20) and (3.24) and omitting nonlinear terms yields the dispersion relations

$$\omega(k) = -k^3 \ \text{ for } I \text{ and } \ \omega(k) = \frac{\gamma}{k} - k^3 \ \text{ for } T^{(2)}. \tag{3.51}$$

The same relationships can be derived from (3.28) and (3.32) accordingly. The phase speed is given by $p = \omega/k$, thus

$$p(k) = -k^2 \ \text{ for } I \text{ and } \ p(k) = \frac{\gamma}{k^2} - k^2 \ \text{ for } T^{(2)}.$$

The group speed is calculated as $c_g(k) = \mathrm{d}\omega/\mathrm{d}k$, hence

$$c_g(k) = -3k^2 \ \text{ for } I \text{ and } \ c_g(k) = -\frac{\gamma}{k^2} - 3k^2 \ \text{ for } T^{(2)}, \quad \text{with} \quad c_g(k) < 0. \tag{3.52}$$

A plot of the dispersion relation, phase speed and group speed for the parameters specified in the caption of Figure 3.2 is demonstrated in Figure 3.4.

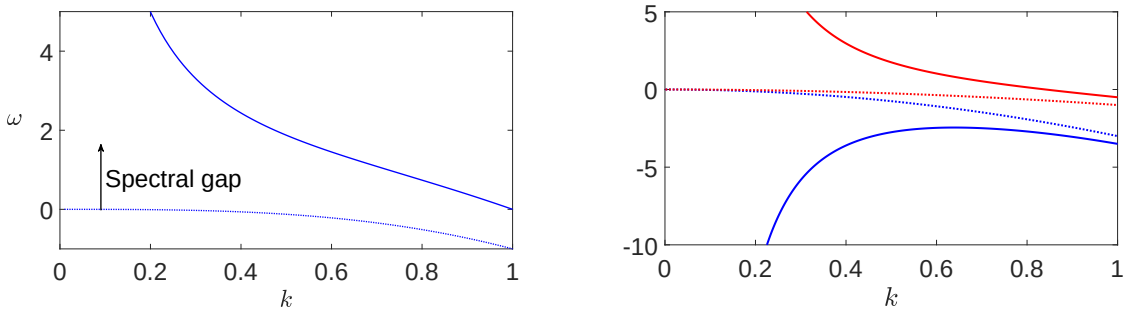

(a) Dispersion Relation

(b) Phase Speed and Group Velocity

Figure 3.4: The dispersion relation for the KdV/Ostrovsky equations is shown in Figure 3.4(a) and the phase speed (red) and group velocity (blue) are shown in Figure 3.4(b) for the base case parameters for soft bonded (solid) and delaminated (dotted) regions.

For $T^{(2)}$, in the soft bonded region, the group speed peak in Figure 3.4(b) is at $c_g = -2.449$ for $k_0 = 0.639$, thus the wave packet will propagate at this speed. However, in the case of delamination, the solitary wave solutions within the delaminated region exist within the spectral gap and travel at a speed $p > 0$, but close to $p = 0$.

Recalling the characteristic variables $\xi = x - ct$ and $X = \varepsilon x$, both with the dimension of length L, we can write c_g as

$$c_g = \frac{\mathrm{d}\xi}{\mathrm{d}X}, \tag{3.53}$$

where c_g represents a dimensionless speed in the characteristic reference frame. Consequently, for each unit increment in X, the wave packet therefore experiences a phase shift of magnitude $x_s = |c_g| = 2.449$ in the ξ direction, assuming the soliton has an amplitude close to zero. The value x_s serves as a dimensionless distance the wave packet travels in ξ for each unit increase in X.

Considering the dimensionless distance x_s, we use the expression for ξ to relate it to time as

$$c_g x_s - 0 = \frac{x_s}{\varepsilon} - t \Rightarrow t = \frac{x_s}{\varepsilon} - x_s c_g. \tag{3.54}$$

Translating back to (x, t) coordinates, we calculate x/t to obtain the phase speed v_b of the waves in the bonded region, predicted as

$$v_b = \frac{x}{t} = \frac{x_s/\varepsilon}{x_s/\varepsilon - x_s c_g} = \frac{1}{1 - \varepsilon x_s}. \tag{3.55}$$

Table 3.1 illustrates the wave speeds in each region of the waveguide from the semi-infinite delaminated structure, along with the predicted speed from the dispersion relation, v_b. It is observed that the solitary waves move at a speed greater than 1.02, while in the bonded region, the wave speed is slightly slower, showing a good agreement with the predicted speed from the dispersion relation.

v_b	v_1	v_2	v_3
0.976	1.033	1.010	1.021

Table 3.1: The predicted speed of the Ostrovsky wave packet in the bonded regions, v_b, and the numerically observed speed of the waves in each region, denoted v_1 to v_3.

3.4.5 Linear dispersion relation - Boussinesq-type equations

We now consider the dispersion relation for the system of Boussinesq and BKG equations (3.1)–(3.4). By substituting the sinusoidal approximation $u \approx e^{i(kx-\omega t)}$ into (3.1)–(3.4), we obtain the dispersion relation

$$\omega = \pm\sqrt{\frac{k^2+\varepsilon\gamma}{1+2\varepsilon\beta k^2}}, \tag{3.56}$$

where ω and k are defined as before. The phase speed is expressed as

$$p = \frac{\omega}{k} = \pm\sqrt{\frac{k^2+\varepsilon\gamma}{k^2+2\varepsilon\beta k^4}}. \tag{3.57}$$

Differentiating the dispersion relation with respect to k yields the group velocity as

$$c_g = \pm\frac{k(c^2-2\varepsilon^2\beta\gamma)}{\sqrt{\varepsilon\gamma+c^2k^2}(1+2\varepsilon\beta k^2)^{3/2}}. \tag{3.58}$$

In Figure 3.5 we provide the corresponding plot to Figure 3.4, but for (3.56) - (3.58). The peak of the group velocity in Figure 3.5(b) is $c_g = 0.976$, which is identical to the wave speed predicted by calculating the dispersion relation from the Ostrovsky equation, implying both methods will provide similar results.

3.4.6 Varying parameters

From the parameters specified in Section 3.4.3, and the β value specified in (3.1) - (3.4), we now vary the values of γ, β, and ε. The resulting wave speeds in each region are presented in Table 3.2.

Table 3.2 shows that the group speed increases when v and γ increase, whereas it decreases when β is increased. In all cases, there is good agreement between the predicted and observed wave speeds, except when varying v. This discrepancy arises because the BKG equations do not directly account for

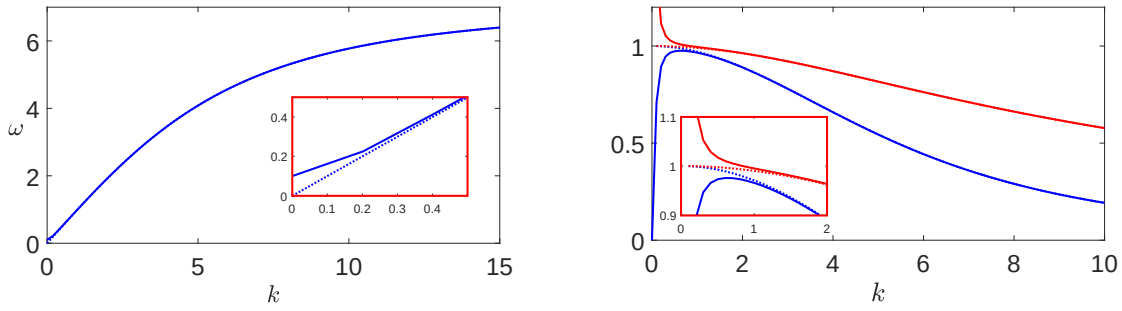

(a) Dispersion Relation

(b) Phase Speed and Group Velocity

Figure 3.5: The dispersion relation for Boussinesq-type equations is shown in Figure 3.5(a) and the phase speed (red) and group velocity (blue) are shown in Figure 3.5(b) for the base case parameters for soft bonded (solid) and delaminated (dotted) regions.

Initial condition	Zero mass				Non-zero mass			
Parameter	c_g	v_1	v_2	v_3	c_g	v_1	v_2	v_3
$v = 8$	0.976	1.163	1.000	1.047	0.976	1.191	1.003	0.995
$\beta = 8$	0.951	1.064	0.977	0.999	0.951	1.081	0.977	1.000
$\beta = 0.65$	0.986	1.064	0.993	1.026	0.986	1.081	0.993	1.025
$\gamma = 2$	0.966	1.064	0.965	1.018	0.966	1.081	0.965	1.018
$\gamma = 4$	0.952	1.064	0.955	0.982	0.952	1.087	0.955	1.011

Table 3.2: The predicted and numerically observed wave speeds for varying parameters and initial conditions.

amplitude, only indirectly through the scaling ε. The results also indicate little variation between using the zero-mass or non-zero-mass initial conditions.

The small wave parameter, ε, directly influences the degree of wave evolution. We will perform simulations using the setup shown in Figure 3.2, varying only ε while keeping all other parameters fixed. The resulting wave speeds in the soft bonded region from these simulations will be compared with theoretical predictions derived from the linear dispersion relations for both the Boussinesq and Ostrovsky equations, as presented in Table 3.3.

Table 3.3 shows excellent agreement between the numerically simulated wave speeds and the two theoretical predictions across all ε values, demonstrating that the linear dispersion relation accurately predicts wave speed for various ε values.

Similarly, we compare the amplitude of the leading wave peak at the end of the delaminated region from our numerical simulations - one set conducted over a duration of $t = 2000$ and another run for a sufficiently long time to allow the leading soliton to separate from the trailing radiation - with the theoretical predictions from the IST for various ε values, as shown in Table 3.4.

Parameter	c_g	v_b	v_2
$\varepsilon = 0.001$	0.9975	0.9976	1.0250
$\varepsilon = 0.002$	0.9951	0.9951	1.0000
$\varepsilon = 0.003$	0.9926	0.9927	1.0000
$\varepsilon = 0.004$	0.9902	0.9903	1.0125
$\varepsilon = 0.005$	0.9878	0.9879	1.0050
$\varepsilon = 0.006$	0.9853	0.9855	1.0042
$\varepsilon = 0.007$	0.9830	0.9831	1.0071
$\varepsilon = 0.008$	0.9810	0.9831	1.0031
$\varepsilon = 0.009$	0.9781	0.9783	1.0083
$\varepsilon = 0.010$	0.9757	0.9760	1.0100

Table 3.3: The numerically observed wave speed in the first soft bonded region, v_2, compared with the wave speed predicted from the linear dispersion relation for the Ostrovsky equation, v_b, and the Boussinesq equation, c_g, for $0.001 \leq \varepsilon \leq 0.01$

Parameter	**IST**	**Simulation** ($t = 2000$)	**Simulation (long run)**
$\varepsilon = 0.001$	-1.472	-1.502	-1.477
$\varepsilon = 0.002$	-1.107	-1.114	-1.107
$\varepsilon = 0.003$	-0.764	-0.763	-0.764
$\varepsilon = 0.004$	-0.630	-0.495	-0.629
$\varepsilon = 0.005$	-0.888	-0.930	-0.880
$\varepsilon = 0.006$	-1.098	-1.034	-1.098
$\varepsilon = 0.007$	-1.208	-1.209	-1.208
$\varepsilon = 0.008$	-1.220	-1.219	-1.221
$\varepsilon = 0.009$	-1.148	-1.148	-1.148
$\varepsilon = 0.010$	-1.016	-1.016	-1.016

Table 3.4: A comparison of the wave amplitude of the leading wave peak at the end of the second delaminated region in the numerical simulation at $t = 1600$ and the IST prediction for $0.001 \leq \varepsilon \leq 0.01$

Table 3.4 shows reasonable agreement between the amplitudes from numerical simulations at $t = 2000$ and the IST predictions for $\varepsilon \leq 0.006$. However, the agreement is not as precise, as the soliton's structure and amplitude are still influenced by the trailing radiation. In contrast, running the simulation long enough for the soliton to separate from the trailing radiation reveals excellent agreement with the IST predictions up to three decimal places. For $\varepsilon \geq 0.007$, both simulation cases demonstrate strong agreement of the amplitude with the IST prediction, as the faster evolution of the wave at larger ε values facilitates quicker separation of the soliton from the trailing radiation even at $t = 2000$. This further validates the IST as a reliable tool for predicting wave amplitudes in the delaminated region and supports the findings presented in Section 3.4.3.

3.4.7 Varying delamination length

To understand the impact of delamination in a layered structure, we investigate how varying the delamination length influences the wave behaviour in the second bonded region. We consider the finite

delaminated structure, using the same parameters as in Section 3.4.3. The delamination length of the second delaminated region is varied incrementally from $D = 0$ (indicating no delamination) in intervals of 10, up to $D = 360$. The calculation duration is set to a maximum of $t = 2000$.

We examine two scenarios: $\varepsilon = 0.005$ and $\varepsilon = 0.001$. Figure 3.6 illustrates the corresponding waves transmitted near the end of the first soft bonded region for these cases. Since the Ostrovsky equation has 'time' represented as $X = \varepsilon x$, we anticipate that a lower value of ε will result in less evolution. Hence, for $\varepsilon = 0.001$, the wave resembles a soliton more closely, while for $\varepsilon = 0.005$, it manifests as an Ostrovsky wave packet. This distinction provides two distinct behaviours for analysis. Other values of ε are expected to align with either of these behaviours or fall within the transition between them. However, as we have already analysed $\varepsilon = 0.001$ and $\varepsilon = 0.005$, examining intermediate cases would add little value and is therefore not pursued within this thesis.

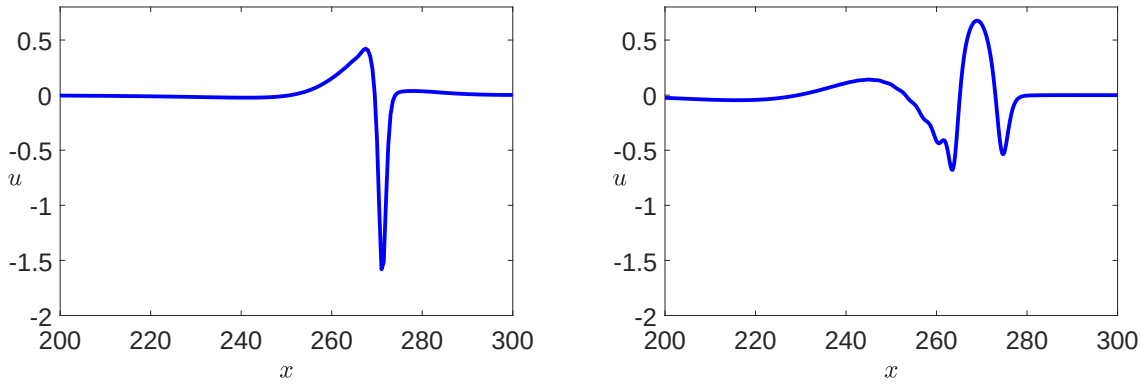

(a) $\varepsilon = 0.001$ (b) $\varepsilon = 0.005$

Figure 3.6: Waves located near the end of the first soft bonded region of the upper waveguide for (a) $\varepsilon = 0.001$ and (b) $\varepsilon = 0.005$.

The amplitude of the Ostrovsky wave packet fluctuates during its propagation, with a peak amplitude near its centre [26]. We determine this peak amplitude by identifying the maximum value in the second bonded region, spanning from $t = 1600$ to $t = 2000$. We then investigate how this peak amplitude varies with different delamination lengths compared to the no-delamination case. The results are shown in Figure 3.7.

In the case where $\varepsilon = 0.001$, there appears to be an almost linear correlation between the delamination length and the amplitude change. This finding is consistent with observations in the solitary wave and radiating solitary wave cases [48, 77]. Conversely, for $\varepsilon = 0.005$, we initially observe an increase in amplitude. However, as the delamination length continues to increase, the amplitude of the wave packet decreases in a nonlinear manner. This is expected as the wave packet comprises of at least one peak

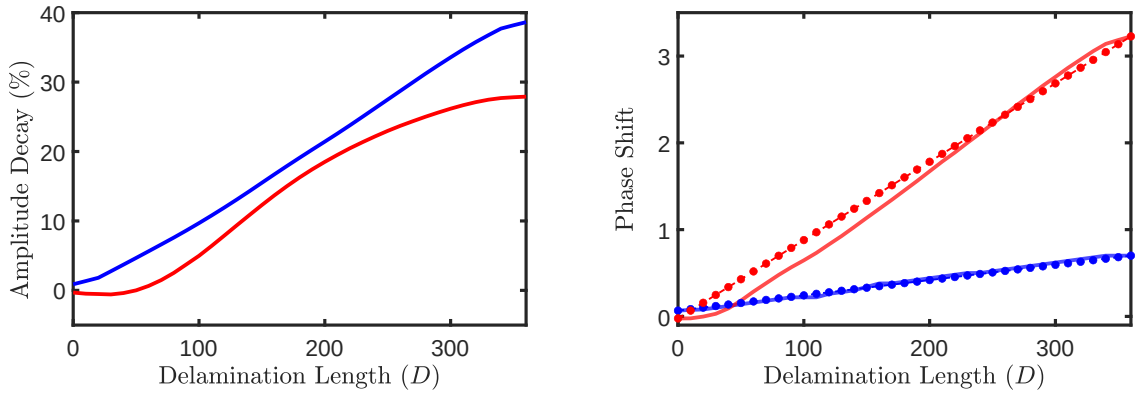

(a) Change in Amplitude

(b) Phase Shift

Figure 3.7: Plots showing (a) the percentage change in amplitude and (b) the phase shift curves (solid lines) relative to the fully bonded case, with their gradients (dashed lines with circular markers). Blue and red lines correspond to $\varepsilon = 0.001$ and $\varepsilon = 0.005$, respectively.

that will eventually evolve into solitons within the delaminated region. However, initially, these peaks are contained within a wave packet, leading to an artificial boost in their amplitude due to the accompanying radiation. As the delamination size increases, the generated solitons gradually separate from the wave packet, becoming distinct. This separation could lead to the expected drop in amplitude as the solitons evolve into Ostrovsky wave packets within the second bonded region.

We now consider the phase shift at the front of the wave packet by manually tracking its position for varying delamination lengths, relative to the no-delamination case. For $\varepsilon = 0.001$, initially, as the delamination length ranges from 0 to 10, there is a sharp rise in phase shift, gradually tapering off beyond $D = 10$. Similarly, for $\varepsilon = 0.005$, there is a noticeable phase shift increase with delamination length. While the relationship is nonlinear, it tends to become closer to linear after an initial adjustment period. We also plotted the gradient of these phase shift curves, which showed a linear increase as the delamination length increased for both ε. For $\varepsilon = 0.005$, the phase increased more significantly than for $\varepsilon = 0.001$.

Referring to Section 3.4.4, we expect a minimum phase shift of $x_s = 2.449$ for $\varepsilon = 0.005$ when $D = 200$, as per the linear dispersion relation. The phase shift from $D = 200$ to $D = 300$ is 1.09. This leads to noticeable disagreement in the gradient at the centre of the phase shift line in Figure 3.7(b), albeit expected due to the nonlinear behaviour contributing to some deviation in the results. Similarly, for $\varepsilon = 0.001$, we predict a minimum phase shift of $x_s = 2.449$ for $D = 1000$. The gradient line of the phase shift for $\varepsilon = 0.001$ closely matches this minimum phase shift.

3.4.8 Application to model a PMMA bar

Let us recall from Section 2.1.1 the DDE

$$u_{tt} - c^2 u_{xx} = \frac{\beta}{\rho} u_x u_{xx} + \frac{J\nu^2}{\sigma}(u_{tt} - c_1^2 u_{xx})_{xx}. \tag{3.59}$$

We adapt this model by including a bonding coefficient γ_m, simulating the waveguide being attached to a much denser lower waveguide via a soft bond, thus

$$u_{tt} - c^2 u_{xx} = \frac{\beta}{\rho} u_x u_{xx} + \frac{J\nu^2}{\sigma}\left(u_{tt} - c_1^2 u_{xx}\right)_{xx} - \gamma_m u. \tag{3.60}$$

We can apply a scaling to bring us to the non-dimensional form, namely

$$\tilde{x} = \frac{x}{X}, \quad \tilde{U} = \frac{u}{U}, \quad \tilde{t} = \frac{t}{T}, \tag{3.61}$$

where

$$X = \sqrt{\frac{J\nu^2}{2\varepsilon\sigma c^2}\left(c^2 - c_1^2\right)}, \quad T = \frac{X}{c}, \quad U = -\frac{12\varepsilon c^2 \rho}{\beta} X, \quad \gamma_m = \frac{2\varepsilon^2 \sigma \gamma}{J\nu^2\left(c^2 - c_1^2\right)}. \tag{3.62}$$

In doing so, we obtain equation (3.2) and an estimate for the 'material' bonding coefficient, γ_m, in terms of the non-dimensional one, γ, used in our results. Within the delaminated regions of the bar, we set $\gamma = 0$, hence $\gamma_m = 0$. Considering a PMMA bar with a cross-section of 10 mm $\times$ 10 mm, which corresponds to dimensions of $2a$ mm $\times$ $2b$ mm, (consistent with experimental setups), we adopt material parameters derived from experiments on PMMA [100], as presented in Table 3.5.

a (m)	b (m)	ρ (kg/m^3)	ν	E (GPa)	l (GPa)	m (GPa)	n (GPa)	β (GPa)
5×10^{-3}	5×10^{-3}	1.16×10^{-3}	0.34	5.27	-10.90	-7.70	-1.4	-3.57

Table 3.5: Table of experimental parameters with definitions consistent with those described in Section 2.1.1, where a and b are the dimensions of the bar's cross-section, ρ is the material density, ν is Poisson's ratio, E is Young's modulus, l, n, and m are Murnaghan's moduli, and β is a nonlinear coefficient.

With these parameters, we can perform a simulation using our model. We take $\varepsilon = 0.1$, consistent with the value utilised in [46] for numerical simulations. The bar is configured with a length of 600 mm, with a delamination beginning at 300 mm.

Based on the results illustrated in Figure 3.8, it becomes apparent that an Ostrovsky wave packet forms within the bonded region, while solitons emerge within the delaminated region. However, these solitons are not fully developed and would require a longer bar for complete separation. The simulated

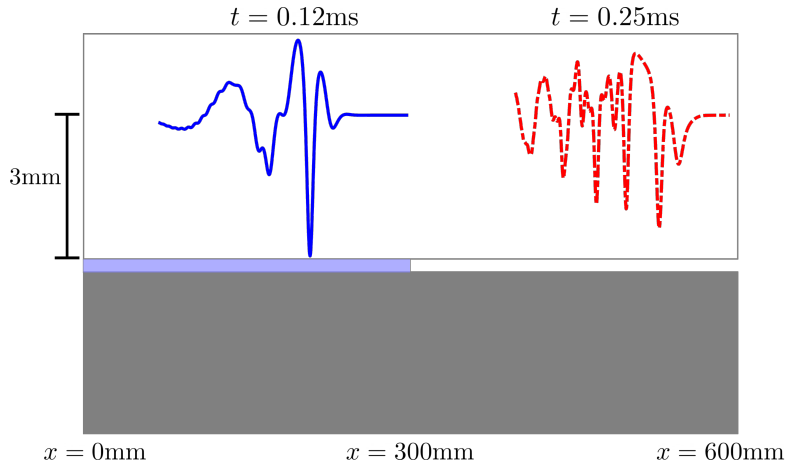

Figure 3.8: Ostrovsky wave packet generation and scattering in a bi-layer structure employing material parameters corresponding to PMMA. Here, we adopt $\varepsilon = 0.1$, with all measurements converted back to dimensional variables.

wave height is approximately 3 mm high, and takes 0.25 ms to approach the end of the bar (0.29 ms to reach it).

3.5 Summary

In this chapter, we explored the scattering of an Ostrovsky wave packet within the upper waveguide of a bi-layer structure featuring both soft bonding and delamination between the layers. Our investigation focused on a configuration where the lower layer has a significantly higher density compared to the upper layer. This setup is described by the BKG equations in the bonded regions and the Boussinesq equations in the delaminated regions.

We constructed weakly-nonlinear solutions with matched asymptotic multiple-scale expansions and used averaging techniques with respect to the fast space variable to derive leading order solutions. This methodology follows established works in the field, which have explored various material properties and bonding conditions [47, 48].

We ran and compared simulations using a direct numerical scheme with a semi-analytical approach, observing good agreement throughout the waveguide. For enhanced accuracy, higher-order corrections in the weakly-nonlinear solution can be derived, similar to the approach used for initial-value problems for these equations [72, 94, 96].

In the initial delaminated region, a solitary wave was generated. Unlike prior studies where the wave evolved into solitons or radiating solitary waves in the soft bonded region, we observed Ostrovsky wave packets in the soft bonded region due to the significant difference in wave speeds between the layers [23].

As the Ostrovsky wave packet entered the second delaminated region, it evolved into a series of rank-ordered solitons accompanied by dispersive radiation, consistent with theoretical predictions from IST theory for the KdV equation [12]. We found excellent agreement between the amplitude of the leading soliton in the simulation and the theoretical prediction using the IST, even across various ε values. Upon re-entering the second bonded region, each of these solitons transitioned into Ostrovsky wave packets, with the leading soliton displaying the most distinct behaviour.

As the length of the delaminated region increases, we observed a decrease in the amplitude of the largest wave peak within the Ostrovsky wave packet. This decrease follows a predominantly linear trend for small values of the wave parameter ε, while for larger values of ε, it exhibits nonlinear behaviour, starting with an initial growth phase followed by decay. Similarly, we noticed an increasing phase shift relative to the fully bonded case as the delamination length increased. This phase shift demonstrates a linear relationship for small ε values and a nonlinear trend for larger ε values. The linear dispersion relation methods for the KdV and Ostrovsky equations, as well as for the BKG and Boussinesq equations, were used to successfully predict the wave speeds in each section for various ε values, showing good agreement with the observed numerical results.

Experiments conducted on PMMA and polystyrene layered waveguides [46,68] have previously demonstrated that solitons can be detected at larger distances compared to linear waves [101]. Motivated by these findings, we simulated a PMMA bar with a cross-section of 10mm $\times$ 10mm and a length of 600mm. Our simulations revealed the development of Ostrovsky wave packets in bonded regions, with solitons beginning to form in delaminated regions. These numerical findings could be used for laboratory experiments involving a diverse range of materials to detect certain waves as a means of controlling delamination.

In Chapter 4, we will explore a similar scattering problem where the lower layer is not as dense, thus we consider its longitudinal displacement, and so coupled Boussinesq equations are employed instead. This will involve a more detailed examination of the weakly-nonlinear solution. Unlike [48], the wave speed in the lower layer will exceed $c = 1 + \mathcal{O}(\varepsilon)$. This suggests that while there might be some initial interaction between the waves in each waveguide, the faster wave in the lower layer will eventually break away from the wave in the upper layer, leading to minimal long-term interaction. Consequently, we do not anticipate observing the radiating solitary waves seen in [48].

Chapter 4

Scattering of an Ostrovsky wave packet in a two-layered waveguide

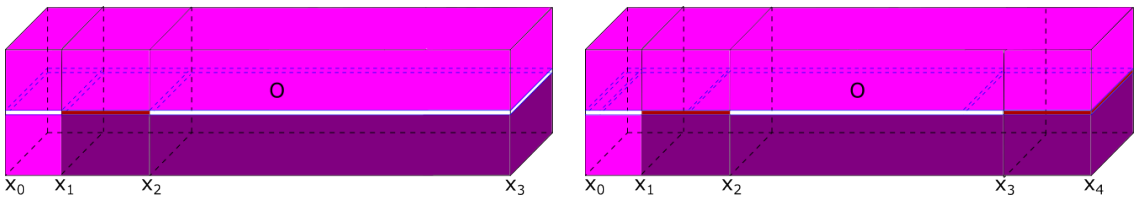

(a) Infinite delamination case

(b) Finite delamination case

Figure 4.1: Schematic of the bi-layer structures with a homogeneous region for $x_0 < x < x_1$, a soft bonded region for $x_1 < x < x_2$ and a delaminated region for $x_2 < x < x_3$. Figure 4.1(b) shows another soft bonded region for $x_3 < x < x_4$. We assume that the homogeneous section has the same material properties as the upper layer and, for the other three sections, we assume that the material in both layers has similar material properties.

In this chapter, we investigate wave scattering in the structures shown in Figure 4.1. These structures are similar those in Chapter 3, but instead of a delaminated first region, the first region here is homogeneous with uniform waveguide densities. Additionally, while Chapter 3 focused only on the upper layer, this chapter examines both layers, as the density discrepancy between them is smaller, except in the first region.

This chapter is organised as follows: in Section 4.1, we will introduce the set of coupled Boussinesq equations that govern the longitudinal displacement and strain within each section of the waveguide. In Section 4.2, we will construct weakly-nonlinear solutions to describe the wave propagation, using an asymptotic multiple-scales expansion at leading order. The constructed leading order solutions will then be used in the semi-analytical method, as in Chapter 3.

In Section 4.3, we will compare the direct numerical solution to the constructed semi-analytical solution, with the aim of achieving good agreement and demonstrating a substantial improvement in computation speed with the semi-analytical approach. Two scenarios will be examined: one with a soft bonded region followed by infinite delamination, and another where delamination is situated between soft bonded regions. The characteristic speed in the lower layer will be varied and compared to theoretical predictions from the linear dispersion relation. We then plot the phase shift, defined as the difference in position of the leading peaks relative to a fully bonded case, for cases of various delamination lengths and positions. When given only a phase shift value, we will use our plots from both layers, or when waves transmit in both directions through the upper layer, to uniquely determine the position and length of the delamination. We will conclude our findings in Section 4.4. The results of this chapter are partially summarised in [102].

4.1 Problem formulation

Similar to Chapter 3, in this chapter we will examine the scattering of a wave packet within a two-layered structure with semi-infinite delamination. The structure consists of an initial homogeneous section, followed by a soft bonded region and then a delaminated region, as illustrated in Figure 4.1(a). Figure 4.1(b) depicts a finite delamination case, similar to the semi-infinite scenario but with the delaminated section 'sandwiched' between two bonded sections. These structures are inspired by the experimental setup in [46].

In Chapter 3, we considered a limiting case where the material in the lower layer differed significantly from that in the upper layer, allowing us to treat the displacements in the lower layer as negligible. In this chapter, we examine the scenario where the characteristic speed in the lower layer is denoted c, while in the upper layer we assume unit speed and the difference in speed between the layers satisfying the relationship $c - 1 = \mathcal{O}(1)$. This assumption reflects the significantly different material properties in each layer, allowing us to consider wave scattering in both layers. In [48], the scattering of long longitudinal waves in this structure was also examined, but the characteristic speeds in the layers differed by $\mathcal{O}(\varepsilon)$, where ε represents a small wave parameter, with the order symbol here indicating the power of ε. The leading order equations were instead described by coupled Ostrovsky equations in the bonded sections and uncoupled Korteweg-de Vries (KdV) equations in the delaminated sections of the bar, consistent with the time-averaged derivation for the initial-value problem, as studied in [72].

Following the notation used in Chapter 3 and [48], we denote the longitudinal displacements in the upper layer of the i-th section as $u^{(i)}$ and in the lower layer as $w^{(i)}$. For both the homogeneous and

delaminated regions, α and β represent the physical and geometrical properties of the waveguide, while c is the wave speed. In the homogeneous region, these constants are set to 1, while in the delaminated region, where these constants may differ. The system governing longitudinal displacements is described by an uncoupled pair of Boussinesq equations

$$\begin{aligned} u_{tt}^{(i)} - u_{xx}^{(i)} &= 2\varepsilon \left[-6u_x^{(i)} u_{xx}^{(i)} + u_{ttxx}^{(i)} \right], \\ w_{tt}^{(i)} - c^2 w_{xx}^{(i)} &= 2\varepsilon \left[-6\alpha w_x^{(i)} w_{xx}^{(i)} + \beta w_{ttxx}^{(i)} \right], \end{aligned} \tag{4.1}$$

for $i = 1, 3$, where $i = 1$ denotes the homogeneous region in which the waveguides have identical material properties, and $i = 3$ denotes the delaminated region. δ and γ are coupling coefficients which depend on the properties of the soft bonded layer [29, 48]. Note that in Chapter 3, we considered the limiting case where in the lower layer $c \to \infty$ and consequently $w \to 0$. For the soft bonded regions, where $i = 2, 4$, the coupled regularised Boussinesq (cRB) equations describe the longitudinal displacement of the waves within the waveguides:

$$\begin{aligned} u_{tt}^{(i)} - u_{xx}^{(i)} &= 2\varepsilon \left[-6u_x^{(i)} u_{xx}^{(i)} + u_{ttxx}^{(i)} - \delta \left(f^{(i)} - g^{(i)} \right) \right], \\ w_{tt}^{(i)} - c^2 w_{xx}^{(i)} &= 2\varepsilon \left[-6\alpha w_x^{(i)} w_{xx}^{(i)} + \beta w_{ttxx}^{(i)} + \gamma \left(f^{(i)} - g^{(i)} \right) \right]. \end{aligned} \tag{4.2}$$

The equations are scaled so that α, β and c appear exclusively in the lower layer. Now, we describe the longitudinal strain of the waves by denoting $f^{(i)} = u_x^{(i)}$ and $g^{(i)} = w_x^{(i)}$, so the system in homogeneous and delaminated regions is formulated as

$$\begin{aligned} f_{tt}^{(i)} - f_{xx}^{(i)} &= 2\varepsilon \left[-3 \left(f^{(i)} \right)_{xx}^2 + f_{ttxx}^{(i)} \right], \\ g_{tt}^{(i)} - c^2 g_{xx}^{(i)} &= 2\varepsilon \left[-3\alpha \left(g^{(i)} \right)_{xx}^2 + \beta g_{ttxx}^{(i)} \right], \end{aligned} \tag{4.3}$$

for $i = 1, 3$. For the soft bonded regions, we have

$$\begin{aligned} f_{tt}^{(i)} - f_{xx}^{(i)} &= 2\varepsilon \left[-3 \left(f^{(i)} \right)_{xx}^2 + f_{ttxx}^{(i)} - \delta \left(f^{(i)} - g^{(i)} \right) \right], \\ g_{tt}^{(i)} - c^2 g_{xx}^{(i)} &= 2\varepsilon \left[-3\alpha \left(g^{(i)} \right)_{xx}^2 + \beta g_{ttxx}^{(i)} + \gamma \left(f^{(i)} - g^{(i)} \right) \right], \end{aligned} \tag{4.4}$$

for $i = 2, 4$. These equations are complemented by continuity conditions at the interfaces between the

sections, with the continuity of longitudinal displacement denoted as

$$u^{(i)}|_{x=x_i} = u^{(i+1)}|_{x=x_i}, \quad w^{(i)}|_{x=x_i} = w^{(i+1)}|_{x=x_i}, \quad i = 1, 2, 3 \tag{4.5}$$

The continuity of normal stress at the interface in the upper bar is written as

$$f^{(i)} + 2\varepsilon \left[-3 \left(f^{(i)} \right)^2 + f^{(i)}_{tt} \right] \Big|_{x=x_i} = f^{(i)} + 2\varepsilon \left[-3 \left(f^{(i+1)} \right)^2 + f^{(i+1)}_{tt} \right] \Big|_{x=x_i}, \quad i = 1, 2, 3, \tag{4.6}$$

and for the lower layer we have

$$g^{(1)} + 2\varepsilon \left[-3 \left(g^{(1)} \right)^2 + g^{(1)}_{tt} \right] \Big|_{x=x_1} = c^2 g^{(2)} + 2\varepsilon \left[-3\alpha \left(g^{(2)} \right)^2 + \beta g^{(2)}_{tt} \right] \Big|_{x=x_1}, \tag{4.7}$$

$$c^2 g^{(i)} + 2\varepsilon \left[-3\alpha \left(g^{(i)} \right)^2 + \beta g^{(i)}_{tt} \right] \Big|_{x=x_i} = c^2 g^{(i+1)} + 2\varepsilon \left[-3\alpha \left(g^{(i+1)} \right)^2 + \beta g^{(i+1)}_{tt} \right] \Big|_{x=x_i}, \quad i = 2, 3. \tag{4.8}$$

With the governing equations and corresponding continuity conditions for our structures now established, we will proceed by constructing weakly-nonlinear solutions and deriving leading order approximations along with the necessary initial conditions.

4.2 Weakly-nonlinear solution

We construct a weakly-nonlinear solution up to $\mathcal{O}(\varepsilon)$ using a methodology similar to that in Chapter 3 to derive the leading order solutions. While some steps are abbreviated here due to their resemblance to those in Chapter 3, the key processes and results are still provided.

4.2.1 Homogeneous section

Let us consider the first region of the bar, the homogeneous section as shown in Figure 4.1(a), using the notation from Section 4.1, we construct the leading order weakly-nonlinear solution for the upper layer in this region, which takes the form

$$f^{(1)}(x,t) = I^{(1)}(\xi, X) + R^{(1)}(\eta, X) + \varepsilon P^{(1)}(\xi, \eta, X) + \mathcal{O}(\varepsilon^2), \tag{4.9}$$

where $\xi = x - t$ and $\eta = x + t$ represent the fast characteristic variables, while $X = \varepsilon x$ denotes the slow space variable. The function $I^{(1)}$ corresponds to the incident wave, $R^{(1)}$ represents the reflected waves, and $P^{(1)}$ accounts for the higher-order correction at $\mathcal{O}(\varepsilon)$. Substituting this expansion into system (4.3)

gives

$$-4P^{(1)}_{\xi\eta} = \left(2I^{(1)}_X - 12I^{(1)}I^{(1)}_\xi + 2I^{(1)}_{\xi\xi\xi}\right)_\xi + \left(2R^{(1)}_X - 12R^{(1)}R^{(1)}_\eta + 2R^{(1)}_{\eta\eta\eta}\right)_\eta + 12\left(I^{(1)}_{\xi\xi}R^{(1)} + I^{(1)}R^{(1)}_{\eta\eta} + 2I^{(1)}_\xi R^{(1)}_\eta\right). \tag{4.10}$$

Averaging the left-hand side of (4.10) by integrating with respect to x, similar to the approach in (3.14), while keeping the constant η fixed, yields

$$\begin{aligned}\lim_{x_0\to-\infty}\frac{-4}{x_1-x_0}\int_{x_0}^{x_1}P^{(1)}_{\xi\eta}\mathrm{d}\eta &= \lim_{x_0\to-\infty}\frac{-4}{2(x_1-x_0)}\int_{2x_0-\eta}^{2x_1-\eta}P^{(1)}_{\xi\eta}\mathrm{d}\eta\\ &= \lim_{x_0\to-\infty}\frac{-4}{2(x_1-x_0)}\left[P^{(1)}_\xi\right]_{2x_0-\eta}^{2x_1-\eta}\\ &= 0.\end{aligned} \tag{4.11}$$

Similarly averaging the right-hand side of (4.10) yields

$$\begin{aligned}0 = &\lim_{x_0\to-\infty}\frac{1}{2(x_1-x_0)}\left[2I^{(1)}_X - 12I^{(1)}I^{(1)}_\xi + 2I^{(1)}_{\xi\xi\xi}\right]_{2x_0-\xi}^{2x_1-\xi}\\ &+ (2R^{(1)}_X - 12R^{(1)}R^{(1)}_\eta + 2R^{(1)}_{\eta\eta\eta})_\eta\lim_{x_0\to-\infty}\left[\frac{\eta}{2(x_1-x_0)}\right]_{2x_0-\xi}^{2x_1-\xi}\\ &- \lim_{x_0\to-\infty}\frac{1}{2(x_1-x_0)}\int_{2x_0-\xi}^{2x_1-\xi}(I^{(1)}_{\xi\xi}R^{(1)} + I^{(1)}R^{(1)}_{\eta\eta} + 2I^{(1)}_\xi R^{(1)}_\eta)\ \mathrm{d}\eta.\end{aligned} \tag{4.12}$$

Evaluating the first and third lines of (4.12) gives us 0, leading to the KdV equation

$$R^{(1)}_X - 6R^{(1)}R^{(1)}_\eta + R^{(1)}_{\eta\eta\eta} = 0. \tag{4.13}$$

Similarly, by averaging with respect to ξ we find

$$I^{(1)}_X - 6I^{(1)}I^{(1)}_\xi + I^{(1)}_{\xi\xi\xi} = 0. \tag{4.14}$$

Thus, by substituting the KdV equations into (4.10) and integrating with respect to ξ and η, we find the higher-order correction

$$P^{(1)} = 3\left(2I^{(1)}R^{(1)} + R^{(1)}_\eta\int I^{(1)}\mathrm{d}\xi + I^{(1)}_\xi\int R^{(1)}\mathrm{d}\eta\right) + \phi^{(1)}_1(\xi, X) + \psi^{(1)}_1(\eta, X), \tag{4.15}$$

where $\phi_1^{(1)}$, $\psi_1^{(1)}$ are arbitrary functions. For the lower layer, we construct the weakly-nonlinear solution, of the form

$$g^{(1)}(x,t) = I^{(1)}(\xi, X) + G^{(1)}(\eta, X) + \varepsilon Q^{(1)}(\xi, \eta, X) + \mathcal{O}(\varepsilon^2), \tag{4.16}$$

where $I^{(1)}$ is the same as in the upper layer. The reflected waves are denoted by $G^{(1)}(\eta, X)$, and $Q^{(1)}(\xi, \eta, X)$ represents the higher-order correction. Since the incident wave is identical to the upper layer, one of the leading order equations for the lower layer is (4.14). Using a similar process as for the upper layer, the other leading order equation is

$$G_X^{(1)} - 6G^{(1)}G_\eta^{(1)} + G_{\eta\eta\eta}^{(1)} = 0, \tag{4.17}$$

and the higher-order correction is

$$Q^{(1)} = 3\left(2I^{(1)}G^{(1)} + G_\eta^{(1)}\int I^{(1)}\mathrm{d}\xi + I_\xi^{(1)}\int G^{(1)}\mathrm{d}\eta\right) + \phi_2^{(1)}(\xi, X) + \psi_2^{(1)}(\eta, X), \tag{4.18}$$

where $\phi_2^{(1)}$, $\psi_2^{(1)}$ are arbitrary functions.

4.2.2 Soft bonded sections

Now, we consider the case where the layers are soft bonded, with significantly different material properties, resulting in a characteristic speed difference between the layers of $c-1 = \mathcal{O}(1)$. For the second soft bonded region, we do not account for reflected waves, as it is the final section of the structure.

We will construct the weakly-nonlinear solutions to (4.4) in the following form

$$\begin{aligned} f^{(i)}(x,t) &= T^{(i)}(\xi, X) + R^{(i)}(\eta, X) + \varepsilon P^{(i)}(\xi, \eta, X) + \mathcal{O}(\varepsilon^2), \\ g^{(i)}(x,t) &= S^{(i)}(\nu, X) + G^{(i)}(\zeta, X) + \varepsilon Q^{(i)}(\nu, \zeta, X) + \mathcal{O}(\varepsilon^2), \end{aligned} \tag{4.19}$$

where $i = 2$ corresponds to the first soft bonded region and $i = 4$ to the second. Here, $f^{(i)}$ represents the solution for the upper layer, and $g^{(i)}$ represents the solution for the lower layer. The characteristic variables ξ, η and X are the same as before, but we now have different characteristic variables for the

second layer, $\nu = x - ct$ and $\zeta = x + ct$. Substituting the expansion of $f^{(i)}$ into (4.4) gives

$$\begin{aligned} -4P^{(i)}_{\xi\eta} = &\left(2T^{(i)}_X - 12(T^{(i)}T^{(i)}_\xi) + 2T^{(i)}_{\xi\xi\xi}\right)_\xi - 2\delta\left(T^{(i)} - S^{(i)}\right) \\ &+ \left(2R^{(i)}_X - 12(R^{(i)}R^{(i)}_\eta) + 2R^{(i)}_{\eta\eta\eta}\right)_\eta - 2\delta\left(R^{(i)} - G^{(i)}\right) \\ &- 12\left(T^{(i)}_{\xi\xi}R^{(i)} + T^{(i)}R^{(i)}_{\eta\eta} + 2T^{(i)}_\xi R^{(i)}_\eta\right). \end{aligned} \tag{4.20}$$

Space averaging the left-hand side of (4.20) while keeping the constant ξ fixed yields 0, similar to the homogeneous region, while averaging the right-hand side gives

$$\begin{aligned} &\left(2R^{(i)}_{\eta X} - 12(R^{(i)}R^{(i)}_\eta)_\eta + 2R^{(i)}_{\eta\eta\eta\eta} - \delta R^{(i)}\right) \lim_{x_{i-1}\to-\infty} \frac{1}{2(x_i - x_{i-1})} \int_{2x_{i-1}-\eta}^{2x_i-\eta} \mathrm{d}\xi \\ &+ \lim_{x_{i-1}\to-\infty} \frac{1}{2(x_i - x_{i-1})} \int_{2x_{i-1}-\eta}^{2x_i-\eta} \delta G^{(i)} \mathrm{d}\xi = 0. \end{aligned} \tag{4.21}$$

Recalling that ζ is a variable in $G^{(i)}$, we express ζ as

$$\frac{(1-c)\xi + (1+c)\eta}{2} = \zeta. \tag{4.22}$$

By transforming the variable ζ in the function $G^{(i)}$ to the expression on the left-hand side of (4.22), we can integrate with respect to ξ to obtain the leading order Ostrovsky equation

$$\left(R^{(i)}_X - 6R^{(i)}R^{(i)}_\eta + R^{(i)}_{\eta\eta\eta}\right)_\eta = \delta R^{(i)}. \tag{4.23}$$

We now apply averaging while holding η constant, following a similar process as when ξ was held constant. Averaging the left-hand side of (4.20) again results in zero. For the right-hand side, we transform ν as

$$\frac{(1+c)\xi + (1-c)\eta}{2} = \nu, \tag{4.24}$$

and perform the averaging to obtain the following leading order Ostrovsky term

$$\left(T^{(i)}_X - 6T^{(i)}T^{(i)}_\xi + T^{(i)}_{\xi\xi\xi}\right)_\xi = \delta T^{(i)}. \tag{4.25}$$

By substituting our leading order Ostrovsky equations into (4.20) and integrating with respect to ξ and

η, we obtain the higher-order correction $P^{(i)}$ as

$$P^{(i)} = -\frac{\delta}{1-c^2}\left(\int\int G^{(i)}(\nu,X)\mathrm{d}\nu\mathrm{d}\nu + \int\int S^{(i)}(\zeta,X)\mathrm{d}\zeta\mathrm{d}\zeta\right) + 3\left(2T^{(i)}R^{(i)} + R^{(i)}_{\eta}\int T^{(i)}\mathrm{d}\xi + T^{(i)}_{\xi}\int R^{(i)}\mathrm{d}\eta\right) + \phi^{(i)}_1(\xi,X) + \psi^{(i)}_1(\eta,X), \tag{4.26}$$

where $\phi^{(i)}_1$, $\psi^{(i)}_1$ are arbitrary functions. Following a similar averaging process for the lower layer, we obtain

$$\left(c^2 S^{(i)}_X - 6\alpha S^{(i)}S^{(i)}_{\nu} + \beta c^2 S^{(i)}_{\nu\nu\nu}\right)_{\nu} = \gamma S^{(i)}, \tag{4.27}$$

$$\left(c^2 G^{(i)}_X - 6\alpha G^{(i)}G^{(i)}_{\zeta} + \beta c^2 G^{(i)}_{\zeta\zeta\zeta}\right)_{\zeta} = \gamma G^{(i)}. \tag{4.28}$$

Following a similar process for the lower layer as for the upper layer, we obtain the higher-order correction $Q^{(i)}$ as follows:

$$Q^{(i)} = \frac{\gamma}{1-c^2}\left(\int\int T^{(i)}\mathrm{d}\xi\mathrm{d}\xi + \int\int R^{(i)}\mathrm{d}\eta\mathrm{d}\eta\right) + 3\alpha\left(2S^{(i)}G^{(i)} + G^{(i)}_{\zeta}\int S^{(i)}\mathrm{d}\nu + S^{(i)}_{\nu}\int G^{(i)}\mathrm{d}\zeta\right) + \phi^{(i)}_2(\nu,X) + \psi^{(i)}_2(\zeta,X), \tag{4.29}$$

where $\phi^{(i)}_2$, $\psi^{(i)}_2$ are arbitrary functions. Recalling that the second soft bonded region is the final region of the structure, no reflective waves are generated, resulting in $R^{(4)} = 0$ and $G^{(4)} = 0$. Consequently, $\psi^{(4)}_1 = 0$ and $\psi^{(4)}_2 = 0$.

4.2.3 Delaminated section

We now consider the third region of the structure where delamination is present. We construct the weakly-nonlinear solution in the form

$$\begin{aligned} f^{(3)}(x,t) &= T^{(3)}(\xi,X) + R^{(3)}(\eta,X) + \varepsilon P^{(3)}(\xi,\eta,X) + \mathcal{O}(\varepsilon^2), \\ g^{(3)}(x,t) &= S^{(3)}(\nu,X) + G^{(3)}(\zeta,X) + \varepsilon Q^{(3)}(\nu,\zeta,X) + \mathcal{O}(\varepsilon^2), \end{aligned} \tag{4.30}$$

where the two sets of characteristic variables are the same as the soft bonded regions. Substituting the expansion of $f^{(3)}$ into (4.3) gives

$$-4P^{(3)}_{\xi\eta} = \left(2T^{(3)}_X - 12(T^{(3)}T^{(3)}_\xi) + 2T^{(3)}_{\xi\xi\xi}\right)_\xi + \left(2R^{(3)}_X - 12(R^{(3)}R^{(3)}_\eta) + 2R^{(3)}_{\eta\eta\eta}\right)_\eta - 12\left(T^{(3)}_{\xi\xi}R^{(3)} + T^{(3)}R^{(3)}_{\eta\eta} + 2T^{(3)}_\xi R^{(3)}_\eta\right). \tag{4.31}$$

Similarly for the lower layer, we find

$$-4c^2Q^{(3)}_{\nu\zeta} = \left(2c^2S^{(3)}_X + 12\alpha(S^{(3)}S^{(3)}_\nu) + 2\beta c^2S^{(3)}_{\nu\nu\nu}\right)_\nu + \left(2c^2G^{(3)}_X + 12\alpha(G^{(3)}G^{(3)}_\zeta) + 2\beta c^2G^{(3)}_{\zeta\zeta\zeta}\right)_\zeta + 12\alpha\left(S^{(3)}_{\nu\nu}G^{(3)} + S^{(3)}G^{(3)}_{\zeta\zeta} + 2S^{(3)}_\nu G^{(3)}_\zeta\right). \tag{4.32}$$

Applying averaging in a manner similar to that used for the homogeneous and soft bonded regions yields the KdV equations in the form

$$T^{(3)}_X - 6T^{(3)}T^{(3)}_\xi + T^{(3)}_{\xi\xi\xi} = 0, \tag{4.33}$$

$$R^{(3)}_X - 6R^{(3)}R^{(3)}_\eta + R^{(3)}_{\eta\eta\eta} = 0, \tag{4.34}$$

in the upper layer and

$$c^2S^{(3)}_X - 6\alpha S^{(3)}S^{(3)}_\nu + \beta c^2S^{(3)}_{\nu\nu\nu} = 0, \tag{4.35}$$

$$c^2G^{(3)}_X - 6\alpha G^{(3)}G^{(3)}_\zeta + \beta c^2G^{(3)}_{\zeta\zeta\zeta} = 0, \tag{4.36}$$

in the lower layer. The leading order equations for the upper layer are similar to those in the homogeneous region, but we consider a transmitted wave instead of an incident wave. Substituting (4.33) and (4.34) into (4.31) and integrating with respect to the characteristic variables gives

$$P^{(3)} = 3\left(2T^{(3)}R^{(3)} + R^{(3)}_\eta\int T^{(3)}\mathrm{d}\xi + T^{(3)}_\xi\int R^{(3)}\mathrm{d}\eta\right) + \phi^{(3)}_1(\xi, X) + \psi^{(3)}_1(\eta, X), \tag{4.37}$$

where $\phi^{(3)}_1$, $\psi^{(3)}_1$ are arbitrary functions. Similarly, substituting (4.35) and (4.36) into (4.32) and integrating with respect to the characteristic variables gives

$$Q^{(3)} = 3\alpha\left(2S^{(3)}G^{(3)} + G^{(3)}_\zeta\int S^{(3)}\mathrm{d}\nu + S^{(3)}_\nu\int G^{(3)}\mathrm{d}\zeta\right) + \phi^{(3)}_2(\nu, X) + \psi^{(3)}_2(\zeta, X), \tag{4.38}$$

where $\phi^{(3)}_2$, $\psi^{(3)}_2$ are arbitrary functions.

4.2.4 Matching at the boundaries

We will now use the continuity conditions (4.5) - (4.8) to establish the 'initial conditions' at the interface for each region of the structure. This involves substituting the weakly-nonlinear solution into the continuity conditions and expressing the functions at the interface of a region in terms of the functions from the previous region.

Since the governing equations in Chapter 3 are the same as those for the upper waveguide in our structure, we can use the 'initial conditions' for the reflected and transmitted waves from Chapter 3, expressed in terms of the transmitted wave from the previous section, which are given by

$$R^{(i+1)}|_{x=x_i} = C_R^{(i)} T^{(i)}|_{x=x_i}, \qquad T^{(i+1)}|_{x=x_i} = C_T^{(i)} T^{(i)}|_{x=x_i}, \quad i = 1, 2, 3, \tag{4.39}$$

where we have the reflection coefficient $C_R^{(1)} = 0$ and transmission coefficient $C_T^{(1)} = 1$. Applying a similar methodology for the lower layer we obtain

$$G^{(i+1)}|_{x=x_i} = C_G^{(i+1)} S^{(i)}|_{x=x_i}, \qquad S^{(i+1)}|_{x=x_i} = C_S^{(i+1)} S^{(i)}|_{x=x_i}, \quad i = 1, 2, 3, \tag{4.40}$$

where the transmission and reflection coefficients take the form

$$C_G^{(i)} = \frac{c-1}{c+1}, \qquad C_S^{(i)} = \frac{2}{c\,(1+c)}, \qquad i = 1, \tag{4.41}$$

$$C_G^{(i)} = 0, \qquad C_S^{(i)} = 1, \qquad i = 2, 3. \tag{4.42}$$

With the leading order solutions and initial conditions for each region in place, we can now proceed to our numerical simulations.

4.3 Numerical results

We will apply direct numerical simulations to the system of equations (4.1) – (4.2), along with the continuity conditions (4.5) – (4.8), using the finite difference method detailed in Appendix A.2. The results from this numerical method will be compared with those from a semi-analytical approach, where we will solve the KdV and Ostrovsky equations using a pseudospectral method, as outlined in Appendix B.

4.3.1 Zero mass - Boussinesq equation initial condition

We build on the method from Section 3.4.1 for a single Ostrovsky equation, applying it to the coupled Ostrovsky equations. To illustrate, we consider the equation for the transmitted wave in the upper bar, (4.25), and integrate both sides over the x to give

$$\int_{-\infty}^{\infty} \left(T_X^{(i)} - 6T^{(i)}T_\xi^{(i)} + T_{\xi\xi\xi}^{(i)}\right)_\xi \,\mathrm{d}x = \delta \int_{-\infty}^{\infty} T^{(i)} \,\mathrm{d}x. \tag{4.43}$$

For the coupled Ostrovsky equation, any periodic solution on a finite domain (or a localised solution on a sufficiently large domain) must have zero mass. Under this assumption, the left-hand side vanishes, thus

$$\int_{-\infty}^{\infty} T^{(i)} \,\mathrm{d}x = 0. \tag{4.44}$$

An identical argument applied to the other three Ostrovsky equations, (4.27), (4.23) and (4.28), yields

$$\int_{-\infty}^{\infty} S^{(i)} \,\mathrm{d}x = 0, \quad \int_{-\infty}^{\infty} R^{(i)} \,\mathrm{d}x = 0, \quad \int_{-\infty}^{\infty} G^{(i)} \,\mathrm{d}x = 0. \tag{4.45}$$

However, due to the coupling between the bars, we express these conditions in a form that reflects this interaction. In particular, we combine them as

$$\int_{-\infty}^{\infty} \left(T^{(i)} - S^{(i)}\right) \,\mathrm{d}x = 0, \quad \int_{-\infty}^{\infty} \left(R^{(i)} - G^{(i)}\right) \,\mathrm{d}x = 0, \tag{4.46}$$

which ensures that the net mass carried by the transmitted and reflected waves is balanced across the coupled system. For the initial conditions, (4.1) and (4.2), taking the integral of the strain solitary wave solution of (4.3) we get

$$\begin{aligned} u\,(x,0) &= A\left[\tanh\left(\frac{x}{\Lambda}\right) - 1\right] - \Gamma\left[\tanh\left(\frac{x+x_0}{\Lambda S}\right) + \tanh\left(\frac{x-x_0}{\Lambda S}\right) - 2\right], \\ u\,(x,\kappa) &= A\left[\tanh\left(\frac{x-\kappa v}{\Lambda}\right) - 1\right] - \Gamma\left[\tanh\left(\frac{x+x_0-\kappa v}{\Lambda S}\right) + \tanh\left(\frac{x-x_0-\kappa v}{\Lambda S}\right) - 2\right], \end{aligned} \tag{4.47}$$

where we have $A = -\frac{v\sqrt{v^2-1}}{\sqrt{2\varepsilon}}$, $\Lambda = \frac{2\sqrt{2\varepsilon}v}{\sqrt{v^2-1}}$ and

$$\Gamma = \frac{\sigma A \tanh\left(\frac{L}{\Lambda}\right)}{\tanh\left(\frac{L+x_0}{\Lambda S}\right) + \tanh\left(\frac{L-x_0}{\Lambda S}\right)}.$$

Here for the semi-analytical calculations, the domain length is considered to be $2L$ and x_0 represents an arbitrary phase shift, $\sigma = 1$, and κ is set to Δt. Γ is chosen to ensure a zero mean value for f, with the same initial condition applied to g. Throughout the cases discussed, S and x_0 are set to 10. For the lower layer, identical expressions are used for both $w(x, 0)$ and $w(x, \kappa)$, as the equations remain consistent across both layers.

4.3.2 Zero mass - KdV equation initial condition

Following Section 3.4.1, for the weakly-nonlinear solutions, we take the exact solitary wave solution derived from the KdV equation (4.14), which governs the incident wave, as

$$I(\xi, 0) = \tilde{A}\ \mathrm{sech}^2\left(\frac{\xi}{\tilde{\Lambda}}\right) - \frac{\tilde{\Gamma}}{S}\left[\mathrm{sech}^2\left(\frac{\xi + x_0}{\tilde{\Lambda}S}\right) + \mathrm{sech}^2\left(\frac{\xi - x_0}{\tilde{\Lambda}S}\right)\right], \tag{4.48}$$

where $\tilde{A} = -\frac{v_1}{2}$, $\tilde{\Lambda} = \frac{2}{\sqrt{v_1}}$ and

$$\tilde{\Gamma} = \frac{A\ \tanh\left(\frac{L}{\Lambda}\right)}{\tanh\left(\frac{L+x_0}{\Lambda S}\right) + \tanh\left(\frac{L-x_0}{\Lambda S}\right)}.$$

The relationship between v and v_1 is given by the approximation $v = 1 + \varepsilon v_1 + \mathcal{O}(\varepsilon^2)$. To determine the initial conditions in other regions of the structure, we use the relations from Section 4.2.4 to express them in terms of (4.48).

4.3.3 Base case simulations

For our numerical schemes, in the direct numerical simulations, we use step sizes of $\Delta x = \Delta t = 0.01$, and for the pseudospectral method we use $\Delta\xi = 0.1$ (the same step size for all characteristic variables) and $\Delta X = 5 \times 10^{-4}$. These are the same step sizes that we employed in Chapter 3. The coefficients are set as $\alpha = \beta = 1 + \varepsilon$ and $\delta = \gamma = 0.5$. The boundary conditions are $u_x = f = 0$ on both the left and right sides of the bar, assuming constant displacements on the left and propagation into an unperturbed medium on the right. These are the same as the boundary conditions that were used in developing the numerical method in [77], which we are also using to solve our equations.

Firstly, we will run a base case simulation for the bi-layer waveguide with semi-infinite delamination, as shown in Figure 4.1(a), and compare the results of the direct numerical simulations with the semi-analytical results.

The comparative analysis in Figure 4.2 shows excellent agreement between the two numerical schemes across all regions and layers. In the upper layer, we observe an incident soliton in the homogeneous region, which evolves into an Ostrovsky wave packet as it propagates into the soft bonded region, consistent with

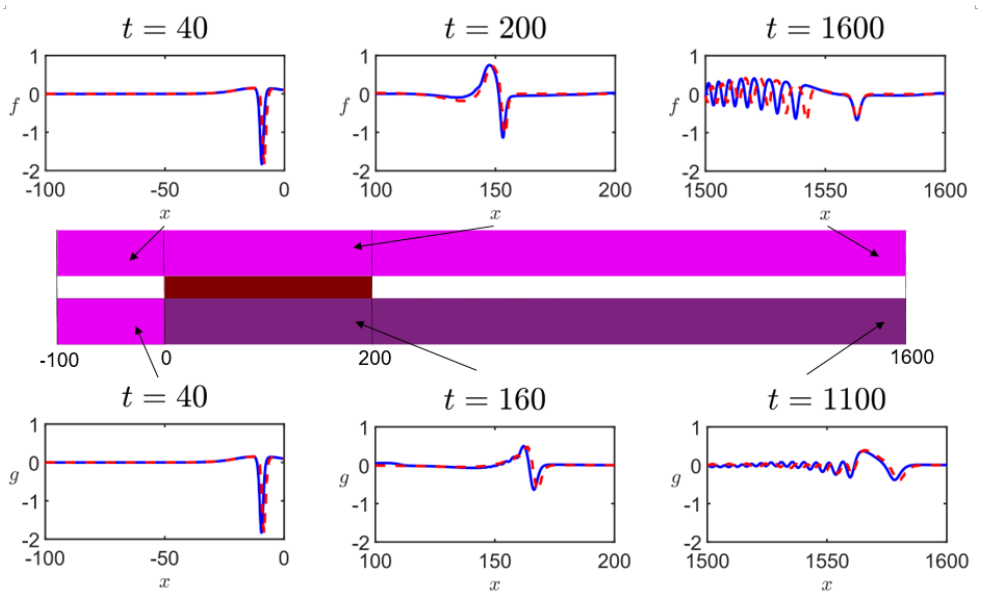

Figure 4.2: The waves in the waveguide with semi-infinite delamination for direct numerical simulations (blue, solid line) and the semi-analytical solution (red, dashed line). Parameters are $v = 4$, $\varepsilon = 0.005$, $c = 1.0$ and $\gamma = 1$ for the upper layer and $c = 1.5$ and $\delta = 1$ for the lower layer. For the finite difference method, the spatial domain is $x \in [-100, 1600]$. In the pseudospectral method, the number of points for the Discrete Fast Fourier Transform (DFFT) is $N = 65,536$.

the expected outcomes in [93, 94]. As the wave packet moves from the soft bonded region into the delaminated region, it evolves into solitons and dispersive radiation. The leading soliton separates and becomes distinct from the trailing radiation, while the remaining peaks continue to separate but are not yet clearly identifiable as solitons.

In the lower layer, the wave behaves similarly to the upper layer but shows less evolution due to the higher characteristic speed and shorter time spent in each region. The agreement between the two numerical schemes could be improved by including higher-order terms or reducing the value of ε. In [48], where the characteristic speeds in each layer are close, a radiating solitary wave formed in the bonded sections of the structure. In the delaminated sections, the solitary wave separated from its co-propagating tail.

In Figure 4.3, we present a computation for the same waveguide configuration as shown in Figure 4.2, but with $\varepsilon = 0.01$. Performing a full error analysis as $\varepsilon \to 0$ is challenging, as the equation essentially reduces to the linear wave equation for the initial wave. However, we observe that the error is larger for higher ε values, evidenced by a greater disparity in wave position and amplitude between the two numerical schemes. The accuracy of the semi-analytical method could be improved by including higher-order terms, but this is beyond the scope of this thesis. For subsequent calculations in this chapter, we will use $\varepsilon = 0.005$, where the agreement between methods is stronger.

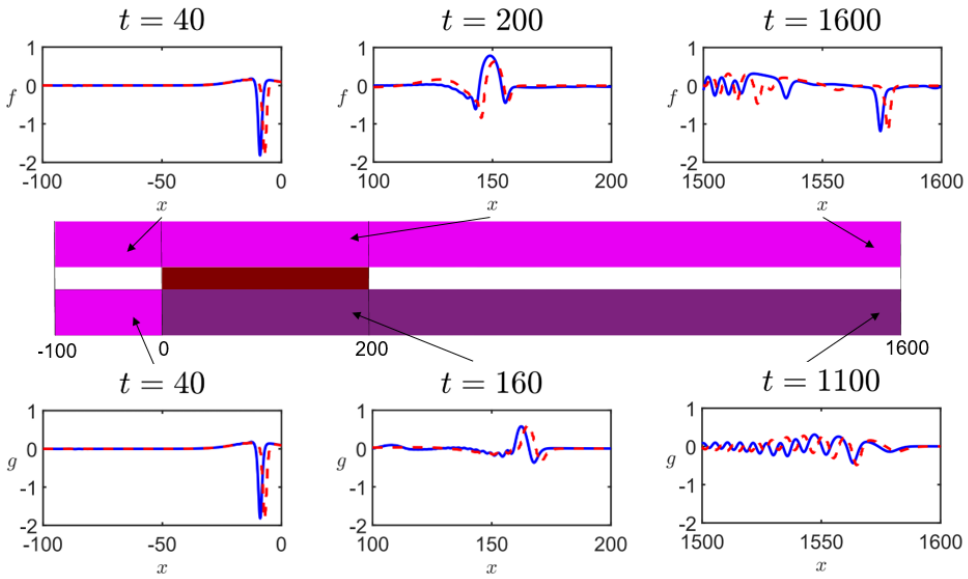

Figure 4.3: The waves in the waveguide with semi-infinite delamination, with parameters similar to Figure 4.2 except $\varepsilon = 0.01$.

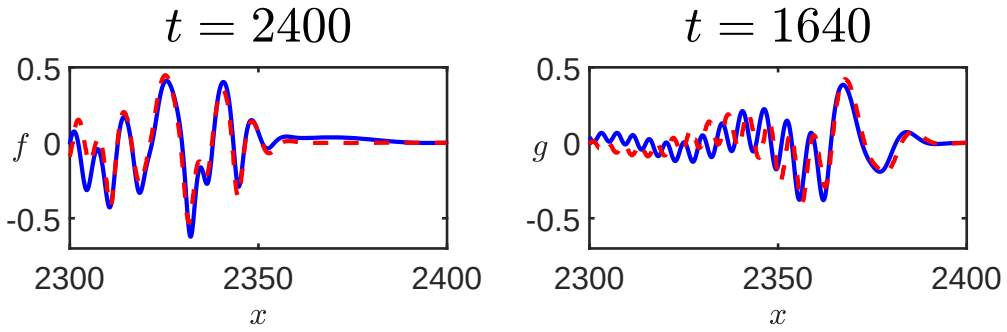

Figure 4.4: The waves in the final section of Figure 4.1(b) for the base case simulation at $t = 2400$ in the upper layer and $t = 1640$ in the lower layer. The parameters are the same as Figure 4.2, comparing the direct numerical simulation (blue, solid line) and the semi-analytical solution (red, dashed line).

Next, we modify the infinite delamination scenario shown in Figure 4.2 by introducing an additional soft bonded region within the interval $1600 < x < 2400$, creating a finite delamination case. This is the structure depicted in Figure 4.1(b). The wave scattering in the newly included final soft bonded region is presented in Figure 4.4. In both layers, we see an Ostrovsky wave packet has evolved from a solitary wave, mirroring the observations from the first bonded region. Additionally, radiation trailing behind the leading wave packet may mask any subsequent wave packets that were generated by other solitons. This behaviour is more pronounced in the upper waveguide, as the lower characteristic speed results in more noticeable evolution. While there is good agreement around the leading wave packet, the accuracy diminishes away from it due to the absence of higher-order correction terms.

At this point, we have demonstrated a strong agreement between the two numerical approaches. The computations were performed on an Intel Core i7-1255U processor, featuring 10 cores, 12 threads, and a maximum clock speed of 4.70GHz. The direct numerical approach to the cRB equations required 16 hours and 40 minutes, whereas the semi-analytical approach completed in just 25 minutes, yielding a speed increase of 40 times. Additionally, the semi-analytical method scales with ε, meaning that for larger values of ε, if the agreement between the two numerical schemes remains reasonable, this scaling could further reduce computation time. Given agreement at the leading peaks is strong, we will use the semi-analytical method for the remaining calculations in this chapter.

4.3.4 Linear dispersion relation

We establish a theoretical prediction of the wave speed by using the linear dispersion relations, to further understand the wave packet behaviour, as in Section 3.4.4. The solutions $I \approx I_0 e^{i(k\xi - \omega X)}$ and $T^{(2)} \approx T_0 e^{i(k\xi - \omega X)}$, where ω is the wave frequency and k is the wavenumber, are the linearised solutions of the KdV equation (4.14) and the Ostrovsky equation (4.25) (or equivalently (4.27)), respectively. Substituting the expressions for I and $T^{(2)}$ into (4.14) and (4.25), respectively, gives

$$\omega(k) = -\beta k^3 \text{ for } I \text{ and } \omega(k) = \frac{\gamma}{c^2 k} - \beta k^3 \text{ for } T^{(2)}. \tag{4.49}$$

The phase speed is defined as $p = \omega/k$, so

$$p(k) = -\beta k^2 \text{ for } I \text{ and } p(k) = \frac{\gamma}{c^2 k^2} - \beta k^2 \text{ for } T^{(2)}.$$

The group velocity is calculated as

$$c_g(k) = -3\beta k^2 \text{ for } I \text{ and } c_g(k) = -\frac{\gamma}{c^2 k^2} - 3\beta k^2 \text{ for } T^{(2)}. \tag{4.50}$$

The speed of solitons within the delaminated region lies within the spectral gap, specifically we have $p > 0$, but also close to $p = 0$. Using a similar methodology to that in Section 3.4.4, but using the characteristic variables $\xi = x - ct$ and $X = \varepsilon x$ instead, we predict the wave speed in the soft bonded region as

$$v_b = \frac{c}{1 - \varepsilon x_s}. \tag{4.51}$$

where x_s is the minimum phase shift, which corresponds to the distance travelled in the characteristic frame for each unit increase in X. For the specific case when $c = 1$, this simplifies to (3.55). The dispersion

relations, phase speeds, and group speeds can be plotted against the wavenumber using a similar method to that in Chapter 3, adapted for the equations used here. The maximum value of c_g for the soft bonded region can then be substituted into (4.51), along with the values of ε and c, to determine the wave speed in that region.

Table 4.1 presents the theoretically predicted wave speed, v_b, and the simulated wave speed, v_4, for the second soft bonded region in the finite delamination base case described in Section 4.3.3, across various values of c. The table also shows the difference between these two wave speeds.

Characteristic speed, c	v_4	v_b	**Difference, %**
1.0	1.00139	0.98787	1.352
1.1	1.10628	1.08895	1.733
1.2	1.20537	1.18985	1.552
1.3	1.30651	1.29062	1.589
1.4	1.40577	1.39128	1.449
1.5	1.51098	1.49186	1.912

Table 4.1: The predicted speed of the wave in the soft bonded regions, v_b, and the numerically observed wave speed in the final soft bonded region, denoted v_4, for various characteristic speeds, c.

When calculating the numerically observed wave speed, we use the leading wave peak as a reference point. The speed is measured over a few hundred nondimensional units of time, beyond which the faster-moving trailing radiation interacts with the wave peak, making it increasingly indistinct and difficult to identify. In Section 3.4.7, the front of the wave packet was used instead. Although the front of the wave packet could extend the second soft bonded region over a larger distance and time, reducing the discrepancy between v_4 and v_b, locating the front of the wave packet becomes increasingly difficult the longer the waves propagate and evolve. Therefore, in Section 4.3.5, we analyse the behaviour of both the leading wave peaks and the front for varying delamination lengths to determine which reference point is easier to interpret and more suitable for subsequent calculations.

4.3.5 Leading wave peak analysis

Figure 4.5 shows the waves near the end of the second soft bonded region in cases similar to our base case simulation but with varying delamination lengths. The leading peaks are highlighted with dots, and a spline interpolation function is used in this and subsequent sections in this chapter to interpret the data between discretised points, providing a continuous wave and improving the accuracy in tracking the leading peak. Since our initial condition is negative, we treat the local minima as "peaks" in relation to this setup. If the initial condition were positive, with the nonlinear term also positive, we would instead identify the local maxima as the peaks. The region where the leading peak is expected is determined by

using information on the distance the wave packet propagates. Working from right-to-left, we identify the first peak that exceeds a threshold of $0.1 \times \min(f)$, thereby avoiding the false inclusion of any low-amplitude oscillations.

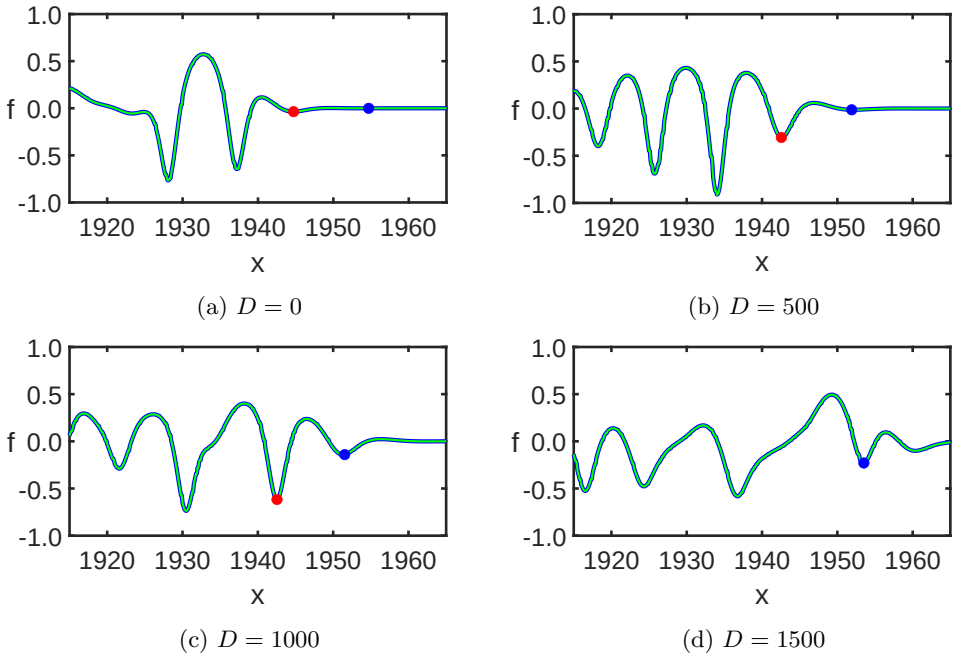

(a) $D = 0$ (b) $D = 500$

(c) $D = 1000$ (d) $D = 1500$

Figure 4.5: The waves in the upper layer of a structure with a homogeneous region from $x_0 = -100$ to $x_1 = 0$, a soft bonded region from $x_1 = 0$ to $x_2 = 300$, a delaminated region from $x_2 = 300$ to $x_3 = 300+D$ (with various delamination lengths D), followed by a second soft bonded region up to $x_4 = 2000$. In the simulation, which runs up to $t = 2000$, the leading wave peak for $D = 0$ is marked in red, while the next leading peak that emerges as the delamination length increases is marked in blue.

The peak marked with a red dot at $D = 0$ has an amplitude of $f = -0.036$. For larger delamination lengths, this peak shifts further into the trailing radiation, and the leading peak, marked by the blue dot, becomes more prominent. There are additional peaks forming; however, we only highlight the initial two that developed to demonstrate this concept. At $D = 1000$, the peak with the blue dot has an amplitude of $f = -0.142$. This indicates that as the delamination length increases, the overall wave packet advances while the peaks, in most cases, retreat into the radiation. For instance, at $D = 0$, the blue peak at $x = 1955$ is near or at the front of the wave packet, as the wave tends towards zero beyond that point. However, at $D = 1500$, the front of the wave packet appears to extend beyond $x = 1965$. This is consistent with the expectation that waves propagate faster in delaminated regions than in soft bonded regions. As a result, the longer the delamination, the further the wave packet propagates if all other variables are the same [75]. We also observe that before the wave peak enters the radiation, the leading wave peak is much easier to visually identify than the front of the wave packet. Due to its consistent and reliable behaviour over time, we will adopt the leading wave peak as our reference point in the subsequent sections. Although

the analysis in this section is based on the case where $x_2 = 300$, the observations are applicable to soft bonded regions of any length, where we will explore varying soft bonded region in the next section.

4.3.6 Varying delamination length and position

In Section 3.4.7, we investigated the wave behaviour in the final bonded region of the upper layer when varying the delamination length, $D = x_3 - x_2$, while keeping the delamination starting position fixed at $x_2 = 300$. In this section, we extend the analysis by varying both the delamination length and its position, considering both waveguides. Our objective is to calculate phase shifts, which are the differences in the positions of leading wave peaks relative to a fully bonded case, for various delamination lengths and positions. Using these calculations, we will explain how to determine the delamination length and position based upon the observed phase shifts.

Firstly, we focus on the upper layer within the structure containing finite delamination described in Section 4.3.3, using the same parameters. We will vary the delamination length, D, from 0 (no delamination) to 400 in increments of 50. Simultaneously, the delamination position, x_2, will be varied from 0 (no initial soft bonded region) to 1500. This range allows us to explore the full spectrum of delamination starting positions for a bar $0 \leq x \leq 2000$. We will calculate the phase shift near the end of the second soft bonded region by comparing the position of the leading wave peak in the fully bonded case to that in each configuration with delamination. The maximum computational time for the calculations is set at $t = 2000$.

Figure 4.6 shows that for $x_2 = 0$, the phase shift increases almost linearly with the delamination length. As x_2 increases, the phase shift continues to grow with the delamination length until $x_2 = 200$, where it begins to decrease. This decreasing trend then continues until $x_2 = 450$, after which the phase shift starts to rise again, following a nonlinear curve. For the remaining x_2 values up to $x_2 = 1500$, the phase shift generally increases or decreases consistently with the delamination length, with only rare instances of reversal. Each graph displays a 'fan' shape, which makes it easier to see the underlying trends. Without these 'fans', plotting all curves on a single graph would lead to overlapping, which could obscure the trends and complicate the interpretation of the results.

Assessing the time required to compute these wave fans, each line of a fan contains 9 points, and there are 29 lines in total in Figure 4.6. Using the semi-analytical approach, the total computation time is approximately 109 hours. In contrast, the direct numerical scheme would require about 2,800 hours to complete. Using the previously mentioned Intel Core i7-1255U processor with 10 cores and 12 threads, we are able to perform 12 computations concurrently. With this setup, the semi-analytical method requires approximately 9 hours and 4 minutes to complete. This demonstrates that the semi-analytical

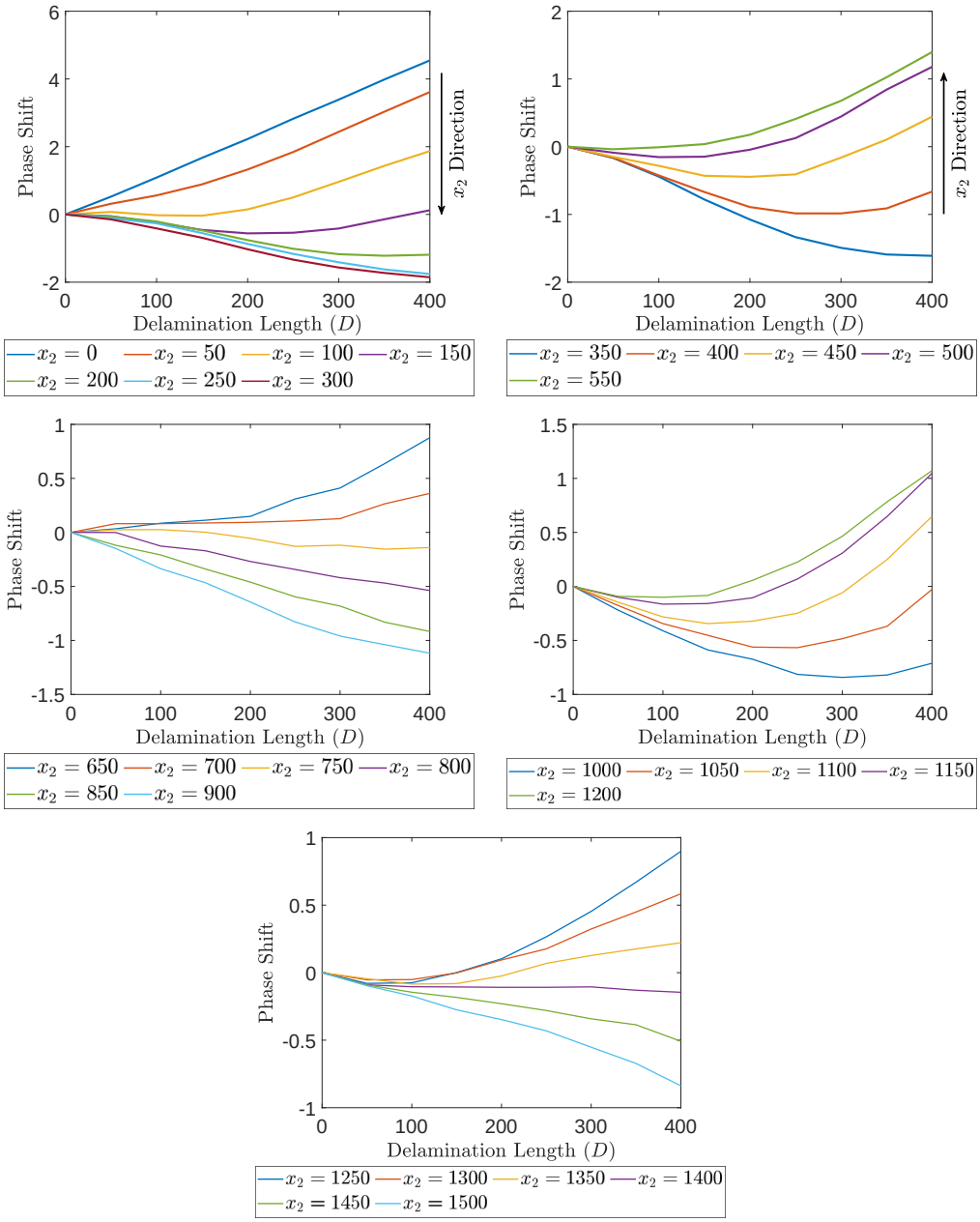

Figure 4.6: Plots showing the phase shift of the leading wave peak for delamination lengths from $D = 50$ to $D = 400$ compared to the fully bonded case in the upper layer. We also vary the delamination position from $x_2 = 0$ to $x_2 = 1500$ and take the characteristic wave speed to be $c = 1.0$. The direction of x_2 is indicated in the first two plots, with the subsequent plots following a downward-upward alternating pattern.

method allows for reasonable computation times, even without specialised hardware. Additionally, if the material properties change, these calculations must be redone with updated parameters. By using the semi-analytical approach, significant computation time is saved whenever testing new materials.

Now, we focus on the lower layer in Figures 4.7 and 4.8, where $c = 1.25$ and $c = 1.5$, respectively.

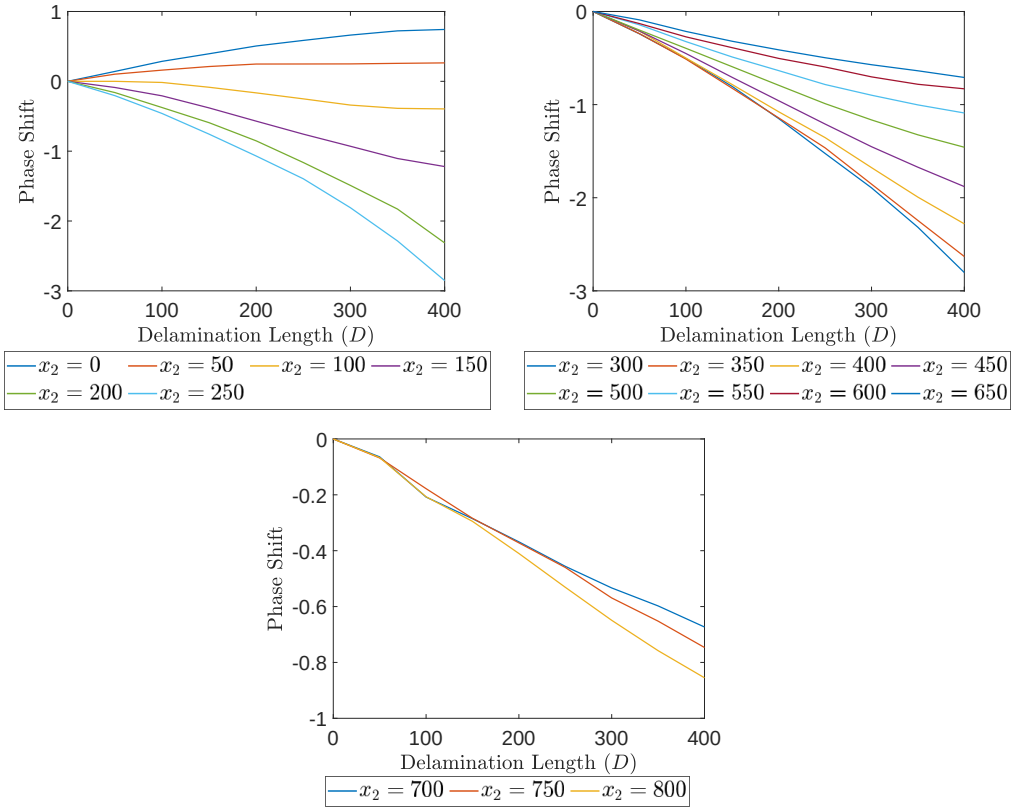

Figure 4.7: Plots showing the phase shift for delamination lengths $D = 50$ to $D = 400$ compared to the fully bonded case in the lower layer. The delamination position is varied from $x_2 = 0$ to $x_2 = 800$ and we take the characteristic wave speed to be $c = 1.25$.

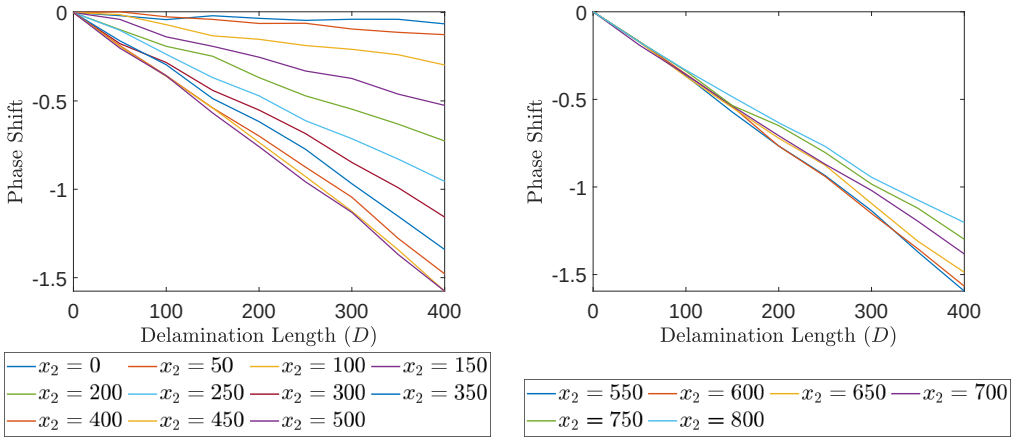

Figure 4.8: Plots showing the phase shift for delamination lengths $D = 50$ to $D = 400$ compared to the fully bonded case in the lower layer. The delamination position is varied from $x_2 = 0$ to $x_2 = 800$ and we take the characteristic wave speed to be $c = 1.5$.

A similar pattern to the upper layer is observed; however, for $c = 1.5$, there is minimal variation in the curves between successive x_2 values due to the slower evolution rate. Additionally, for $c = 1.5$, curves

overlap for smaller delamination lengths, also owing to the slower evolution. Figure 4.9 shows the gradient of the phase shift curves for each x_2 value.

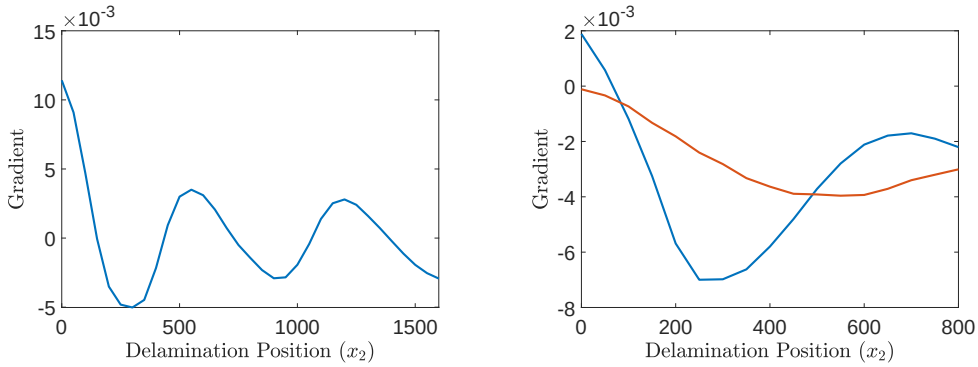

Figure 4.9: Gradient plots for all x_2 values in the upper layer (left) with $c = 1.0$, and the lower layer (right) with $c = 1.25$ (blue) and $c = 1.5$ (red).

Figure 4.9 shows that for $c = 1.0$ in the upper layer, the phase shift curve with the greatest gradient occurs at $x_2 = 0$, and this gradient steadily decreases as x_2 increases, reaching its lowest point around $x_2 = 350$. It then gradually increases from $x_2 = 350$ to $x_2 = 550$. Similar behaviour is observed for $c = 1.25$ and $c = 1.5$, with the overall fluctuations in gradient becoming progressively smaller as c increases.

The gradient plots serve two main purposes in this context. Firstly, they clearly reveal the gradient's tipping points, which help determine when to transition to a new graph for plotting the phase shift curves. By separating the curves at these points where the gradient switches from increasing to decreasing, or vice versa, we avoid overlap and ensure a clearer visual representation. Secondly, the gradient plots highlight broader behavioural trends. For example, in the $c = 1.0$ case, the progressively smaller amplitudes of successive peaks and troughs indicate that, for large values of x_2, the differences between phase shift curves diminish significantly.

In an engineering context, it may be necessary to analyse two structures with configurations similar to those in Figure 4.1, where in one structure the delaminated region is absent (i.e., $D = 0$), but in the structure containing delamination, the position and length of the delaminated region are unknown. The goal of this analysis is to determine the position and length of delamination in the damaged structure by comparing the position of the leading wave peak near the end of the damaged structure to that of the structure without delamination.

For example, consider a phase shift of -1.5 being observed in the upper layer and -2.01 in the lower layer, where the lower layer has a characteristic speed of $c = 1.25$. By referencing Figures 4.6 and 4.7, we find that in the upper layer, a phase shift of -1.5 intersects at $x_2 = 250, 300, 350$ with corresponding delamination

lengths of $D = 321, 285, 303$, respectively. Similarly, for the lower layer with $c = 1.25$, a phase shift of -2.01 intersects at $x_2 = 200, 250, 300, 350, 400$ with delamination lengths of $D = 369, 321, 314, 320, 353$, respectively. Given that both the upper and lower layers have values of $x_2 = 250$ with $D = 321$ under these respective phase shifts, we can infer that these values likely represent the delamination start position and length for the damaged structure.

Figure 4.10 presents two additional phase shift cases, each with common delamination lengths and positions in the upper and lower layers. Figure 4.10(a)-(b) represents the second case, with Figure 4.10(a) showing the upper layer and Figure 4.10(b) the lower layer. Similarly, Figure 4.10(c)-(d) represents the third case, with Figure 4.10(c) showing the upper layer and Figure 4.10(d) the lower layer. Instead of displaying the entire range of x_2 values, Figure 4.10 shows only the values that intersect with the given phase shifts.

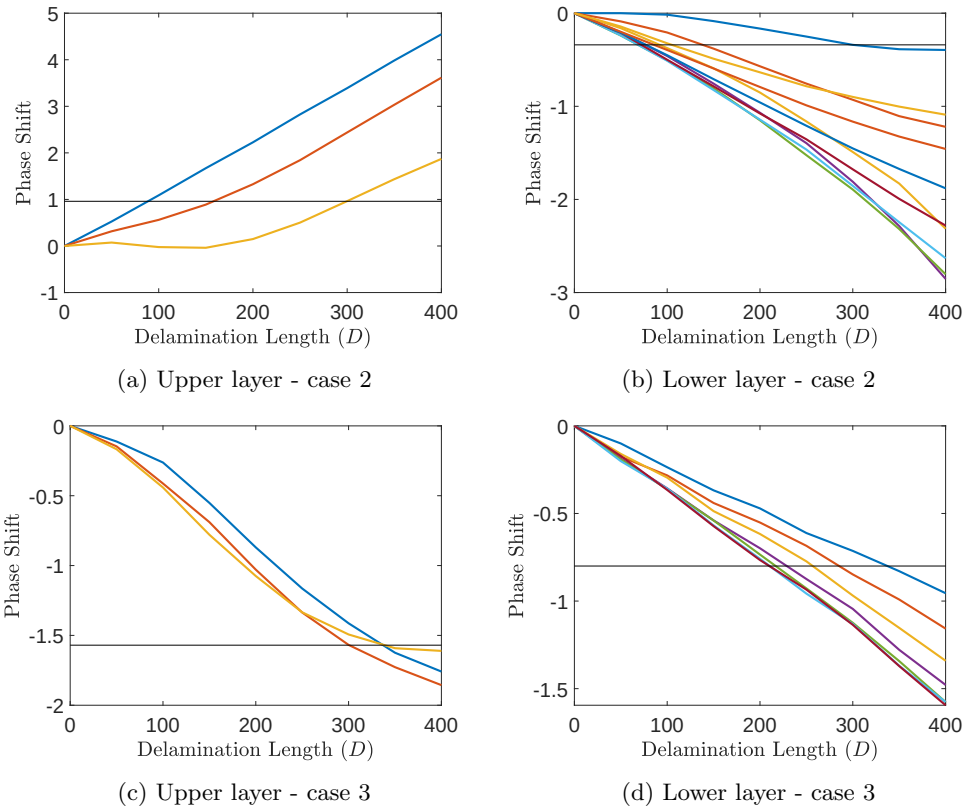

(a) Upper layer - case 2

(b) Lower layer - case 2

(c) Upper layer - case 3

(d) Lower layer - case 3

Figure 4.10: Plots of all the phase shifts curves that intercept arbitrary phase shift values (horizontal black lines) at 0.96 and -0.34, for case 2, as well as -0.80 and -1.57, for case 3.

Figure 4.10(a)-(b) shows that a phase shift of 0.96 intersects the upper waveguide, while a phase shift of -0.34 intersects the lower layer, both at $x_2 = 100$ and $D = 300$. This indicates that the structure has delamination starting at $x_2 = 100$ with a length of $D = 300$. Similarly, for case 3, phase shifts of -1.57

and -0.80 intersect the upper and lower layers, respectively, at $x_2 = 250$ and $D = 337$. From this we can infer the delamination length and position based on these phase shifts. As mentioned earlier, in practical applications where the structure's configuration is often unknown, the phase shift can help determine the delamination length and position. In theory, this approach can be applied to further cases as well, allowing for a broader range of configurations to be analysed.

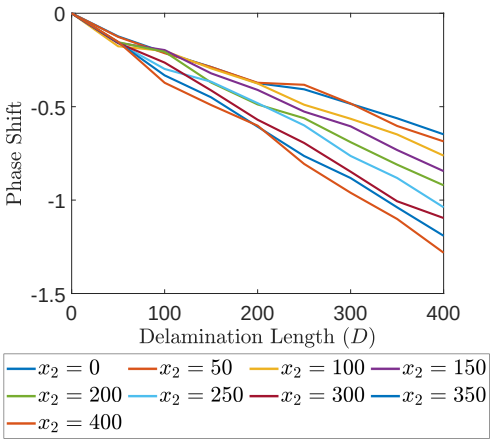

Figure 4.11: Plots of the change in phase shift, with reference to the fully bonded case, in the lower layer from $x_2 = 0$ to $x_2 = 400$ for $c = 2.0$.

If we consider the case when $c = 2.0$, we observe even less discrepancy between x_2 values, with some overlap occurring between all of them. As a result, larger c values will not be used in the remainder of the analysis, as the lack of variation in the x_2 curves makes it difficult to distinguish between them and detect delamination. Instead, we can extend our analysis by examining wave propagation in the reverse direction.

4.3.7 Reversing the direction of wave propagation

Next, we examine the scenario where wave propagation occurs from right to left in the upper layer with $c = 1.0$. This configuration is considered because the $c = 1.5$ case discussed previously resulted in excessive overlap between x_2 values, limiting its usefulness. In this case, we use $\tilde{x}$ to denote the position along the bar on the horizontal x-axis, where $\tilde{x}$ increases as we move to the left.

In this configuration, for our numerical analysis, the initial homogeneous region is from $\tilde{x}_0 = -100$ to $\tilde{x}_1 = 0$. The waveguides from $\tilde{x}_1$ to $\tilde{x}_2$ are soft bonded, where $\tilde{x}_2$ indicates the start of the delaminated region. The end of the delaminated region is denoted by $\tilde{x}_3 = \tilde{x}_2 - D$, and the second soft bonded region is from $\tilde{x}_3$ to $\tilde{x}_4 = 2000$.

Importantly, as the position of $\tilde{x}$ in this reverse case corresponds to a spatial reflection of x when

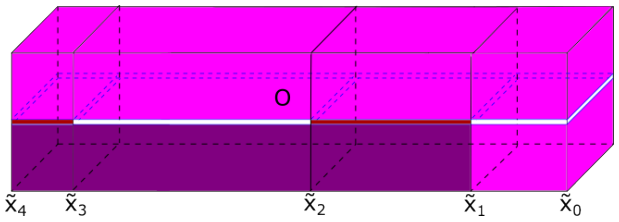

Figure 4.12: Schematic of the bi-layer structure where wave propagation occurs from from right to left. A homogeneous region is from $\tilde{x}_0 < \tilde{x} < \tilde{x}_1$, followed by a soft bonded region for $\tilde{x}_1 < \tilde{x} < \tilde{x}_2$ and a delaminated region for $\tilde{x}_2 < \tilde{x} < \tilde{x}_3$, and another soft bonded region for $\tilde{x}_3 < \tilde{x} < \tilde{x}_4$. We assume the homogeneous section has the same material properties of the upper layer and for the other three sections, the material in both layers has similar properties.

the wave propagates from left to right, the previously computed results can be used without additional simulations.

While reassigning the soft bonded regions in the left to right case can reproduce the reversed case, modelling wave propagation from right to left enables delamination to be identified within a single, fixed structure. This is more practical both experimentally, since generating waves from both ends of one setup is simpler than analysing two separate configurations, and analytically, as it preserves a clear correspondence between spatial coordinates and structural layout.

Similarly to the case when the wave propagated from left to right, by varying the delamination length and position, we can calculate and use the phase shift, as depicted in Figure 4.13, to determine the structure configuration. This provides another effective tool for detecting delamination, particularly in situations where the wave propagation in the lower layer is not observed, such as when the lower layer has a significantly higher characteristic wave speed.

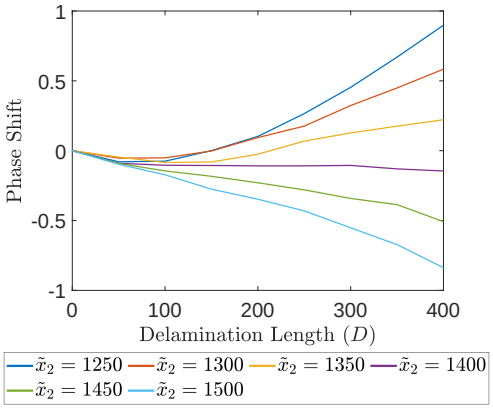

Figure 4.13: A plot of the change in phase shift, with reference to the fully bonded case, for $\tilde{x}_2 = 1250$ to $\tilde{x}_2 = 1500$ in the upper waveguide, when the wave propagation is from right to left.

In Figure 4.13, a similar fan shape is observed in the upper layer as was observed when the wave moves

from left to right. As an example of how this can be applied, for a phase shift of -0.342, from Figure 4.13 we observe one of the intersections occurs at $\tilde{x}_2 = 1450$ with corresponding delamination lengths of $D = 300$. For left-to-right propagation, a phase shift of -1.415 corresponds to a delamination length of $D = 300$ at $x_2 = 250$. Figure 4.14 shows the structural configurations for the phase shift values of -1.415 when the wave propagates from left to right and -0.342 when it propagates from right to left, both in the upper layer.

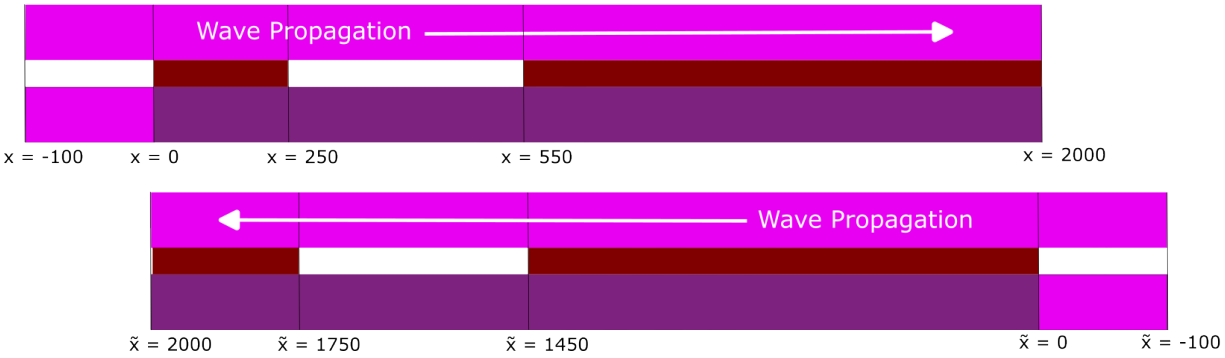

Figure 4.14: Structure configurations for phase shifts of -1.415 with wave propagation from left to right (top) and -0.342 with wave propagation from right to left (bottom), both observed in the upper layer.

From Figure 4.14, we observe that the delamination length and position are the same for both structures, confirming that the delamination is from $x = 250$ to $x = 550$. This method is applied only to the upper layer due to overlapping phase shifts in the lower layer, making it difficult to detect the corresponding delamination lengths and positions.

4.4 Summary

In this chapter, we extended the analysis from Chapter 3, which focused solely on the upper layer of a two-layered structure, to include both layers. Previous studies have examined similar cases with identical layers and perfect bonding [45,47], as well as soft bonding with similar material properties [47]. However, in these last two chapters, we have investigated the emergence of Ostrovsky wave packets in systems where the layers have distinct properties.

We modelled the longitudinal displacements within the waveguide using coupled Boussinesq equations and applied a direct numerical simulation method, as detailed in Appendix A. We then applied a semi-analytical approach based on matched asymptotic multiple-scale expansions and averaging with respect to the fast space variable. Our results showed that the semi-analytical approach was approximately 97.5% faster than the direct numerical simulations. We then compared the results from both numerical schemes

and demonstrated that they agree well around the main wave packet, with some divergence observed in the trailing radiation. This could be addressed by including higher-order corrections in the weakly-nonlinear solution, as shown for the corresponding initial-value problem for a single section in [76]. Our numerical simulations further revealed the emergence of Ostrovsky wave packets within the soft bonded regions and solitons in the delaminated region, across both waveguides. We also applied the linear dispersion relation to the KdV and Ostrovsky equations to predict the wave speed in the soft bonded region and validated our simulation results for various values of c.

We found that varying the delamination length caused a phase shift in the leading wave peak position compared to the case with no delamination, for various delamination starting positions. We plotted these phase shifts and identified common delamination lengths and positions for given phase shift values in both waveguides, revealing the structural configuration and providing a tool for detecting delamination. When the layers have significantly different characteristic speeds, such as $c = 1.0$ in the upper layer and $c = 2.0$ in the lower layer, we observed substantial overlap among the x_2 phase shift curves in the lower layer, making it difficult to interpret the results. In such cases, we used the phase shifts for waves propagating in the opposite direction through the upper layer. This represents a significant advancement in the study of detecting delamination within layered structures, as it is the first instance, to our knowledge, where nonlinear waves have been used to identify both the position and length of a delamination. Previous studies [47, 48] and Chapter 3 only identified the delamination length

Throughout this thesis, we have mostly utilised phase shifts and the theoretical prediction of wave speed from the linear dispersion relation. In the next chapter, we will instead leverage the wave's amplitude and the Inverse Scattering Transform (IST) to explore additional methods for detecting delamination.

Chapter 5

Scattering of a radiating solitary wave in a two-layered waveguide

In this chapter, we will examine the scattering of a long longitudinal solitary wave as it propagates through the layers of multi-layered structures that feature delamination at the centre, with either perfectly bonded or soft bonded regions on either side of the delaminated region. In the perfectly bonded scenario, we will consider waveguides of identical materials, which are governed by a system of Boussinesq equations. For the soft bonded case, the longitudinal displacements will be governed by coupled Boussinesq equations, similar to those discussed in Chapter 4. However, in contrast to Chapter 4, the two layers will have characteristic speeds that are more closely matched.

In the case of perfect bonding in Section 5.1, we construct a weakly-nonlinear solution to derive leading order solutions, then the Inverse Scattering Transform (IST) is used to theoretically predict wave amplitude, and while this is similar to Section 3.4.2, we will explore the IST in greater depth in this chapter. In a similar way to Chapters 3 and 4, our goal is to determine the delamination length through numerical simulations. However, unlike the previous chapters, which focused on phase shift relative to the case with no delamination, here we will analyse the amplitude difference between the incident wave in the first region and the transmitted wave in the third region for various delamination lengths and Full Width at Half Maximum (FWHM) values, a common soliton measure in experiments.

We will also consider various structure configurations and geometries as well as a range of FWHM values. Based on these findings, we will develop a scaling that generalises all FWHM cases to match the results of a single case, allowing us to compute just one case, thereby enhancing the computational efficiency.

In the soft bonded case, we use the difference in the numerically observed wave amplitudes between the first and second soft bonded regions, rather than creating a measure with the IST, which cannot be applied to the coupled Ostrovsky equations. The results of this chapter are partially summarised in [103].

5.1 Perfectly bonded case

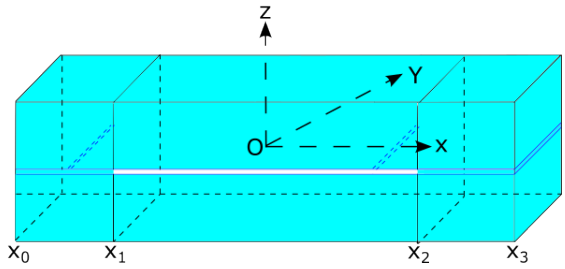

Figure 5.1: Bi-layer structure with an initial perfectly bonded region for $x_0 < x < x_1$, a delaminated region for $x_1 < x < x_2$ and a perfectly bonded region for $x_2 < x < x_3$. We assume that the materials in both layers are identical.

Figure 5.1 illustrates a perfectly bonded two-layered structure with delamination in the centre. Although the scenario depicted in Figure 5.1 shows two layers, the arrangement can accommodate any symmetrical number of layers, assuming uniform material properties and identical bonding (or lack thereof) between each consecutive pair of layers. For example, this could be extended to three layers, as shown in Figure 5.2.

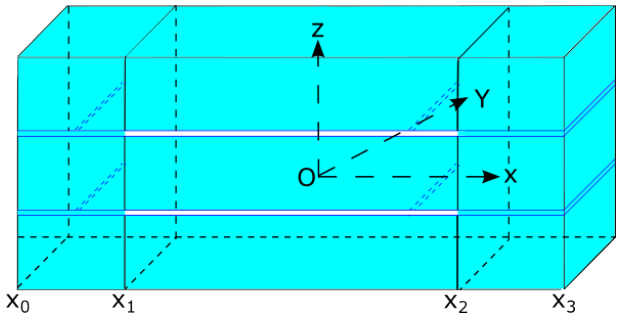

Figure 5.2: Tri-layer structure with an initial perfectly bonded region for $x_0 < x < x_1$, a delaminated region for $x_1 < x < x_2$ and a perfectly bonded region for $x_2 < x < x_3$. We assume that the materials in all layers are identical.

For our study, we will examine the scattering of long longitudinal solitary waves within the waveguides of an n-layered structure, where the bonded and delaminated regions are consistent with those shown in Figures 5.1 and 5.2 across all layers. Here, n denotes the number of layers in the structure. The

displacement of the long longitudinal solitary waves within each layer of the structure are governed by the following regularised non-dimensional Boussinesq equations:

$$u_{tt}^{(i)} - c_i^2 u_{xx}^{(i)} = \varepsilon \left[-12\alpha_i u_x^{(i)} u_{xx}^{(i)} + 2\beta_i u_{ttxx}^{(i)} \right]. \tag{5.1}$$

Here, $i = 1, 3$ denotes the perfectly bonded regions, while $i = 2$ represents the delaminated region. The coefficients α_i and β_i are geometrical parameters, and c_i is the characteristic wave speed. These values could vary between sections, indicating a waveguide with different materials in each section; however, for our analysis, we assume uniform material properties across all sections. The parameter ε denotes the small wave parameter. By differentiating (5.1) with respect to x and setting $u_x^{(i)} = f^{(i)}$, we derive the governing equations for the strain of the long longitudinal solitary waves in the form

$$f_{tt}^{(i)} - c_i^2 f_{xx}^{(i)} = \varepsilon \left[-6\alpha_i \left(f^{(i)} \right)_{xx}^2 + 2\beta_i f_{ttxx}^{(i)} \right]. \tag{5.2}$$

These equations are complemented with continuity conditions, namely continuity of longitudinal displacement

$$u^{(i)}\Big|_{x=x_i} = u^{(i+1)}\Big|_{x=x_i}, \tag{5.3}$$

and continuity of normal stress

$$\sigma^{(i)}|_{x=x_i} = \sigma^{(i+1)}|_{x=x_i}, \tag{5.4}$$

where $\sigma^{(i)}$ is defined by our original equation (5.1) when written in the form

$$u_{tt}^{(i)} = \frac{\mathrm{d}\sigma^{(i)}}{\mathrm{d}x}.$$

We consider $\alpha_i = 1$ for all i, $\beta_{1,3} = 1$ and

$$\beta_2(n, k) = \frac{n^2 + k^2}{n^2(1 + k^2)}, \tag{5.5}$$

where k is determined by the geometry of the layer. Referring to Figure 5.1, and similarly to structures with more layers, the cross-section of each layer has a width of $2a$, and height of $2b/n$, with k defined as $k = b/a$. In our subsequent numerical simulations, we will examine the wave behaviour for various values of n and k.

5.1.1 Weakly-nonlinear solution and initial conditions

We construct a weakly-nonlinear solution for each section of the bar within the outlined n-layered structure, following the approaches used in [47, 48, 77, 93], and resulting in

$$f^{(i)}(x,t) = T^{(i)}(\xi, X) + R^{(i)}(\eta, X) + \varepsilon P^{(i)}(\xi, \eta, X) + \mathcal{O}\left(\varepsilon^2\right), \tag{5.6}$$

where $\xi = x - c_i t$, $\eta = x + c_i t$, and $X = \varepsilon x$. The functions T and R represent the leading order transmitted and reflected waves, respectively, while the function P is the higher-order correction. Note that $T^{(1)}$ represents the incident wave in the first region. By substituting (5.6) into (5.2) and considering terms up to $\mathcal{O}(\varepsilon)$, we find

$$\begin{aligned} -2P^{(i)}_{\xi\eta} = &\left(T^{(i)}_X - 6\frac{\alpha_i}{c_i^2}T^{(i)}T^{(i)}_\xi + \beta_i T^{(i)}_{\xi\xi\xi}\right)_\xi + \left(R^{(i)}_X - 6\frac{\alpha_i}{c_i^2}R^{(i)}R^{(i)}_\eta + \beta_i R^{(i)}_{\eta\eta\eta}\right)_\eta \\ &- 6\alpha_i\left(2T^{(i)}_\xi R^{(i)}_\eta + T^{(i)}R^{(i)}_{\eta\eta} + T^{(i)}_{\xi\xi}R^{(i)}\right). \end{aligned} \tag{5.7}$$

For the first region, where $i = 1$, by assuming that the left boundary of the waveguide tends to negative infinity, we average the left-hand side of equation (5.7) with respect to the fast space variable x, as

$$\lim_{x_0\to-\infty}\frac{1}{x_1 - x_0}\int_{x_0}^{x_1}\ldots \mathrm{d}x. \tag{5.8}$$

Given that all functions and their derivatives are assumed to remain bounded and decay sufficiently rapidly at infinity to avoid secular terms in the asymptotic expansions, at constant ξ, we have

$$\lim_{x_0\to-\infty}\frac{1}{x_1 - x_0}\int_{x_0}^{x_1} P^{(1)}_{\xi\eta}\mathrm{d}x = \lim_{x_0\to-\infty}\frac{1}{2(x_1 - x_0)}\int_{2x_0-\xi}^{2x_1-\xi} P^{(1)}_{\xi\eta}\mathrm{d}\eta = \lim_{x_0\to-\infty}\frac{1}{2(x_1 - x_0)}\left[P^{(1)}_\xi\right]_{2x_0-\xi}^{2x_1-\xi} = 0. \tag{5.9}$$

A similar process is applied at constant η, which also results in the left-hand side of (5.7) tending to 0 after the averaging process has been applied. Now by averaging the right-hand side of (5.7) at both constant ξ and η we yield the following Korteweg-de Vries (KdV) equations

$$T^{(1)}_X - 6\frac{\alpha_1}{c_1^2}T^{(1)}T^{(1)}_\xi + \beta_1 T^{(1)}_{\xi\xi\xi} = 0, \tag{5.10}$$

$$R^{(1)}_X - 6\frac{\alpha_1}{c_1^2}R^{(1)}R^{(1)}_\eta + \beta_1 R^{(1)}_{\eta\eta\eta} = 0, \tag{5.11}$$

and by substituting our KdV equations into (5.7) and rearranging to make $P^{(1)}$ the subject, we obtain the higher-order correction as

$$P^{(1)} = 3\alpha_1 \left(2T^{(1)}R^{(1)} + R^{(1)}_{\eta} \int T^{(1)} \mathrm{d}\xi + T^{(1)}_{\xi} \int R^{(1)} \mathrm{d}\eta \right) + \psi^{(1)}(\xi, X) + \phi^{(1)}(\eta, X), \tag{5.12}$$

where $\psi^{(1)}$ and $\phi^{(1)}$ are arbitrary constants. We apply a similar averaging across the remaining sections, assuming for each that the left boundaries tend to negative infinity. This allows us to express the leading order equations in a general form for all sections as

$$T^{(i)}_X - 6\frac{\alpha_i}{c_i^2} T^{(i)} T^{(i)}_{\xi} + \beta_i T^{(i)}_{\xi\xi\xi} = 0, \tag{5.13}$$

$$R^{(i)}_X - 6\frac{\alpha_i}{c_i^2} R^{(i)} R^{(i)}_{\eta} + \beta_i R^{(i)}_{\eta\eta\eta} = 0, \tag{5.14}$$

and the higher-order correction as

$$P^{(i)} = 3\alpha_i \left(2T^{(i)}R^{(i)} + R^{(i)}_{\eta} \int T^{(i)} \mathrm{d}\xi + T^{(i)}_{\xi} \int R^{(i)} \mathrm{d}\eta \right) + \psi^{(i)}(\xi, X) + \phi^{(i)}(\eta, X). \tag{5.15}$$

To determine the initial conditions, we apply a process similar to that in Chapter 3. For brevity, we will provide a brief overview. By substituting our weakly-nonlinear solution into the continuity conditions (5.3) - (5.4), we derive values for T and R at the interface, expressed in terms of the previous transmitted wave, as

$$R^{(i)}|_{x=x_i} = C^{(i)}_R T^{(i)}|_{x=x_i}, \quad T^{(i+1)}|_{x=x_i} = C^{(i)}_T T^{(i)}|_{x=x_i}, \tag{5.16}$$

where the reflection and transmission coefficients take the form

$$C^{(i)}_R = \frac{c_i - 1}{c_i + 1}, \quad C^{(i)}_T = \frac{2}{c_i\,(1 + c_i)}. \tag{5.17}$$

Given our assumption that the waveguide comprises uniform material (i.e., $c_i = 1$ for all i), we observe full transmission and no reflection. If the value of c_i varies between sections of the bar, $i = 1, 2, 3$, implying the material in a single layer varies across the bar, then the coefficients should be computed using the respective values of c_i. This avenue could be explored in future investigations.

5.1.2 Theoretical prediction from the incident wave

In [45], the wave amplitude for an incident soliton entering a delaminated region was theoretically predicted using the IST. Here, we briefly outline this approach and introduce an initial condition expressed in

terms of the FWHM of the incident soliton, defined as the distance between the points where the wave's amplitude is half of its maximum value. Later in Section 5.3.3, we extend this to consider solitons entering the second bonded region. Similar to Section 3.4.2, we can rewrite the transmitted wave equation (5.13) in the form

$$U_\tau - 6UU_\chi + U_{\chi\chi\chi} = 0, \quad U|_{\tau=0} = U_0(\chi), \tag{5.18}$$

where χ and τ are characteristic variables written in standard IST notation. For a sufficiently rapidly decaying initial condition $U_0(\chi)$ on the infinite line, the solution to (5.18) is related to the spectral problem for the Schrödinger equation given by

$$\Psi_{\chi\chi} + [\lambda - U_0(\chi)]\Psi = 0, \tag{5.19}$$

where λ is the spectral parameter. Determining the evolution of scattering data for both discrete and continuous spectra and using this to reconstruct the solution to the KdV equation is known as the IST method [12]. We assume an incident soliton in the first region, which, being a traveling wave solution, will propagate over time while preserving its shape. To illustrate the theoretical predictions of the wave amplitude, we will examine the second region, where β_2 is defined as in (5.5). The initial condition for (5.18) in the second region then takes the form

$$U_0(\chi) = -A\,\mathrm{sech}^2\left(\frac{\chi}{l}\right), \quad A = \frac{v}{2\beta_2}, \quad l = \frac{2}{\sqrt{v}}, \tag{5.20}$$

where $v > 0$ is the phase speed. In this scenario, the solution will consist of either a single soliton or a series of solitons, characterised by eigenvalues in the discrete spectrum, along with accompanying dispersive radiation determined by the continuous spectrum. In certain instances, we may observe the fission of the initial soliton, where more than one soliton is generated, particularly when $\beta_2 \neq 1$. The discrete eigenvalues of (5.19) are expressed as $\lambda = -k_n^2$, where

$$k_n = \frac{1}{2l}\left[\sqrt{1 + 4Al^2} - (2n-1)\right], \tag{5.21}$$

for $n = 1, 2, \ldots, N_T$, where $N_T \in \mathbb{Z}$ is the number of solitons. The number solitons generated in the delaminated region is determined by the largest integer satisfying the inequality

$$N_T < \frac{1}{2}\left(\sqrt{1 + \frac{8}{\beta_2}} + 1\right). \tag{5.22}$$

From (5.22), we observe that when $\beta_2 = 1$, only one soliton will form, while for $\beta_2 < 1$, multiple solitons will be generated, with more arising as β_2 decreases. This behaviour corresponds to an increase in layers in the waveguide or a change in geometry. As $\tau \to \infty$, the solution evolves into a train of solitary waves, ordered by amplitude, propagating to the right, along with some dispersive radiation (a dispersive wave train) moving to the left in the moving reference frame. Thus, we have

$$U(\chi, \tau) \sim -\sum_{n=1}^{N} 2k_n^2 \text{sech}^2(k_n(\chi - 4k_n^2\tau - \chi_n)) + \text{radiation}, \tag{5.23}$$

where χ_n represents the phase shift. If the delamination is infinite, the solitons will separate in rank order, with the largest soliton at the front. However in our scenario where delamination is finite, separation occurs only if the delamination is large. This will allow us to establish a measure of the delamination length when we evaluate our numerical simulations later in this chapter by comparing the wave amplitude of the leading wave peak at the end of the bar with the theoretical prediction.

We introduce the incident solitary wave for $T^{(1)}$, which is the exact traveling wave solution of (5.13) in the first region of the structure, as

$$T^{(1)}(\xi, X) = -\frac{v}{2}\text{sech}^2\left(\frac{\sqrt{v}}{2}(\xi - vX)\right). \tag{5.24}$$

The soliton peak in (5.24) occurs for the maximum value of $T^{(1)}(\xi, X)$, when $\text{sech}^2(0) = 1$ at $\xi = vX$, therefore, we obtain

$$T^{(1)}(vX, X) = -\frac{v}{2}. \tag{5.25}$$

To find the half-maximum value, we take half of (5.25), and so

$$-\frac{v}{2}\text{sech}^2\left(\frac{\sqrt{v}}{2}(\xi - vX)\right) = -\frac{v}{4}. \tag{5.26}$$

Solitary waves are often measured in experiments using their FWHM. Since $\xi - vX$ is the position relative to the centre of the wave, and due to the symmetry of the wave, the full width corresponds to twice the distance from the centre to the half-maximum value. Therefore, we set $\text{FWHM}/2 = \xi - vX$ and rewrite (5.26) as

$$-\frac{v}{2}\text{sech}^2\left(\frac{\sqrt{v}}{4}\text{FWHM}\right) = -\frac{v}{4}, \tag{5.27}$$

and hence we obtain

$$v = \left(\frac{4}{\text{FWHM}}\cosh^{-1}\left(\sqrt{2}\right)\right)^2. \tag{5.28}$$

This allows us to generalise the FWHM to any size of incident solitary wave.

5.2 Imperfect bonding case

Let's delve into the scenario illustrated in Figure 5.3, of a two-layered structure with an initial homogeneous region, followed by a delaminated region 'sandwiched' between soft bonded regions. The layers are composed of similar materials.

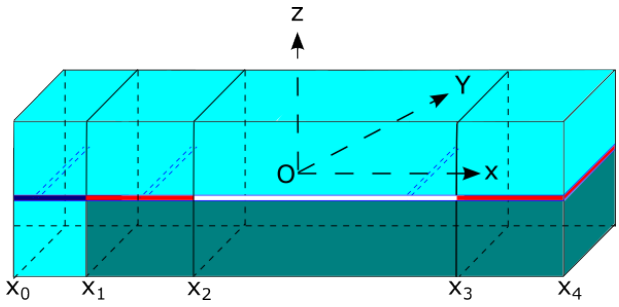

Figure 5.3: Bi-layer structure with an initial homogeneous region for $x_0 < x < x_1$ followed by a delaminated region for $x_2 < x < x_3$ 'sandwiched' by soft bonded regions. We assume that the materials in both layers are similar, that is, their material properties differ by $\mathcal{O}(\varepsilon)$.

The longitudinal displacement in the homogeneous regions is described by the following regularised non-dimensional Boussinesq equations,

$$\begin{aligned} u_{tt}^{(i)} - u_{xx}^{(i)} &= \varepsilon \left[-12 u_x^{(i)} u_{xx}^{(i)} + 2 u_{ttxx}^{(i)} \right], \\ w_{tt}^{(i)} - w_{xx}^{(i)} &= \varepsilon \left[-12 w_x^{(i)} w_{xx}^{(i)} + 2 w_{ttxx}^{(i)} \right], \end{aligned} \tag{5.29}$$

for $i = 1$, while in the bonded regions we have the following coupled regularised Boussinesq (cRB) equations:

$$\begin{aligned} u_{tt}^{(i)} - u_{xx}^{(i)} &= \varepsilon \left[-12 u_x^{(i)} u_{xx}^{(i)} + 2 u_{ttxx}^{(i)} \right] - \varepsilon \delta (u^{(i)} - w^{(i)}), \\ w_{tt}^{(i)} - c^2 w_{xx}^{(i)} &= \varepsilon \left[-12 \alpha w_x^{(i)} w_{xx}^{(i)} + 2 \beta w_{ttxx}^{(i)} \right] + \varepsilon \gamma (u^{(i)} - w^{(i)}), \end{aligned} \tag{5.30}$$

for $i = 2, 4$, and in the delaminated region we have

$$\begin{aligned} u_{tt}^{(i)} - u_{xx}^{(i)} &= \varepsilon \left[-12 u_x^{(i)} u_{xx}^{(i)} + 2 u_{ttxx}^{(i)} \right], \\ w_{tt}^{(i)} - c^2 w_{xx}^{(i)} &= \varepsilon \left[-12 \alpha w_x^{(i)} w_{xx}^{(i)} + 2 \beta w_{ttxx}^{(i)} \right], \end{aligned} \tag{5.31}$$

for $i = 3$. Differentiating the governing equations with respect to x and denoting $u_x^{(i)} = f^{(i)}$, we obtain

the Boussinesq equations for the longitudinal strain in the homogeneous region

$$\begin{aligned} f_{tt}^{(i)} - f_{xx}^{(i)} &= \varepsilon \left[-6 \left(f^{(i)} \right)_{xx}^2 + 2 f_{ttxx}^{(i)} \right], \\ g_{tt}^{(i)} - g_{xx}^{(i)} &= \varepsilon \left[-6 \left(g^{(i)} \right)_{xx}^2 + 2 g_{ttxx}^{(i)} \right], \end{aligned} \tag{5.32}$$

for $i = 1$, while in the soft bonded regions we have

$$\begin{aligned} f_{tt}^{(i)} - f_{xx}^{(i)} &= \varepsilon \left[-6 \left(f^{(i)} \right)_{xx}^2 + 2 f_{ttxx}^{(i)} \right] - \varepsilon \delta (f^{(i)} - g^{(i)}), \\ g_{tt}^{(i)} - c^2 g_{xx}^{(i)} &= \varepsilon \left[-6\alpha \left(g^{(i)} \right)_{xx}^2 + 2\beta g_{ttxx}^{(i)} \right] + \varepsilon \gamma (f^{(i)} - g^{(i)}), \end{aligned} \tag{5.33}$$

for $i = 2, 4$, and in the delaminated regions we have

$$\begin{aligned} f_{tt}^{(i)} - f_{xx}^{(i)} &= \varepsilon \left[-6 \left(f^{(i)} \right)_{xx}^2 + 2 f_{ttxx}^{(i)} \right], \\ g_{tt}^{(i)} - c^2 g_{xx}^{(i)} &= \varepsilon \left[-6\alpha \left(g^{(i)} \right)_{xx}^2 + 2\beta g_{ttxx}^{(i)} \right], \end{aligned} \tag{5.34}$$

for $i = 3$. As with the perfectly bonded case, these equations are complemented with continuity conditions at the interfaces between the sections. We have the continuity of longitudinal displacement

$$u^{(i)}|_{x=x_i} = u^{(i+1)}|_{x=x_i}, \quad w^{(i)}|_{x=x_i} = w^{(i+1)}|_{x=x_i}, \tag{5.35}$$

and the continuity of normal stress

$$\sigma_u^{(i)}|_{x=x_i} = \sigma_u^{(i+1)}|_{x=x_i}, \quad \sigma_w^{(i)}|_{x=x_i} = \sigma_w^{(i+1)}|_{x=x_i}, \tag{5.36}$$

for $i = \{1, 2, 3\}$, where σ_u and σ_w are implicitly defined by (5.30) as

$$\begin{aligned} u_{tt}^{(i)} &= \frac{\mathrm{d}\sigma_u^{(i)}}{\mathrm{d}x} - \varepsilon \delta (u^{(i)} - w^{(i)}), \\ w_{tt}^{(i)} &= \frac{\mathrm{d}\sigma_w^{(i)}}{\mathrm{d}x} + \varepsilon \gamma (u^{(i)} - w^{(i)}), \end{aligned} \tag{5.37}$$

respectively. We'll focus solely on deriving the leading order solutions for the soft bonded region since the homogeneous and delaminated cases addressed in Sections 4.2.1 and 4.2.3, respectively, involve the same derivation, despite the characteristic speed in the lower layer being different in the delaminated region in this scenario. Here, since the materials in the layers have similar properties, we have $c - 1 = \mathcal{O}(\varepsilon)$. In this

scenario, the cRB equations provide solutions in the form of radiating solitary waves. Thus, we note that

$$c-1=O(\varepsilon) \quad \Rightarrow \quad \frac{c^2-1}{\varepsilon}=\mathcal{O}(1), \tag{5.38}$$

which is also observed in [48]. Using (5.38) we can rearrange equation (5.33) to obtain

$$g_{tt}^{(i)}-g_{xx}^{(i)}=\varepsilon\left[-6\alpha(g^{(i)})^2+2\beta g_{tt}^{(i)}+\frac{c^2-1}{\varepsilon}g^{(i)}\right]_{xx}+\varepsilon\gamma\left(f^{(i)}-g^{(i)}\right). \tag{5.39}$$

Therefore, unlike in Section 4.2.2, we can use a single set of characteristic variables to construct the weakly-nonlinear solutions to (5.33), which are described as

$$f^{(2)}(x,t)=T^{(2)}(\xi,X)+R^{(2)}(\eta,X)+\varepsilon P^{(2)}(\xi,\eta,X)+O(\varepsilon^2), \tag{5.40}$$

$$g^{(2)}(x,t)=S^{(2)}(\xi,X)+G^{(2)}(\eta,X)+\varepsilon Q^{(2)}(\xi,\eta,X)+O(\varepsilon^2), \tag{5.41}$$

respectively. The characteristic variables are defined as $\xi=x-t$, $\eta=x+t$, and $X=\varepsilon x$. In the second section, $T^{(2)}$ and $S^{(2)}$ denote the transmitted waves, while $R^{(2)}$ and $G^{(2)}$ represent the reflected waves, in the upper and lower layers, respectively. The higher-order corrections are denoted by $P^{(2)}$ and $Q^{(2)}$ for the upper and lower layers, respectively. We substitute (5.40) and its corresponding derivatives into the upper layer equation in (5.33) with $i=2$, while only considering terms up to $\mathcal{O}(\varepsilon)$. This yields

$$\begin{aligned}-4P_{\xi\eta}^{(2)}=&\left(2T_{\xi X}^{(2)}-12(T^{(2)}T_{\xi}^{(2)})_{\xi}+2T_{\xi\xi\xi\xi}^{(2)}\right)-\delta\left(T^{(2)}-S^{(2)}\right)\\&+\left(2R_{\eta X}^{(2)}-12(R^{(2)}R_{\eta}^{(2)})_{\eta}+2R_{\eta\eta\eta\eta}^{(2)}\right)-\delta\left(R^{(2)}-G^{(2)}\right)\\&-12\left(T_{\xi\xi}^{(2)}R^{(2)}+T^{(2)}R_{\eta\eta}^{(2)}+2T_{\xi}^{(2)}R_{\eta}^{(2)}\right).\end{aligned} \tag{5.42}$$

Similarly, substituting (5.41) and its respective derivatives into the lower layer equation in (5.39), while also considering terms up to $\mathcal{O}(\varepsilon)$, gives

$$\begin{aligned}-4Q_{\xi\eta}^{(2)}=&\left(2S_{\xi X}^{(2)}+\frac{c^2-1}{\varepsilon}S_{\xi}^{(2)}-12\alpha(S^{(2)}S_{\xi}^{(2)})_{\xi}+2\beta S_{\xi\xi\xi\xi}^{(2)}\right)+\gamma\left(T^{(2)}-S^{(2)}\right)\\&+\left(2G_{\eta X}^{(2)}+\frac{c^2-1}{\varepsilon}G_{\eta}^{(2)}-12\alpha(G^{(2)}G_{\eta}^{(2)})_{\eta}+2\beta G_{\eta\eta\eta\eta}^{(2)}\right)+\gamma\left(R^{(2)}-G^{(2)}\right)\\&-12\alpha\left(S_{\xi\xi}^{(2)}G^{(2)}+S^{(2)}G_{\eta\eta}^{(2)}+2S_{\xi}^{(2)}G_{\eta}^{(2)}\right).\end{aligned} \tag{5.43}$$

As the solution is analysed from the moment the waves enter the region at $x=x_1$ until the reflected waves from $x=x_2$ return to $x=x_1$, and because $x=x_2$ is assumed to be sufficiently distant, we consider

the averaging

$$\lim_{x_2\to-\infty}\frac{1}{x_2-x_1}\int_{x_1}^{x_2}\ldots\mathrm{d}x. \tag{5.44}$$

Similarly to the approach in Sections 3.2 and 4.2, we apply averaging by integrating (5.42) with respect to x while keeping ξ constant, and we apply the same procedure to (5.43), which yields the coupled Ostrovsky equations

$$\left(T_X^{(2)}-6T^{(2)}T_\xi^{(2)}+T_{\xi\xi\xi}^{(2)}\right)_\xi=\frac{\delta}{2}\left(T^{(2)}-R^{(2)}\right), \tag{5.45}$$

$$\left(S_X^{(2)}+\frac{c^2-1}{2\varepsilon}S_\xi^{(2)}-6\alpha S^{(2)}S_\xi^{(2)}+\beta S_{\xi\xi\xi}^{(2)}\right)_\xi=\frac{\gamma}{2}\left(S^{(2)}-G^{(2)}\right). \tag{5.46}$$

Similarly, applying averaging to (5.43) and (5.43) while fixing constant η gives

$$\left(R_X^{(2)}-6R^{(2)}R_\eta^{(2)}+R_{\eta\eta\eta}^{(2)}\right)_\eta=\frac{\delta}{2}\left(R^{(2)}-T^{(2)}\right), \tag{5.47}$$

$$\left(G_X^{(2)}+\frac{c^2-1}{2\varepsilon}G_\eta^{(2)}-6\alpha G^{(2)}G_\eta^{(2)}+\beta G_{\eta\eta\eta}^{(2)}\right)_\eta=\frac{\gamma}{2}\left(G^{(2)}-S^{(2)}\right), \tag{5.48}$$

aligning with the findings from the time-averaged derivation in [72]. Coupled Ostrovsky equations commonly arise in the modeling of nonlinear waves in layered waveguides, in both solid and fluid media [48,74]. By substituting (5.45) and (5.47) into (5.42) and integrating with respect to the characteristic variables, we obtain

$$P^{(2)}=3\left(2T^{(2)}R^{(2)}+R_\eta^{(2)}\int T^{(2)}\mathrm{d}\xi+T_\xi^{(2)}\int R^{(2)}\mathrm{d}\eta\right)+\phi_1^{(2)}(\xi,X)+\psi_1^{(2)}(\eta,X), \tag{5.49}$$

where $\phi_1^{(2)}$ and $\psi_1^{(2)}$ are arbitrary functions. Likewise, by substituting (5.46) and (5.48) into (5.43) and integrating with respect to the characteristic variables, we find

$$Q^{(2)}=3\alpha\left(2S^{(2)}G^{(2)}+G_\eta^{(2)}\int S^{(2)}\mathrm{d}\xi+S_\xi^{(2)}\int G^{(2)}\mathrm{d}\eta\right)+\psi_2^{(2)}(\xi,X)+\phi_2^{(2)}(\eta,X), \tag{5.50}$$

where $\psi^{(2)}$ and $\phi_2^{(2)}$ are arbitrary functions. To establish our initial conditions, we use a methodology similar to that discussed for the perfectly bonded case in Section 5.1.1, so we will omit the details here.

Since the coupled Ostrovsky equations cannot be solved using the IST, theoretical predictions of the wave amplitude in the soft bonded region are not possible. Consequently, we will rely solely on the wave amplitudes from the numerical simulations to detect delamination in this scenario.

To relate the initial condition to the incident soliton's FWHM, we first consider (5.31), leading to the

strain solitary wave in the delaminated section of the structure taking the form

$$w_x(x,0) = -\frac{(v^2-c^2)}{4\alpha\varepsilon}\text{sech}^2\left(\frac{\sqrt{v^2-c^2}}{2v\sqrt{2\varepsilon\beta}}(x+x_0)\right). \tag{5.51}$$

Integrating $w_x(x,0)$ with respect to x gives the initial condition for w as

$$w(x,0) = -\frac{v\sqrt{2\varepsilon\beta}\sqrt{v^2-c^2}}{2\alpha\varepsilon}\left[\tanh\left(\frac{\sqrt{v^2-c^2}}{2v\sqrt{2\varepsilon\beta}}(x+x_0)\right)-1\right], \tag{5.52}$$

where the constant of integration is chosen so that the waves are propagating into an unperturbed medium. We study the effect of varying the FWHM of the incident soliton on wave amplitude for different delamination lengths. To establish a correspondence between the initial condition and the soliton's FWHM, we use (5.51) to solve

$$-\frac{(v^2-c^2)}{4\alpha\varepsilon}\text{sech}^2\left(\frac{\sqrt{v^2-c^2}}{2v\sqrt{2\varepsilon\beta}}(x+x_0)\right) = -\frac{(v^2-c^2)}{8\alpha\varepsilon}, \tag{5.53}$$

for the phase speed, v, which yields

$$v = \sqrt{-\frac{c^2\text{FWHM}^2}{32\beta\text{arccosh}(\sqrt{2})^2-\text{FWHM}^2}}. \tag{5.54}$$

5.3 Numerical results

For our numerical study, we will first present the scattering of transmitted solitons for various delamination lengths in both the perfectly bonded and soft bonded cases in Section 5.3.2. Next, for the perfectly bonded case in Section 5.3.3, we will introduce a measure, σ, based on wave amplitudes in different sections of the structure from our simulations and the IST. This measure is compared against various delamination lengths and FWHM values to identify correlations between σ and the delamination length, aiding in the detection of delamination. For the soft bonded case in Section 5.3.4, we apply a similar process. However, since the IST cannot be used in the soft bonded region, we base our measure, ζ, solely on the wave amplitudes in different regions. For both the perfectly and soft bonded cases, we scale the measures σ and ζ for incident waves of different FWHM to a reference incident wave of a single FWHM value. This scaling reduces the computational effort by allowing us to calculate results for different FWHM values from a single reference case.

5.3.1 Numerical methods

We will apply the finite difference scheme from Appendix A, following the approach in [77], to solve our systems of Boussinesq equations. Additionally, a semi-analytical method will be employed based on a pseudospectral scheme applied to the KdV equations in the perfectly bonded case (Appendix B.1) and to the coupled Ostrovsky equations in the soft bonded case (Appendix B.3). For all simulations, the grid spacing and time step for the finite difference scheme are set to $\Delta x = 0.01$ and $\Delta t = 0.01$, respectively. For the semi-analytical method, we use $\Delta X = 5 \times 10^{-4}$ and $\Delta \xi = 0.1$.

5.3.2 Examples of scattering

Firstly, let's examine the impact of delamination on the scattering of an incident solitary wave for the perfectly bonded case described in Section 5.1. Figure 5.4(a)-(d) shows the scattering near the end of the bar for simulations on a spatial domain, $x \in [-100, 1000]$, with the delamination starting at $x = 0$ and varying in length across three cases: $D = 0$, $D = 50$, and $D = 300$. The figure also includes a comparison between the semi-analytical and finite difference methods for $D = 300$.

In Figure 5.4(a), without delamination, the soliton propagates without any change in shape or structure. However, when delamination is introduced, as shown in Figures 5.4(b) and 5.4(c), the soliton evolves differently. For $D = 50$, the second soliton starts to form but is still partially obscured by significant radiation. By $D = 300$, the second soliton is much clearer and more distinct from the radiation. Figure 5.4(d) demonstrates a reasonable agreement between the direct numerical simulation and the semi-analytical method for $D = 300$, with only minor discrepancies in their positions along the x coordinate and slight differences in amplitude. These discrepancies should reduce for smaller values of ε, although this would also result in less wave evolution.

As with the perfectly bonded case, we examine wave propagation in a soft bonded structure. The spatial domain, $x \in [-500, 1000]$, featuring a homogeneous section for $x \in [-500, -400]$ to generate an incident soliton in both layers. The first soft bonded region is for $x \in [-400, 0]$, with delamination at $x \in [0, D]$ and the second soft bonded region is for $x \in [D, 1000]$. We present three scenarios: no delamination, a shorter delamination with $D = 100$, and a longer delamination with $D = 300$.

The wave scattering for the soft bonded case in the upper layer is shown in Figure 5.4(e)-(h). The waves in the lower layer exhibit similar behaviour; therefore, a depiction of them is not presented. For the case without delamination, Figure 5.4(e), a solitary wave with a one-sided oscillatory tail, known as a radiating solitary wave, is observed. Details on radiating solitary waves are outlined in Section 2.3.4. As the delamination length increases the solitary wave loses amplitude and sheds energy into its tail

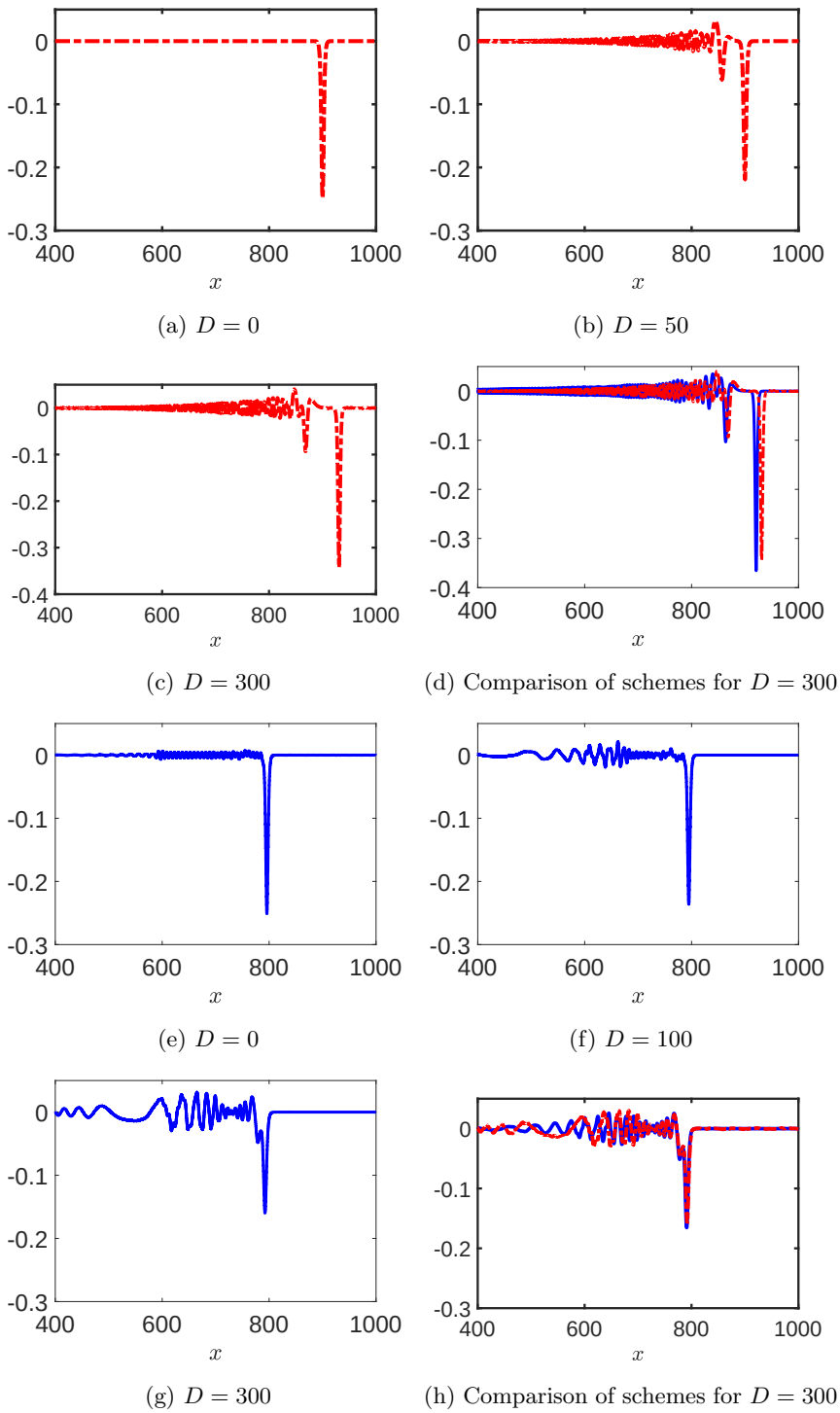

(a) $D = 0$ (b) $D = 50$

(c) $D = 300$ (d) Comparison of schemes for $D = 300$

(e) $D = 0$ (f) $D = 100$

(g) $D = 300$ (h) Comparison of schemes for $D = 300$

Figure 5.4: The waves in the final section of the structure in any layer for the perfectly bonded cases (a) - (d) at $t = 900$ and in the upper layer for the soft bonded cases (e) - (h) at $t = 1200$, shown for various delamination lengths, and calculated via the direct numerical method (blue solid line, $f^{(4)}$) and the semi-analytical method (red dotted line, $T^{(4)}$). For the perfectly bonded case, the parameters are $\varepsilon = 0.1$, FWHM $= 5.0$, $n = 2$, and $k = 2$, with a computational domain of $x \in [-100, 1000]$, and the pseudospectral method using $N = 32,768$ points. For the soft bonded case, parameters are $\varepsilon = 0.05$, FWHM $= 5.0$, $c = 1.025$, $\alpha = \beta = 1.05$, $\delta = \gamma = 1$, and $N = 65,536$ with $x \in [-500, 1000]$.

due to energy exchange between the layers, as shown in Figures 5.4(f) and 5.4(g). These changes serve as indicators of delamination, where we can use the amplitude decay to provide us a measure of the delamination length. Figure 5.4(h) shows excellent agreement between the two numerical schemes at the leading wave peak, similar to the perfectly bonded case, though the agreement diminishes further from the peak, which could be improved with higher-order corrections.

Figure 5.5 builds upon the simulations shown in Figure 5.4 by illustrating wave scattering in the final perfectly bonded region for different values of n and k. As these values increase, there is a noticeable rise in background radiation and the appearance of secondary solitons. This behaviour aligns with previous expectations, as a decrease in β_2 in (5.5) leads to the generation of more solitons.

5.3.3 Measure of delamination length for perfect bonding

We will extend the observations from the previous section by introducing a measure, σ, based on the amplitudes of the leading solitons in the perfectly bonded regions and the theoretical wave amplitude predictions from the IST method, as outlined in Section 5.1.2. We aim to calculate σ for various delamination lengths to identify a correlation, that could be used to help detect delamination based on the σ value. This approach assumes that the solitons are well separated from any background radiation, with greater separation observed for larger delamination lengths. We will then generalise the σ value for different FWHM values. Firstly, we consider

$$A_3 = A_1 k_2^2 k_3^2, \quad k_2 = \frac{1}{2}\left(\sqrt{1+\frac{8}{\beta_2}}-1\right), \quad k_3 = \frac{1}{2}\left(\sqrt{1+8\beta_2}-1\right), \tag{5.55}$$

where A_1 is the amplitude of the incident soliton, and A_3 is the amplitude of the leading soliton in the second bonded region, as predicted by the IST. The eigenvalues k_2 and k_3 are related to the leading soliton amplitudes in the second and third regions, respectively. The leading soliton's amplitude in the second bonded region from the numerical simulation is expressed as A_{num}. Using these amplitudes, we now introduce the measure σ as

$$\sigma = \frac{A_{\text{num}} - A_1}{A_3 - A_1} \times 100. \tag{5.56}$$

This formula is the same as the one used in [77], where only FWHM = 5 was considered. We extend our analysis to a range of delamination lengths expressed in terms of FWHM, rather than nondimensional units D, to explore delamination curves for different FWHM values.

In Figure 5.6, we observe that at $D = 0$, $\sigma = 0$. This is consistent with Figure 5.4(a), where a delamination length of $D = 0$ shows that the wave remains in the same form as the incident wave, and therefore, the amplitude is unaffected. As the delamination length increases, so does σ, for all

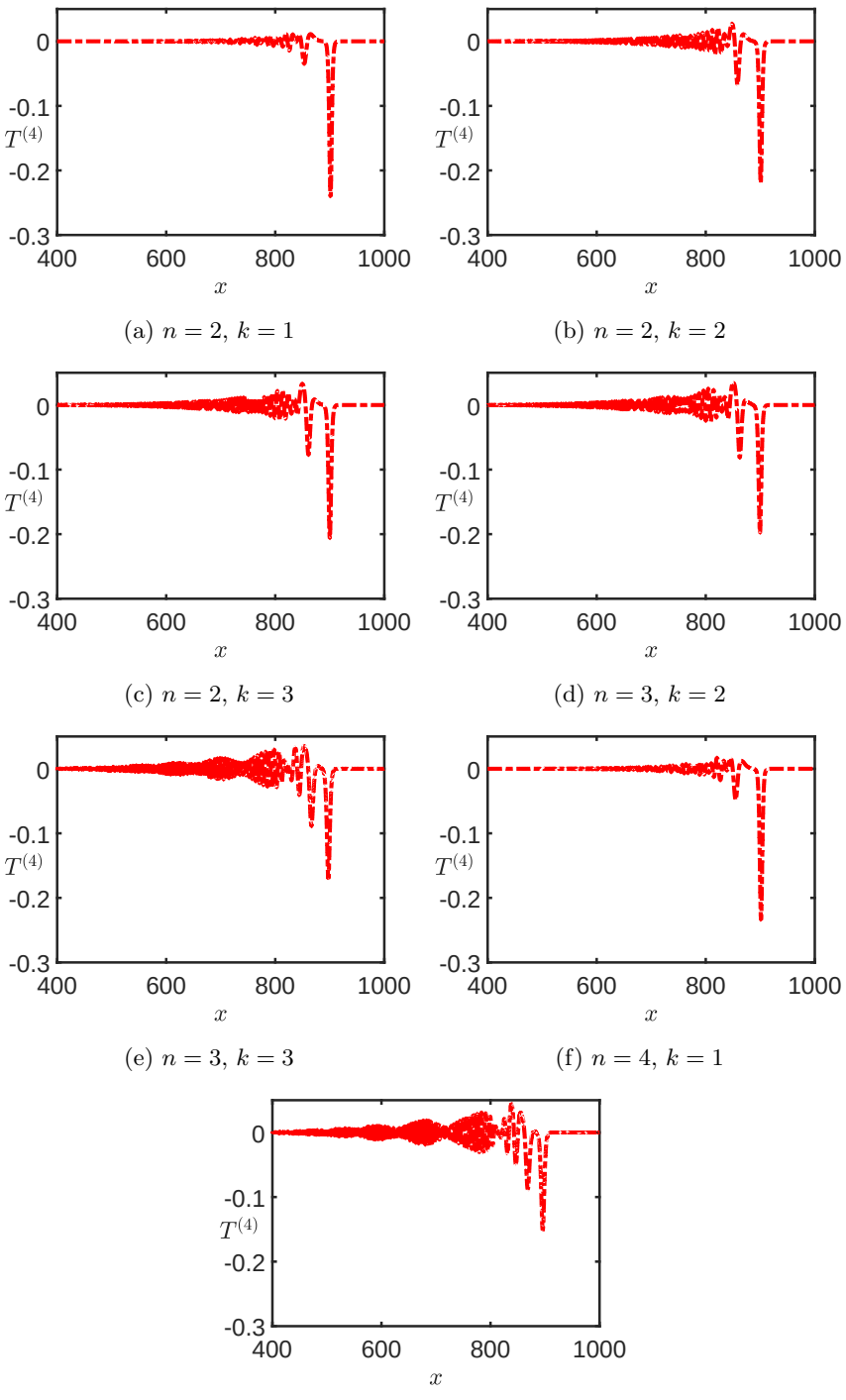

(a) $n = 2$, $k = 1$

(b) $n = 2$, $k = 2$

(c) $n = 2$, $k = 3$

(d) $n = 3$, $k = 2$

(e) $n = 3$, $k = 3$

(f) $n = 4$, $k = 1$

(g) $n = 4$, $k = 3$

Figure 5.5: The waves at $t = 900$ in the final section of the bar for the perfectly bonded case are shown for a delamination length of $D = 60$ using semi-analytical simulations, for a computational domain $x \in [-100, 1000]$. The parameters are $\varepsilon = 0.1$, FWHM $= 5.0$, and $N = 131,072$.

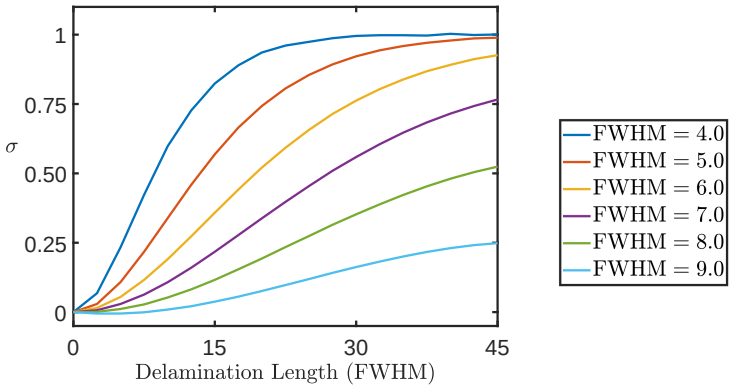

Figure 5.6: Plot of σ against delamination length from 0 to 45, in terms of FWHM, for various FWHM values. Parameters used are $\varepsilon = 0.1$, $n = 2$, and $k = 2$.

FWHM values. For smaller FWHM values, such as FWHM $= \{4, 5\}$, σ tends to converge towards 1. For FWHM $= \{6, 7, 8, 9\}$, σ appears likely to approach 1 if larger delamination lengths were considered. To address the limitation of insufficient delamination lengths, we extend our study to include larger delamination lengths and various n and k values, as shown in Figure 5.7. This extended analysis focuses on smaller FWHM values, which have already shown a tendency to converge to 1, allowing for more insight than the larger FWHM values. We observe similar results as shown in Figure 5.6, but now for FWHM values in the range $[4, 7]$ with increments of 0.5 across all n and k cases.

To generalise this approach, we use (5.28), which relates the phase speed v to the FWHM, where v is inversely proportional to the square of FWHM. By using FWHM $= 5$ as a reference, because it is the last curve to reach $\sigma = 1$ within the given delamination range, we express σ as a function of delamination length parametrised by FWHM, and introduce the scaling

$$\tilde{\sigma}(D; \text{FWHM}) = \frac{\text{FWHM}^2}{25}\sigma(D; \text{FWHM}). \tag{5.57}$$

The plots in Figure 5.8 show the scaled cases of Figure 5.7, derived using (5.57), for varying delamination lengths, and for $n = 3$, $k = 3$ and $n = 4$, $k = 3$. The scaled plots overlap for all FWHM curves, although for larger FWHM values, the curves stop earlier within the delamination length range. With longer delamination lengths, the alignment would continue further. Consequently, by computing only the curve for the smallest FWHM, which extends the furthest, we can replicate the subsequent curves for any other FWHM value through scaling. This approach improves experimental efficiency of our simulations for incident waves of different widths.

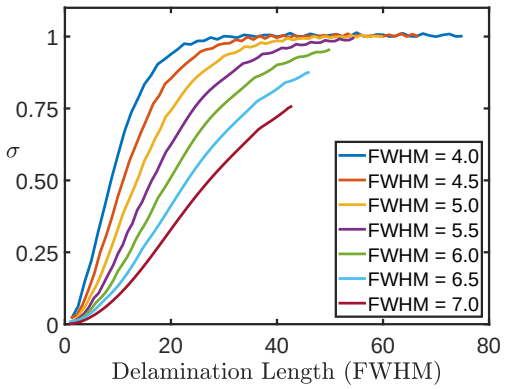

(a) Delamination measure for $n = 2$, $k = 3$.

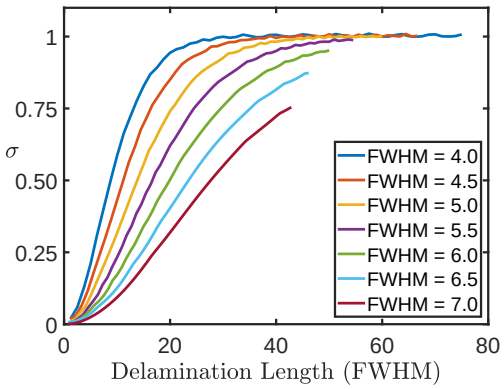

(b) Delamination measure for $n = 3$, $k = 2$.

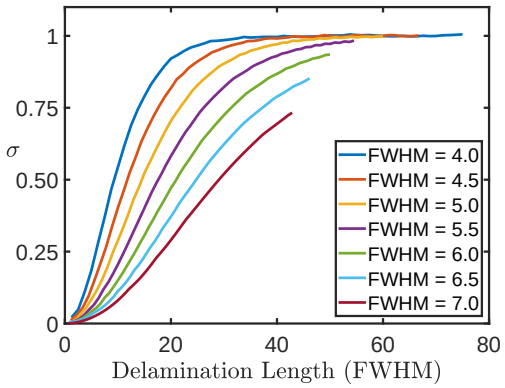

(c) Delamination measure for $n = 3$, $k = 3$.

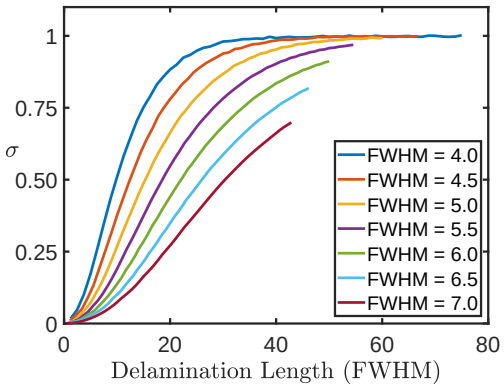

(d) Delamination measure for $n = 4$, $k = 3$.

Figure 5.7: Plots of σ against delamination lengths from 0 to 80 in terms of FWHM, for various FWHM, n, and k values, with $\varepsilon = 1$.

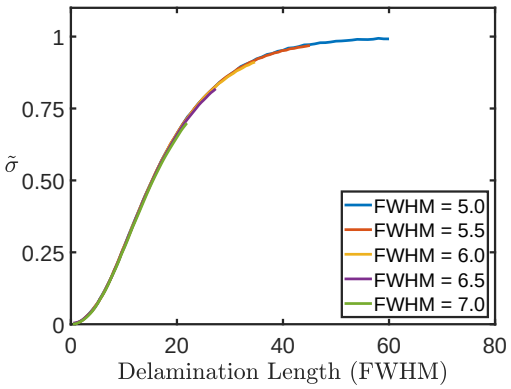

(a) Scaled delamination curve $n = 3$, $k = 3$.

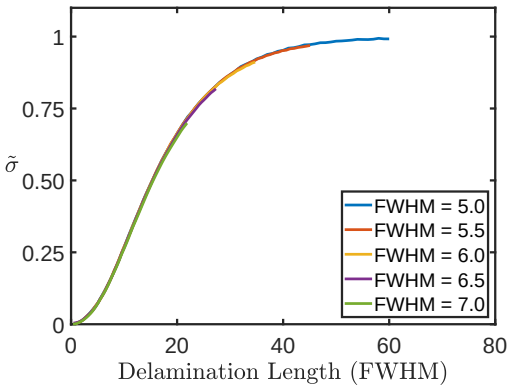

(b) Scaled delamination curve $n = 4$, $k = 3$.

Figure 5.8: Plots of the scaled data from Figure 5.7 for $n = 3$, $k = 3$ and $n = 4$, $k = 3$, with the scaling given by (5.57).

5.3.4 Measure of delamination length for soft bonding

We now turn to the soft bonded case discussed in Section 5.2. The analysis in [48] considered only a single value of FWHM, whereas our study will extend to a broad range of FWHM values using the finite difference scheme outlined in Appendix A. In this case, the IST cannot be applied to predict wave amplitudes in the bonded regions due to the non-integrability of the coupled Ostrovsky equations.

We define the amplitude in each region from the numerical simulation as A_i, where i indicates the region index. We introduce the measure

$$\zeta = \frac{|A_1 - A_3|}{A_1} \times 100, \tag{5.58}$$

which quantifies the change in amplitude between the two soft bonded regions. This measure, ζ, will be analysed to assess whether it correlates with the delamination length, potentially providing an additional metric for delamination detection.

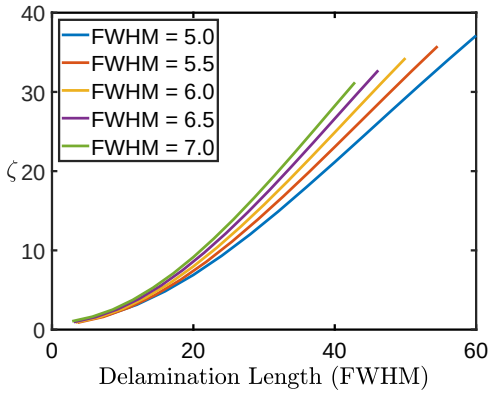

Figure 5.9: Plot of ζ against delamination lengths, from 0 to 60 in terms of FWHM, for the upper layer of the structure in Figure 5.3. The curves correspond to different FWHM values, with parameters $\varepsilon = 0.05$, $\delta = \gamma = 1$.

Figure 5.9 shows ζ for various FWHM values, computed for the upper layer of the structure in Figure 5.3, for various delamination lengths. Generally, as the delamination length increases, the ζ value also increases. Similar behaviour is observed for the lower layer, but those results are omitted for brevity.

Following a similar approach to the perfectly bonded case, we aim to scale the curves for different FWHM values so that they overlap with a chosen reference curve. This would allow us to reproduce all other curves using the data from just that single reference curve. Unlike the perfect bonding scenario, where σ decreases with increasing FWHM, in this case, ζ increases as FWHM grows. Given this trend,

and selecting FWHM = 5 as a reference value, we propose a scaling of the form

$$\tilde{\zeta} = \frac{\zeta}{p + q\,\overline{\text{FWHM}} + r\,\overline{\text{FWHM}}^2}, \quad p + q + r = 1, \tag{5.59}$$

where

$$\overline{\text{FWHM}} = \frac{\text{FWHM}}{5} \tag{5.60}$$

and p, q, and r are constants. Notably, setting $p = q = 0$ and $r = 1$ aligns with the inverse of the scaling utilised in (5.57) for the perfectly bonded scenario. However, this choice fails to give a good fit in the soft bonded case. To address this, we generalise the scaling to encompass any quadratic expression in $\overline{\text{FWHM}}$, with coefficients subject to a normalisation constraint $p+q+r = 1$. The outcomes for $p = 0.49$, $q = 0.28$, and $r = 0.23$ are depicted in Figure 5.10.

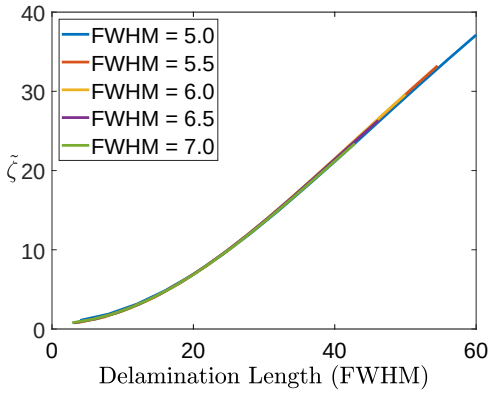

Figure 5.10: Plots of the scaled data from Figure 5.9, with the scaling given by (5.59) with $p = 0.49$, $q = 0.28$, and $r = 0.23$.

Figure 5.10 shows excellent alignment across all FWHM values up to a delamination length of 40 FWHM, after which it begins to deteriorate slightly but remains generally satisfactory. This fitting process is based on trial and error rather than a theoretical prediction, as in the perfectly bonded case. Although there is potential to find a more precise fit using advanced nonlinear optimisation techniques, a task that extends beyond the scope of this thesis, we have established a workable solution.

5.3.5 Material parameters

In Figure 5.10, we observe excellent agreement between the various FWHM cases of $\tilde{\zeta}$ up to 40 units of FWHM, after which the agreement begins to deteriorate slightly, corresponding to a minimum of

200 in nondimensional units. Therefore we use the scaling to transform our nondimensional variables into dimensional material parameters, allowing us to compare experimental data to confirm whether a delamination length of 200 is reasonable.

Referring to the dimensional form of the DDE in (2.14), we transition the scaling to nondimensional form via

$$\tilde{x} = \frac{x}{X}, \quad \tilde{f} = \frac{f}{F}, \quad \tilde{t} = \frac{t}{T}, \tag{5.61}$$

where

$$X = \sqrt{\frac{J\nu^2}{2\varepsilon\sigma c^2}\,(c^2 - c_1^2)}, \quad T = \frac{X}{c}, \quad F = -\frac{12\varepsilon c^2\rho}{\beta}X. \tag{5.62}$$

We can determine the corresponding material length from the nondimensional length. Considering the PMMA bar and parameters outlined in Table 3.5, also stated in [46], we find that for $\varepsilon = 0.1$, a delamination length of $x = 200$ in nondimensional units corresponds to a dimensional delamination of approximately $x = 520$ mm. This length is significant considering that experimental materials are typically around 600 mm long in total. Hence, it is reasonable to confine our considerations to delamination values less than 200 nondimensional units in the context of practical applications.

5.4 Summary

This chapter builds upon the methodologies introduced in Chapters 3 and 4, where we examined the scattering of a bulk strain solitary wave in a delaminated bi-layer structure with perfect bonding between the layers, as well as the behaviour of radiating solitary waves in a similar structure with soft bonding. The longitudinal displacements are described by either Boussinesq equations (for perfectly bonded, homogeneous or delaminated sections) or coupled Boussinesq equations (for soft bonded sections), with continuity conditions imposed on the interface. In both cases, we developed a weakly-nonlinear solution and derived corresponding initial conditions. Incident solitary waves undergo fission upon entering delaminated regions in both perfect and soft bonded structures, providing a clear indicator of delamination.

We develop theoretical estimates for the soliton amplitudes after propagating through a delaminated region by employing the IST to analyse the transmitted waves. Wave scattering behaviours in both bonding scenarios were examined across various delamination lengths and geometric configurations, revealing a correlation between these parameters and the observed number of solitons.

A measure, σ, is used leveraging both theoretical and observed data of the wave's amplitude to estimate the delamination length. This measure is extended to accommodate incident waves of varying FWHM.

A quadratic scaling is used to align all delamination curves to a single reference curve. This shows that the curves overlap, allowing us to compute just one curve and apply the scaling to get the results for the others. This approach significantly reduces computational time and enables efficient exploration of incident waves of various widths.

For the soft bonded structure, theoretical estimates are unavailable through the IST. Instead, we use the wave amplitudes in the first and second soft bonded regions from the numerical simulation to create our measure ζ. A quadratic scaling is identified, showing mostly strong agreement and is consistent across both layers of the structure.

Expanding on the findings of this chapter, the accuracy of the semi-analytical scheme could be enhanced by implementing higher-order corrections. Involving higher-order corrections would increase the potential to yield even more precise results than those obtained at leading order. Further details on this will be provided in Chapter 6.

Chapter 6

Conclusion

6.1 Overview

In this thesis, we investigated the scattering of long longitudinal bulk strain waves in multiple layered structures with varying bonding types between the layers. Since our goal was to detect delamination, we developed and used numerical techniques for each structure to analyse the wave's amplitude, speed, and position in both bonded and delaminated regions. Previous studies have explored delamination detection methods for two-layered structures [47, 48]. Building on this work, our research applied new detection methods to both previously and newly studied structures.

In Chapter 3, we examined a two-layered structure featuring an initial delaminated region to generate a solitary wave, followed by a second delaminated region sandwiched between two soft bonded regions - a structure similar to that used in the experimental study [46]. We constructed weakly-nonlinear solutions and obtained equations describing left and right propagating waves to leading order, with corresponding initial and continuity conditions, by using a similar methodology to previous work [29, 45]. We then used the numerical schemes presented in Appendices A and B to perform 'base case' simulations for a scenario with infinite delamination in the structure, finding excellent agreement between the two numerical schemes. In the soft bonded region, the leading peak evolved into an Ostrovsky wave packet, while in the delaminated region, it evolved into a solitary wave followed by secondary solitons and radiation. By applying the Inverse Scattering Transform (IST) to the Korteweg-de Vries (KdV) equation and using the linear dispersion relations for the Ostrovsky and Boussinesq equations, we derived theoretical predictions for the leading wave peak amplitude and wave speed, both of which showed excellent agreement with the simulations. By varying parameters such as ε and δ, we further validated the theoretical predictions, finding consistent agreement with the simulations. In the case of finite delamination, the wave in the second

soft bonded region evolved into an Ostrovsky wave packet once again. We then varied the delamination length from $D = 0$ to $D = 300$ and calculated the difference in wave amplitude and phase shift relative to the $D = 0$ case for $\varepsilon = 0.001$ and $\varepsilon = 0.005$. As the delamination length increased, the amplitude decreased mostly linearly for smaller ε and nonlinearly for larger ε. The phase shift increased with delamination length for smaller ε, and for larger ε, it also increased linearly but more significantly following an initial nonlinear behaviour at smaller delamination lengths. These results show that amplitude and phase shift can be used to identify the delamination length without prior knowledge of its value, thus addressing the research project's objective. Using experimental parameters from [100] for waveguide properties and geometry, we ran a simulation and observed an Ostrovsky wave packet in the soft bonded region and solitons in the delaminated region, though not fully separated due to the bar's shortened length. This simulation provides insights into expected real-world outcomes.

In Chapter 4, we extended the analysis from Chapter 3 by considering the lower layer of the structure to have a characteristic speed difference of $c - 1 = \mathcal{O}(1)$, where the upper layer has a unit wave speed. In a similar approach to Chapter 3, we outlined equations for the longitudinal displacement and strain, along with continuity conditions. We developed a weakly-nonlinear solution and derived equations for the leading order left- and right- propagating waves, along with their respective initial conditions, and outlined the numerical methods. In our 'base case' simulation for a structure with infinite delamination, the wave propagation in the upper layer was similar to that observed in Chapter 3. The only difference was a slightly smaller ε value was used, which resulted in a reduction in wave evolution. The waves in the lower layer evolved less than those in the upper layer, due to its higher wave speed. Similar effects were observed in the second soft bonded region for the finite delamination case. We varied the characteristic wave speed, c, in the base case simulation and compared it with theoretical predictions derived from the linear dispersion relation, finding good agreement between the two. To enhance our understanding of delamination detection, we varied the delamination position from $x_2 = 0$ to $x_2 = 1500$, the delamination length from $D = 0$ to $D = 400$, and the characteristic wave speed, c. For most delamination starting positions, as the delamination length increased, the phase shift of the leading peak in the second soft bonded region also increased, primarily in a nonlinear fashion, except at $x_2 = 0$, where the increase was linear. A 'yoyo' effect was observed, with the gradient of the phase shift increasing to a certain point, then decreasing, and repeating this pattern. In the lower layer, where we considered c values such as $c = 1.25$ and $c = 1.5$, there was less variation between each x_2 curve due to reduced wave evolution. For c values such as $c = 2.0$, the variation between x_2 curves was minimal, leading us to omit further analysis of these higher c values. For arbitrary phase shift values, we identified a common delamination length and position for both layers by using our phase shift plots. This demonstrates that specific waveguide

configurations can be determined without prior knowledge of the setup. Additionally, we analysed the phase shift for waves propagating from right to left in the upper waveguide. We then demonstrated that, while the phase shift might decrease with increasing delamination length, the overall wave packet consistently moved forward as the delamination grew. This observation aligns with the theory that the delaminated region has a greater group speed than the soft bonded region [26].

In Chapter 5, we focused on analysing wave behaviour in multi-layered structures to further our understanding of delamination detection. We first studied a multi-layered waveguide with a delaminated region 'sandwiched' between perfectly bonded regions, where the structure could extend to any number of layers since the materials were identical. We formulated the governing equations for the longitudinal wave displacements, constructed the weakly-nonlinear solutions, and established the initial conditions. We expanded upon the IST method introduced in Chapter 3, generalising the incident solitary wave to account for the Full Width at Half Maximum (FWHM). We then examined a similar structure, which was the two-layered waveguide from Chapter 4; however, in this case, both layers were composed of similar materials, resulting in the generation of radiating solitary waves. We conducted preliminary simulations for various waveguide configurations and geometries, n and k, and observed that as the n and k values increased, more solitons were generated in the regions following delamination. We then varied the delamination length in the perfectly bonded scenario and compared it against a measure, σ, derived from the wave amplitudes in the perfectly bonded regions, based on both the simulation results and IST wave amplitude predictions. Across various FWHM values, an increase in delamination length led to a corresponding increase in σ, which approached a theoretical limit of $\sigma = 1$, the maximum relative change in wave amplitude between the regions. In some cases, the value nearly reached this limit but fell short due to the range of delamination lengths tested in the simulations. This pattern was consistently observed across different n and k values. We scaled σ so that all FWHM curves overlapped with the FWHM = 5 curve, meaning we could derive the results for FWHM = 5 and then use our scaling to obtain the results for the other FWHM cases. In the soft bonded case, since the IST couldn't be applied to the Ostrovsky equation, we used the wave amplitudes in the first and third regions to create a measure, ζ, which we then compared to varying delamination lengths. We observed that as the delamination length increased, ζ also increased in a mostly nonlinear fashion across all FWHM curves. Similar to the perfectly bonded case, we then scaled the curves for different FWHM values using $\tilde{\zeta}$, so that they overlap with a reference curve at FWHM = 5. We then scaled our Boussinesq equations to nondimensional form, utilising experimental data parameters to determine delamination lengths in practical setups.

6.2 Further work

For future work, implementing higher-order corrections to the weakly-nonlinear solutions is expected to improve the agreement between the semi-analytical approach and the finite difference method, particularly for waves further from the leading wave peak. In the bonded region discussed in Section 4.2.2, we could construct the following weakly-nonlinear solutions:

$$f^{(i)}(x,t) = T^{(i)}(\xi, X) + R^{(i)}(\eta, X) + \varepsilon P^{(i)}(\xi, \eta, X) + \varepsilon^2 P_2^{(i)}(\xi, \eta, X) + \mathcal{O}(\varepsilon^3), \tag{6.1}$$

$$g^{(i)}(x,t) = S^{(i)}(\nu, X) + G^{(i)}(\zeta, X) + \varepsilon Q^{(i)}(\nu, \zeta, X) + \varepsilon^2 Q_2^{(i)}(\nu, \zeta, X) + \mathcal{O}(\varepsilon^3), \tag{6.2}$$

where $P_2^{(i)}(\xi, \eta, X)$ and $Q_2^{(i)}(\nu, \zeta, X)$ are higher-order correction terms that could be included. Similarly to the leading order case, we would substitute $f^{(i)}$ and $g^{(i)}$ into the Boussinesq equations for longitudinal wave displacement, then use averaging techniques to derive the higher-order solutions. With these higher-order solutions, we would apply the pseudospectral scheme to obtain numerical approximations for the wave propagation. Although the methodology is similar to that used when incorporating up to leading order terms in the weakly-nonlinear solutions, the mathematical complexity of incorporating higher-order terms is significantly greater and beyond the scope of this thesis.

Another avenue for future work could involve incorporating relaxed bonding between the two layers of the structure. This type of bonding is much weaker than soft bonding and was modelled by an asymptotic long-wave model in [29]. Analysing the wave behaviour in this relaxed bonded case would improve our understanding of a broader range of structures, increasing the applicability of delamination detection, as real-world applications often involve various bonding types. Similar to the reason that higher-order corrections were not explored, the mathematical complexity of finding leading order solutions and applying the semi-analytical method requires significant additional work, which is why it is beyond the scope of this thesis.

In Chapter 5, we partially explored a three-layered waveguide structure with perfect bonding. Since the materials of each layer were identical, the solution for one layer applied to all, simplifying the problem to solving for just one layer. However, when the waveguides consist of different materials, as in the soft bonded cases, it becomes necessary to solve for each of the three layers individually, significantly increasing the mathematical complexity. If the wave speeds in each layer are similar, solitons will evolve into radiating solitary waves. The interactions among these waves across the three layers will complicate the interpretation of the scattering results. This added complexity, combined with the extensive computational effort required, limited our ability to explore this scenario within the scope of this thesis.

Appendix A

Finite difference method

In this appendix, we will apply the finite difference method to two cases: a single Boussinesq equation and the initial value problem for a system of M coupled Boussinesq equations. This approach will encompass all instances of the finite difference method used throughout this thesis.

We will begin with the finite difference method applied to a single Boussinesq equation. This will involve discretising the equation over a defined spatial and temporal domain and substituting the necessary finite difference approximations into our Boussinesq equation. By reducing the continuous equation to a discretised form, we expect to obtain a tridiagonal matrix representation that can be solved using the Thomas algorithm [104]. This formulation will effectively incorporate boundary conditions and ensures accurate numerical solutions for the Boussinesq equation.

This initial case lays the groundwork for treating M coupled Boussinesq equations, as discussed in Chapters 4 - 5. In this case, we will consider the general formulation, from which specific cases can be derived by simply adjusting the coefficient values. The method is also applicable in Chapter 3 where the lower layer is neglected. We again employ a discretisation process while introducing ghost points to manage boundary conditions effectively throughout the derivation of our numerical scheme.

A.1 Boussinesq equation

Firstly, let us recall the following general Boussinesq-type equation (2.20) as:

$$u_{tt} - c^2 u_{xx} = \varepsilon(\alpha u_x u_{xx} + \beta u_{ttxx}). \tag{A.1}$$

We consider the discretisation process, which involves dividing the domain $[-L, L] \times [0, T]$ into a grid with uniform spacing, represented by Δx in the spatial direction and Δt in the temporal direction. We approximate the analytical solution $u(x, t)$ by the finite difference scheme, denoted as $u(i\Delta x, j\Delta t) = u_{i,j}$, where we have $i = 0, 1, ..., N$ and $j = 0, 1, ...$ Consequently, the time derivatives are represented by second order central differences as

$$u_t = \frac{u_{i,j+1} - u_{i,j-1}}{2\Delta t} + \mathcal{O}(\Delta t^2) \quad \text{and} \quad u_{tt} = \frac{u_{i,j+1} - 2u_{i,j} + u_{i,j-1}}{\Delta t^2} + \mathcal{O}(\Delta t^2), \tag{A.2}$$

and the spatial derivatives are also represented by second order central differences as

$$u_x = \frac{u_{i+1,j} - u_{i-1,j}}{2\Delta x} + \mathcal{O}(\Delta x^2) \quad \text{and} \quad u_{xx} = \frac{u_{i+1,j} - 2u_{i,j} + u_{i-1,j}}{\Delta x^2} + \mathcal{O}(\Delta x^2). \tag{A.3}$$

For simplification, we introduce the notation

$$D_{xx}(u_{i,j}) = \Delta x^2 u_{xx} \approx u_{i+1,j} - 2u_{i,j} + u_{i-1,j}. \tag{A.4}$$

Multiplying the approximations for u_x and u_{xx} together after omitting $\mathcal{O}(\Delta x^2)$ gives

$$u_x u_{xx} = \frac{(u_{i,j+1})^2 - 2(u_{i,j})(u_{i,j+1}) + 2(u_{i,j})(u_{i,j-1}) - (u_{i,j-1})^2}{2\Delta x^3}. \tag{A.5}$$

To determine the central finite difference representation for u_{ttxx}, we first apply the second time derivative operator to the second spatial derivative operator and then apply the resulting operator to u. This yields

$$u_{ttxx} \approx \frac{u_{i+1,j+1} - 2u_{i,j+1} + u_{i-1,j+1}}{\Delta t^2 \Delta x^2} + \frac{-2u_{i+1,j} + 4u_{i,j} - 2u_{i-1,j}}{\Delta t^2 \Delta x^2} + \frac{u_{i+1,j-1} - 2u_{i,j-1} + u_{i-1,j-1}}{\Delta t^2 \Delta x^2}. \tag{A.6}$$

Now substituting the respective finite difference approximations into (A.1) yields

$$\begin{aligned}
&\frac{u_{i,j+1} - 2u_{i,j} + u_{i,j-1}}{\Delta t^2} - c^2 \frac{D_{xx}(u_{i,j})}{\Delta x^2} \\
&= \varepsilon \left[\frac{\alpha}{2} \left((u_{i+1,j})^2 - 4(u_{i+1,j})(u_{i,j}) - 4(u_{i-1,j})(u_{i,j}) + (u_{i-1,j})^2 \right) \right. \\
&\quad \left. + \beta \left(\frac{u_{i+1,j+1} - 2u_{i,j+1} + u_{i-1,j+1}}{\Delta t^2 \Delta x^2} + \frac{-2u_{i+1,j} + 4u_{i,j} - 2u_{i-1,j}}{\Delta t^2 \Delta x^2} + \frac{u_{i+1,j-1} - 2u_{i,j-1} + u_{i-1,j-1}}{\Delta t^2 \Delta x^2} \right) \right].
\end{aligned} \tag{A.7}$$

After some rearrangement, (A.7) can be expressed as

$$\begin{aligned}
&\left(\Delta x^2 + 2\varepsilon\beta\right) u_{i,j+1} - \varepsilon\beta u_{i+1,j+1} - \varepsilon\beta u_{i-1,j+1} \\
&= \Delta t^2 c^2 D_{xx}(u_{i,j}) + \left(2\Delta x^2 + 4\varepsilon\beta\right) u_{i,j} - \left(\Delta x^2 + 2\varepsilon\beta\right) u_{i,j-1} \\
&\quad + \frac{\varepsilon\alpha\Delta t^2 (u_{i+1,j})^2}{2\Delta x^2} - 2\varepsilon\alpha\Delta t^2 (u_{i+1,j})(u_{i,j}) + 2\varepsilon\alpha\Delta t^2 (u_{i-1,j})(u_{i,j}) \\
&\quad + \frac{\varepsilon\alpha\Delta t^2 (u_{i-1,j})^2}{2\Delta x^2} - 2\varepsilon\beta u_{i+1,j} - 2\varepsilon\beta u_{i-1,j} + \varepsilon\beta u_{i+1,j-1} + \varepsilon\beta u_{i-1,j-1}.
\end{aligned} \tag{A.8}$$

We can denote the right-hand side of (A.8) as f_i, thus yielding

$$(\Delta x^2 + 2\varepsilon\beta) u_{i,j+1} - \varepsilon\beta u_{i+1,j+1} - \varepsilon\beta u_{i-1,j+1} = f_i. \tag{A.9}$$

Now we can express (A.9) in tridiagonal matrix form as

$$\begin{pmatrix}
\Delta x^2 + 2\varepsilon\beta & -2\varepsilon\beta & & & \\
-\varepsilon\beta & \Delta x^2 + 2\varepsilon\beta & -\varepsilon\beta & & \\
& \ldots & \ldots & \ldots & \\
& -\varepsilon\beta & \Delta x^2 + 2\varepsilon\beta & -\varepsilon\beta & \\
& & -\varepsilon\beta & \Delta x^2 + 2\varepsilon\beta
\end{pmatrix}
\begin{pmatrix} u_{0,j+1} \\ u_{1,j+1} \\ \ldots \\ u_{N-1,j+1} \\ u_{N,j+1} \end{pmatrix}
= \begin{pmatrix} f_0 \\ f_1 \\ \ldots \\ f_{N-1} \\ f_N \end{pmatrix}, \tag{A.10}$$

for $j = 0, 1, \ldots$. This tridiagonal system can be solved via the Thomas algorithm which is an optimisation of Gaussian elimination [104]. Since we're dealing with localised initial displacement data, we can achieve zero boundary conditions for the displacement by selecting a sufficiently large value for L. With $u = 0$ imposed on the boundaries within the interval $[-L, L]$, we also impose $u_x = 0$. Applying a central difference approximation to this condition gives

$$u_x = \frac{u_{i+1,j} - u_{i-1,j}}{2\Delta x} = 0 \implies u_{i+1,j} = u_{i-1,j}, \tag{A.11}$$

for $j = 1, 2, ...$ at $i = 0$ and $i = N$. Since the bar length is sufficiently large, the boundary conditions are imposed far enough from the propagating waves, allowing us to set

$$u_{0,j} = u_{N,j} = 0 \quad \forall j \in \{1, 2, 3, \dots\} \tag{A.12}$$

The initial conditions are chosen to represent a solitary wave solution, assuming that the initial state corresponds to a traveling soliton. Consequently, the solutions after the initial conditions are shifted by $v_1 \Delta t$. Thus, we set

$$u_{i,0} = 3(c_1^2 - 1)\,\mathrm{sech}^2\left(\frac{i\Delta x\sqrt{c_1^2 - 1}}{2c_1}\right), \quad \text{and} \quad u_{i,1} \quad = 3(c_1^2 - 1)\,\mathrm{sech}^2\left(\frac{(i\Delta x - v_1\Delta t)\sqrt{c_1^2 - 1}}{2c_1}\right). \tag{A.13}$$

If the boundary values are not assumed to be zero, we calculate the values at the boundary points for $j = 1, 2, ...$, ensuring that the tridiagonal matrix is modified to include the term $u_{-1,j+1}$. To apply the Thomas algorithm in this case, we introduce the variables ρ_1 and ρ_2, where $\rho_1 = \Delta x^2 + 2\rho_2$ and $\rho_2 = \varepsilon\beta$. Substituting these terms into (A.10) simplifies the tridiagonal system to

$$\begin{pmatrix} \rho_1 & -2\rho_2 & & \\ -\rho_2 & \rho_1 & -\rho_2 & \\ & \dots & \dots & \\ & -\rho_2 & \rho_1 & -\rho_2 \\ & & -2\rho_2 & \rho_1 \end{pmatrix} \begin{pmatrix} u_{0,j+1} \\ u_{1,j+1} \\ \dots \\ u_{N-1,j+1} \\ u_{N,j+1} \end{pmatrix} = \begin{pmatrix} f_0 \\ f_1 \\ \dots \\ f_{N-1} \\ f_N \end{pmatrix}, \tag{A.14}$$

which can be expressed as

$$\begin{pmatrix} 1 & \gamma_1 & & \\ 0 & 1 & \gamma_2 & \\ & 0 & 1 & \gamma_3 \\ & \dots & \dots & \dots \\ & 0 & 1 & \gamma_{N-1} \\ & & 0 & 1 \end{pmatrix} \begin{pmatrix} u_{0,j+1} \\ u_{1,j+1} \\ u_{2,j+1} \\ \dots \\ u_{N-1,j+1} \\ u_{N,j+1} \end{pmatrix} = \begin{pmatrix} g_0 \\ g_1 \\ g_2 \\ \dots \\ g_{N-1} \\ g_N \end{pmatrix}, \tag{A.15}$$

where the values $\gamma_1 = \frac{-2\rho_2}{\rho_1}$, $g_0 = \frac{f_0}{\rho_1}$, $\gamma_i = \frac{\rho_2}{\rho_1 + \rho_2\gamma_{i-1}}$ for $i = 2, 3, \dots, N-1$, and $g_i = \frac{f_i + \rho_2 g_{i-1}}{\rho_1 + \rho_2\gamma_i}$ for $i = 1, 2, \dots, N$. The left boundary point, $i = 0$, in implicit form, can be determined by substituting γ_1

and g_0 into the first row of (A.15), allowing us to express $u_{0,j+1}$ in terms of the iterative point:

$$u_{0,j+1} = \frac{2\varepsilon\beta u_{1,j+1} + f_0}{\Delta x^2 + 2\varepsilon\beta}. \tag{A.16}$$

A similar process can be applied to determine the values for the remaining points, including the right boundary point, $i = N$.

A.2 Initial value problem for a system of M coupled Boussinesq equations

In this thesis, we examined structures consisting of multiple regions, with the wave displacement governed by a set of Boussinesq-type equations with boundary and continuity conditions. While Section A.1 applied the finite difference method to the single Boussinesq equation, this approach alone is insufficient for solving the entire system. Thus, we must extend our methodology to address the full system of Boussinesq-type equations.

Let us extend the finite difference method from Section A.1 to a two layered structure with M sections, each described by a system of coupled (cRB) or uncoupled Boussinesq equations. The equations for each section are given by

$$\begin{aligned} u_{tt}^{(l)} - u_{xx}^{(l)} &= 2\varepsilon \left[-6u_x^{(l)} u_{xx}^{(l)} + u_{ttxx}^{(l)} - \delta_l \left(u^{(l)} - w^{(l)} \right) \right], \\ w_{tt}^{(l)} - c_l^2 w_{xx}^{(l)} &= 2\varepsilon \left[-6\alpha_l w_x^{(l)} w_{xx}^{(l)} + \beta_l w_{ttxx}^{(l)} + \gamma_l \left(u^{(l)} - w^{(l)} \right) \right], \quad x_{l-1} < x < x_l, \end{aligned} \tag{A.17}$$

where the variables retain the same meanings as in the previous section, with the exception of δ_l and γ_l, which are coupling coefficients dependent on the properties of the soft bonding layer, and are the only unknowns, obtained through parameter rescaling. The subscripts 1 and 2 refer to the coefficients for the upper and lower layers, respectively, and x_l represents the interface position between sections. The equations are defined for each section $l = 1, 2, ..., M$.

We enforce continuity of the longitudinal displacement and normal stress at the interface between the equations, given by

$$u^{(l)}|_{x=x_l} = u^{(l+1)}|_{x=x_l}, \quad w^{(l)}|_{x=x_l} = w^{(l+1)}|_{x=x_l}, \tag{A.18}$$

and

$$\begin{aligned} u_x^{(l)} + 2\varepsilon\left[-3\left(u_x^{(l)}\right)^2 + u_{ttx}^{(l)}\right]\Big|_{x=x_l} &= u_x^{(l+1)} + 2\varepsilon\left[-3\left(u_x^{(l+1)}\right)^2 + u_{ttx}^{(l+1)}\right]\Big|_{x=x_l}, \\ c_l^2 w_x^{(l)} + 2\varepsilon\left[-3\alpha_l\left(w_x^{(l)}\right)^2 + \beta_l w_{ttx}^{(l)}\right]\Big|_{x=x_l} &= c_{i+1}^2 w_x^{(l+1)} + 2\varepsilon\left[-3\alpha_{l+1}\left(w_x^{(l+1)}\right)^2 + \beta_{i+1} w_{ttx}^{(l+1)}\right]\Big|_{x=x_l}, \end{aligned} \tag{A.19}$$

respectively, for $l = 1, 2, ..., M-1$. To find a numerical solution for the equation system (A.17) - (A.19), we again make use of central difference approximations, similarly as in the previous sections. Note that the discretisation in x can vary across sections, allowing for finer mesh in regions with complex waves and a coarser mesh where the solution is simpler, improving the computational efficiency. The time step Δt will be determined by the smallest spatial discretisation, i.e., $\Delta x_{\min} = \min_{i=1,2,...,M}\Delta x_i$. Substituting the respective approximations into system (A.17) results in a coupled system of tridiagonal equations, of the form

$$\begin{aligned} &- 2\varepsilon u_{i+1,j+1}^{(l)} + \left(4\varepsilon + \Delta x_l^2\right) u_{i,j+1}^{(l)} - 2\varepsilon u_{i-1,j+1}^{(l)} = \left(\Delta t^2 - 4\varepsilon\right) D_{xx}\left(u_{i,j}^{(l)}\right) \\ &+ 2\Delta x_l^2 u_{i,j}^{(l)} - \frac{6\varepsilon\Delta t^2}{\Delta x_l}\left[\left(u_{i+1,j}^{(l)}\right)^2 - \left(u_{i-1,j}^{(l)}\right)^2 - 2u_{i+1,j}^{(l)}u_{i,j}^{(l)} + 2u_{i,j}^{(l)}u_{i-1,j}^{(l)}\right] \\ &+ 2\varepsilon u_{i+1,j-1}^{(l)} - \left(4\varepsilon + \Delta x_l^2\right) u_{i,j-1}^{(l)} + 2\varepsilon u_{i-1,j-1}^{(l)} - 2\varepsilon\delta_l\Delta x_l^2\Delta t^2\left(u_{i,j}^{(l)} - w_{i,j}^{(l)}\right), \end{aligned} \tag{A.20}$$

and

$$\begin{aligned} &- 2\varepsilon\beta_l w_{i+1,j+1}^{(l)} + \left(4\varepsilon + \Delta x_l^2\right) w_{i,j+1}^{(l)} - 2\varepsilon\beta_l w_{i-1,j+1}^{(l)} = \left(\Delta t^2 c_l^2 - 4\varepsilon\beta_l\right) D_{xx}\left(w_{i,j}^{(l)}\right) \\ &+ 2\Delta x_l^2 w_{i,j}^{(l)} - \frac{6\varepsilon\alpha_l\Delta t^2}{\Delta x_l}\left[\left(w_{i+1,j}^{(l)}\right)^2 - \left(w_{i-1,j}^{(l)}\right)^2 - 2w_{i+1,j}^{(l)}w_{i,j}^{(l)} + 2w_{i,j}^{(l)}w_{i-1,j}^{(l)}\right] \\ &+ 2\varepsilon\beta_l w_{i+1,j-1}^{(l)} - \left(4\varepsilon\beta_l + \Delta x_l^2\right) w_{i,j-1}^{(l)} + 2\varepsilon w_{i-1,j-1}^{(l)} - 2\varepsilon\gamma_l\Delta x_l^2\Delta t^2\left(u_{i,j}^{(l)} - w_{i,j}^{(l)}\right), \end{aligned} \tag{A.21}$$

for $i = 0, 1, ..., N_l$. Assuming the domain $[x_{l-1}, x_l] \times [0, T]$ is discretised, the number of points in each section is calculated as $N_l = (x_l - x_{l-1})/\Delta x_l$, with $i = 0, 1, ..., N_l$. Thus, the continuity condition (A.18) becomes

$$u_{N_l,j+1}^{(l)} = u_{0,j+1}^{(l+1)}, \quad w_{N_l,j+1}^{(l)} = w_{0,j+1}^{(l+1)}. \tag{A.22}$$

We substitute the central difference approximations into the continuity condition (A.19), introducing "ghost points" in the form of $u_{N_l+1,j+1}^{(l)}$, $u_{-1,j+1}^{(l+1)}$, $w_{N_l+1,j+1}^{(l)}$, and $w_{-1,j+1}^{(l+1)}$, consequently transforming the

first equation in (A.19) into the form

$$\begin{aligned}
&\Delta x_l \Delta t^2 \left(u^{(l)}_{N_l+1,j+1} - u^{(l)}_{N_l-1,j+1}\right) - 2\Delta x_l \varepsilon \Big(2u^{(l)}_{N_l+1,j+1} - 2u^{(l)}_{N_l-1,j+1} - 5u^{(l)}_{N_l+1,j} + 5u^{(l)}_{N_l-1,j} \\
&+ 4u^{(l)}_{N_l+1,j-1} - 4u^{(l)}_{N_l-1,j-1} - u^{(l)}_{N_l+1,j-2} + u^{(l)}_{N_l-1,j-2}\Big) \\
&- 3\Delta t^2 \varepsilon \left[\left(u^{(l)}_{N_l+1,j+1}\right)^2 + \left(u^{(l)}_{N_l-1,j+1}\right)^2 - 2u^{(l)}_{N_l+1,j+1} u^{(l)}_{N_l-1,j+1}\right] \\
&= \frac{\Delta x_l^2}{\Delta x_{l+1}} \Delta t^2 \left(u^{(l+1)}_{1,j+1} - u^{(l+1)}_{-1,j+1}\right) + 2\frac{h_l^2}{h_{l+1}} \varepsilon \Big(2u^{(l+1)}_{1,j+1} - 2u^{(l+1)}_{-1,j+1} - 5u^{(l+1)}_{1,j} + 5u^{(l+1)}_{-1,j} + 4u^{(l+1)}_{1,j-1} \\
&- 4u^{(l+1)}_{-1,j-1} - u^{(l+1)}_{1,j-2} + u^{(l+1)}_{-1,j-2}\Big) - 3\frac{\Delta x_l^2}{\Delta x_{l+1}^2} \Delta t^2 \varepsilon \left[\left(u^{(l+1)}_{1,j+1}\right)^2 + \left(u^{(l+1)}_{-1,j+1}\right)^2 - 2u^{(l+1)}_{1,j+1} u^{(l+1)}_{-1,j+1}\right], \qquad \text{(A.23)}
\end{aligned}$$

and similarly transforming the second equation in (A.19) to obtain

$$\begin{aligned}
&\Delta x_l \Delta t^2 c_l^2 \left(w^{(l)}_{N_l+1,j+1} + w^{(l)}_{N_l-1,j+1}\right) + 2\Delta x \varepsilon \beta_l \Big(2w^{(l)}_{N_l+1,j+1} - 2w^{(l)}_{N_l-1,j+1} - 5w^{(l)}_{N_l+1,j} + 5w^{(l)}_{N_l-1,j} \\
&\quad + 4w^{(l)}_{N_l+1,j-1} - 4w^{(l)}_{N_l-1,j-1} - w^{(l)}_{N_l+1,j-2} + w^{(l)}_{N_l-1,j-2}\Big) \\
&- 3\Delta t^2 \varepsilon \alpha_l \left[\left(w^{(l)}_{N_l+1,j+1}\right)^2 + \left(w^{(l)}_{N_l-1,j+1}\right)^2 - 2w^{(l)}_{N_l+1,j+1} w^{(l)}_{N_l-1,j+1}\right] \\
&= \frac{\Delta x_l^2}{\Delta x_{l+1}} \Delta t^2 c_{l+1}^2 \left(w^{(l+1)}_{1,j+1} - w^{(l+1)}_{-1,j+1}\right) + 2\frac{\Delta x_l^2}{\Delta x_{l+1}} \varepsilon \beta_{l+1} \Big(2w^{(l+1)}_{1,j+1} - 2w^{(l+1)}_{-1,j+1} - 5w^{(l+1)}_{1,j} + 5w^{(l+1)}_{-1,j} \\
&\quad + 4w^{(l+1)}_{1,j-1} - 4w^{(l+1)}_{-1,j-1} - w^{(l+1)}_{1,j-2} + w^{(l+1)}_{-1,j-2}\Big) \\
&- 3\frac{\Delta x_l^2}{\Delta x_{l+1}^2} \Delta t^2 \varepsilon \alpha_{l+1} \left[\left(w^{(l+1)}_{1,j+1}\right)^2 + \left(w^{(l+1)}_{-1,j+1}\right)^2 - 2w^{(l+1)}_{1,j+1} w^{(l+1)}_{-1,j+1}\right], \qquad \text{(A.24)}
\end{aligned}$$

for u and w respectively.

As we are again considering localised initial data for strains, choosing a sufficiently large L allows us to impose zero boundary conditions for the strain, i.e., $u_x = 0$. Enforcing the boundary conditions at the first and last sections gives

$$u^{(1)}_{1,j+1} = u^{(1)}_{-1,j+1} \text{ and } u^{(M)}_{N_M+1,j+1} = u^{(M)}_{N_M-1,j+1}, \qquad \text{(A.25)}$$

and equivalent relations for w. Therefore, since we have consistently applied central difference approximations, we now have a second-order scheme.

In each domain there are two ghost points: one at the left boundary and one at the right boundary. The exceptions are the first domain, which has no ghost point on the left, and the M–th domain, which has no ghost point on the right. To accommodate these exceptions, we rearrange the boundary conditions. Accordingly, we define the right-hand side of (A.20) as $f_i^{(l)}$ and that of (A.21) as $g_i^{(l)}$ for the corresponding

values of i as

$$\tilde{f}_0^l = f_0^{(l)} + 2\varepsilon u_{-1,j+1}^{(l)}, \quad \tilde{f}_{N_l}^l = f_{N_l}^{(l)} + 2\varepsilon u_{N_l+1,j+1}^{(l)}, \tag{A.26}$$

$$\tilde{g}_0^l = g_0^{(l)} + 2\varepsilon\beta_l w_{-1,j+1}^{(l)}, \quad \tilde{g}_{N_l}^l = g_{N_l}^{(l)} + 2\varepsilon\beta_l w_{N_l+1,j+1}^{(l)}, \tag{A.27}$$

We can express (A.20) in matrix form for each section, with two exceptional cases at the boundaries. In the first section, for $i = 0, 1, ..., N_1$, we have

$$A\begin{pmatrix} u_{0,j+1}^{(1)}, & u_{1,j+1}^{(1)}, & \dots, & u_{N_1-1,j+1}^{(1)}, & u_{N_1,j+1}^{(1)} \end{pmatrix} = \begin{pmatrix} f_0^{(1)}, & f_1^{(1)}, & \dots, & f_{N_1-1}^{(1)}, & \tilde{f}_{N_1}^{(1)} \end{pmatrix}. \tag{A.28}$$

For the final section, we similarly have:

$$A\begin{pmatrix} u_{0,j+1}^{(M)}, & u_{1,j+1}^{(M)}, & \dots, & u_{N_M-1,j+1}^{(M)}, & u_{N_M,j+1}^{(M)} \end{pmatrix} = \begin{pmatrix} \tilde{f}_0^{(M)}, & \tilde{f}_1^{(M)}, & \dots, & f_{N_M-1}^{(M)}, & f_{N_M}^{(M)} \end{pmatrix}. \tag{A.29}$$

For all other regions where $1 < l < M$, the system of linear equations takes the form

$$A\begin{pmatrix} u_{0,j+1}^{(l)}, & u_{1,j+1}^{(l)}, & \dots, & u_{N_l-1,j+1}^{(l)}, & u_{N_l,j+1}^{(l)} \end{pmatrix} = \begin{pmatrix} \tilde{f}_0^{(l)}, & f_1^{(l)}, & \dots, & f_{N_1-1}^{(l)}, & \tilde{f}_{N_1}^{(l)} \end{pmatrix}, \tag{A.30}$$

where

$$A = \begin{pmatrix} 4\varepsilon + \Delta x^2 & -4\varepsilon & & & \\ -2\varepsilon & 4\varepsilon + \Delta x^2 & -2\varepsilon & & \\ & ... & ... & ... & \\ & -2\varepsilon & 4\varepsilon + \Delta x^2 & -2\varepsilon & \\ & & -2\varepsilon & 4\varepsilon + \Delta x^2 & \end{pmatrix}. \tag{A.31}$$

A similar system can be formed for (A.21), but we omit this expression for brevity. We now have the tridiagonal systems for the functions u and w, which can be solved implicitly using the Thomas algorithm, while considering the ghost points at both the left-hand and right-hand boundaries. As a result, the solution at each point can be expressed in terms of the explicit solution, when ghost points are absent, and a multiplicative factor from the ghost points as

$$u_{i,j+1}^{(l)} = \phi_i^{(l)} + \psi_i^{(l)} u_{-1,j+1}^{(l)} + \omega_i^{(l)} u_{N_i+1,j+1}^{(l)}, \tag{A.32}$$

where we have a similar relationship for w, and $\phi_i^{(l)}$ $\psi_i^{(l)}$ and $\omega_i^{(l)}$ are coefficents from (A.28)–(A.30). We note that $\psi_i^{(1)} = 0$ and $\omega_i^{(M)} = 0$ because there are no ghost points at these far boundaries.

From the system of linear equations (A.28)–(A.30), we can estimate the coefficient vectors ϕ and ω.

Using the Thomas algorithm, we observe that these coefficients depend on Δx, the step size, which we assume to be small enough so that we can omit it. To simplify the estimation, we neglect terms greater than order Δx in the estimates that follow. Under this assumption, for $i = 0, 1, ..., N_l$, the coefficients are determined as

$$\psi_i^{(l)} = \frac{N_l + 1 - i}{N_l + 2}, \quad \omega_i^{(l)} = \frac{1 + i}{N_i + 2}. \tag{A.33}$$

For a sufficiently large domain, or small Δx, the coefficient of the left ghost point approaches zero at the right-hand boundary, and similarly, the right ghost point at the left-hand boundary. Our calculations for $N = 50000$ yielded a boundary value of essentially zero ($O(10^{-300})$), which is below machine precision ($O(10^{-16})$). This indicates that a suitable Δx and corresponding N can be determined for most domain sizes. As a result, we can simplify the problem to solving just two equations at each interface, involving two ghost points. To derive this nonlinear equation, we first rewrite $u_{-1,j+1}^{(l+1)}$ in terms of $u_{N_l+1,j+1}^{(l)}$ using (A.22). Then, we substitute the expressions for $u_{N_l-1,j+1}^{(l)}$ and $u_{1,j+1}^{(l+1)}$ from (A.32) in terms of the ghost points. Substituting these into (A.22) yields

$$\phi_{N_l}^{(l)} + \omega_{N_l}^{(l)} u_{N_l+1,j+1}^{(l)} = \phi_0^{(l+1)} + \psi_0^{(l+1)} u_{-1,j+1}^{(l+1)}, \tag{A.34}$$

and therefore we have

$$\begin{aligned} u_{-1,j+1}^{(l+1)} &= \frac{\phi_{N_l}^{(l)} - \phi_0^{(l+1)} + \omega_{N_l}^{(l)} u_{N_l+1,j+1}^{(l)}}{\psi_0^{(l+1)}}, \\ u_{1,j+1}^{(l+1)} &= \phi_1^{(l+1)} + \frac{\psi_1^{(l+1)}}{\psi_0^{(l+1)}} \left(\phi_{N_l}^{(l)} - \phi_0^{(l+1)} + \omega_{N_l}^{(l)} u_{N_l+1,j+1}^{(l)} \right). \end{aligned} \tag{A.35}$$

We follow a similar approach for w. By substituting (A.32) and (A.33) into (A.23), which results in a quadratic equation for $u_{N_l+1,j+1}^{(l)}$, written explicitly as

$$h_0 \left(u_{N_l+1,j+1}^{(l)} \right)^2 + h_1 u_{N_l+1,j+1}^{(l)} + h_2 = 0, \tag{A.36}$$

where

$$
\begin{aligned}
h_0 &= -3\Delta t^2\varepsilon\left(\omega_{N_l-1}^{(l)}-1\right)^2+3\frac{\Delta x_l^2}{\Delta x_{l+1}^2}\Delta t^2\varepsilon\left(\frac{\omega_{N_l}^{(l)}}{\psi_0^{(l+1)}}\right)^2\left(\psi_1^{(l+1)}-1\right)^2,\\
h_1 &= \left(1-\omega_{N_l-1}^{(l)}\right)\left(\Delta x_l\Delta t^2+4\Delta x_l\varepsilon+6\Delta t^2\varepsilon\phi_{N_l-1}^{(l)}\right)\\
&\quad+\left(1-\psi_1^{(l+1)}\right)\left(\frac{\omega_{N_l}^{(l)}}{\psi_0^{(l+1)}}\right)\left(\frac{\Delta x_l^2}{\Delta x_{l+1}}\Delta t^2+4\frac{\Delta x_l^2}{\Delta x_{l+1}}\varepsilon-6\frac{\Delta x_l^2}{\Delta x_{l+1}^2}\Delta t^2\varepsilon\phi_1^{(l+1)}\right)\\
&\quad+6\frac{\Delta x_l^2}{\Delta x_{l+1}^2}\Delta t^2\varepsilon\frac{\omega_{N_l}^{(l)}\left(\phi_{N_l}^{(l)}-\phi_0^{(l+1)}\right)}{\left(\psi_0^{(l+1)}\right)^2}\left[\left(\psi_1^{(l+1)}\right)^2-2\psi_1^{(l+1)}+1\right],\\
h_2 &= --\phi_{N_l-1}^{(l)}\left(\Delta x_l\Delta t^2+4\Delta x_l\varepsilon\right)-3\Delta t^2\varepsilon\left(\phi_{N_l-1}^{(l)}\right)^2\\
&\quad+2\Delta x_l\varepsilon\left(-5u_{N_l+1,j}^{(l)}+5u_{N_l-1,j}^{(l)}+4u_{N_l+1,j-1}^{(l)}-4u_{N_l-1,j-1}^{(l)}-u_{N_l-1,j-2}^{(l)}+u_{N_l-1,j-2}^{(l)}\right)\\
&\quad+3\frac{\Delta x_l^2}{\Delta x_{l+1}^2}\Delta t^2\varepsilon\left[\left(\phi_1^{(l+1)}\right)^2+\left(\frac{\phi_{N_l}^{(l)}-\phi_0^{(l+1)}}{\psi_0^{(l+1)}}\left(\psi_1^{(l+1)}-1\right)\right)^2\right.\\
&\quad\left.+2\left(\psi_1^{(l+1)}-1\right)\left(\frac{\phi_1^{(l+1)}\left(\phi_{N_l}^{(l)}-\phi_0^{(l+1)}\right)}{\psi_0^{(l+1)}}\right)\right]\\
&\quad-\left(\frac{\Delta x_l^2}{\Delta x_{l+1}}\Delta t^2+4\frac{\Delta x_l^2}{\Delta x_{l+1}}\varepsilon\right)\left[\phi_1^{(l+1)}+\frac{\phi_{N_l}^{(l)}-\phi_0^{(l+1)}}{\psi_0^{(l+1)}}\left(\psi_1^{(l+1)}-1\right)\right]\\
&\quad-2\varepsilon\frac{\Delta x_l^2}{\Delta x_{l+1}}\left(-5u_{1,j}^{(l+1)}+5u_{-1,j}^{(l+1)}+4u_{1,j-1}^{(l+1)}-4u_{-1,j-1}^{(l+1)}-u_{1,j-2}^{(l+1)}+u_{-1,j-2}^{(l+1)}\right).
\end{aligned}
\tag{A.37}
$$

If $h_0 = 0$, a linear boundary equation must be solved. When the nonlinearity coefficients are the same across both sections of the bar, i.e., $\alpha_l = 1$, this condition $h_0 = 0$ holds. However, when $h_0 \neq 0$, and the nonlinearity coefficient varies between sections, we must select the correct sign in the quadratic equation. This sign is chosen to align with the behaviour of the solution in the adjacent regions.

The finite difference method has now been applied for the cases of a single Boussinesq and initial value problem for a system of M coupled Boussinesq equations. This comprehensive framework will allow us to run numerical simulations to explore wave propagation across the different layers.

Appendix B

Semi-analytical method - Pseudospectral scheme

In the forthcoming appendix, we will present a detailed analysis of a pseudospectral scheme that offers a semi-analytical solution for wave propagation, which is the second numerical scheme discussed in this thesis.

We will address three equations: the Korteweg-de Vries (KdV) equation, the single Ostrovsky equation, and the coupled Ostrovsky equation. These equations represent the leading order equations derived from our analysis of weakly-nonlinear wave propagation in various structures throughout this thesis. We will demonstrate how to apply the continuous Fourier transform to each equation, followed by the Discrete Fourier Transform (DFT) for numerical analysis. By transforming the spatial domain to facilitate computational methods, we will simplify the equations and implement the Fast Fourier Transform (FFT) algorithm. The Runge-Kutta 4th-order method will then be employed to discretise the transformed equations, in time, yielding accurate numerical approximations.

B.1 KdV equation

Firstly, let us consider the following KdV equation

$$f_T + \alpha f f_\xi + \beta f_{\xi\xi\xi} = 0, \tag{B.1}$$

where α and β are constants and the variables are defined as $T = \varepsilon t$ and $\xi = x - t$. The continuous Fourier transform yields a nonlinear ODE, which is difficult to solve analytically; therefore, the DFT will be used to obtain a numerical solution. Currently, the domain is defined on the intervals $t \in [0, \mathsf{T}]$ and $\xi \in [-L, L]$. We transform the spatial domain $\xi \in [-L, L]$ to $\tilde{\xi} \in [0, 2\pi]$ using the transformation $\tilde{\xi} = s\xi + \pi$, where $s = \pi/L$. We then express the derivatives with respect to ξ in terms of $\tilde{\xi}$, giving

$$f_\xi = s f_{\tilde{\xi}}, \quad f_{\xi\xi\xi} = s^3 f_{\tilde{\xi}\tilde{\xi}\tilde{\xi}}. \tag{B.2}$$

Substituting these expressions into (B.1) and omitting tildes yields

$$f_T + s\alpha f f_\xi + s^3 \beta f_{\xi\xi\xi} = 0. \tag{B.3}$$

To simplify the nonlinear terms we introduce the notation

$$f f_\xi = (z_a)_\xi = \left(\frac{f^2}{2}\right)_\xi. \tag{B.4}$$

The solution is discretised at N equally spaced points across the interval $\Delta\xi = 2\pi/N$, where N is a power of 2. This setup allows us to use the DFT

$$\hat{f}(k, T) = \frac{1}{\sqrt{N}} \sum_{j=0}^{N-1} f(\xi_j, T) e^{-ik\xi_j}, \quad -\frac{N}{2} \leq k \leq \frac{N}{2} - 1, \tag{B.5}$$

for each fixed T, where k is an integer representing the wavenumber. For $k \neq 0$, the Inverse Discrete Fourier Transform (IDFT) is

$$f(\xi, T) = \frac{1}{\sqrt{N}} \sum_{k=-\frac{N}{2}}^{\frac{N}{2}-1} \hat{f}(k, T) e^{ik\xi_j}, \quad j = 0, 1, ..., N-1. \tag{B.6}$$

The FFT algorithm is utilised to efficiently compute these transformations [105]. In Fourier space, spatial derivatives correspond to multiplication by powers of ik, such that

$$\frac{\partial}{\partial\tilde{\xi}} \to ik, \quad f_{\tilde{\xi}} \to ik\tilde{f}(k), \quad f_{\tilde{\xi}\tilde{\xi}\tilde{\xi}} \to -ik^3\tilde{f}(k). \tag{B.7}$$

Therefore, applying the DFT to (B.3), with respect to ξ, gives

$$\hat{f}_T + isk\alpha\hat{z}_a - is^3k^3\beta\hat{f} = 0. \tag{B.8}$$

We implement the Runge-Kutta 4th order method by assuming $\hat{f}_j = \hat{f}(k, j\Delta T)$ is the solution at $T = j\Delta T$ for (B.8). While Euler's method, as derived in [74], provides a valid approach, we opted for the Runge-Kutta method due to its higher accuracy and reduced error accumulation over time. Therefore, the solution at $T = (j+1)\Delta T$ is given by

$$\hat{f}_{k,(j+1)\Delta T} = \hat{f}_{k,j\Delta T} + \frac{1}{6}(a + 2b + 2c + d), \tag{B.9}$$

where a, b, c and d are functions of ξ at time T and are defined as

$$a = \Delta T F\left(\hat{f}_{k,j\Delta T}\right), \quad b = \Delta T F\left(\hat{f}_{k,j\Delta T} + \frac{a_1}{2}\right), \quad c = \Delta T F\left(\hat{f}_{k,j\Delta T} + \frac{b_1}{2}\right), \quad d = \Delta T F\left(\hat{f}_{k,j\Delta T} + c_1\right). \tag{B.10}$$

The function F is obtained by isolating the non-time derivative terms in (B.8), resulting in

$$F(\hat{f}) = \frac{isk\alpha\hat{z}_a}{is^3k^3\beta - 1}. \tag{B.11}$$

B.2 Single Ostrovsky equation

Let us consider the Ostrovsky equation

$$(T_X + \alpha TT_\nu + \beta T_{\nu\nu\nu})_\nu = \gamma T, \tag{B.12}$$

where T now represents a transmitted wave, with $\nu = x + t$ and $X = \varepsilon x$ as characteristic variables. Similarly to Section B.1, we map $\nu \in [-L, L]$ to $\tilde{\nu} \in [0, 2\pi]$ via the transformation $\tilde{\nu} = \frac{\pi}{L}\nu + \pi$, where $s = \pi/L$ and k is an integer representing the wavenumber, as defined previously. In addition, we define the DFT as

$$\hat{T}(k, X) = \frac{1}{\sqrt{N}} \sum_{j=0}^{N-1} T(\nu_j, X)e^{-ik\xi_j}, \quad -\frac{N}{2} \leq k \leq \frac{N}{2} - 1, \tag{B.13}$$

where k is defined as before. The IDFT is then given by

$$T(\nu, X) = \frac{1}{\sqrt{N}} \sum_{k=-\frac{N}{2}}^{\frac{N}{2}-1} \hat{T}(k, X) e^{-ik\xi_j}, \quad j = 0, 1, ..., N-1. \tag{B.14}$$

Applying the DFT to (B.12), while omitting tildes, yields

$$\hat{T}_X = -\alpha isk\widehat{(T)^2} + \beta is^3 k^3 \hat{T}_{\nu\nu\nu} - \gamma \frac{i}{sk}(-\hat{T}). \tag{B.15}$$

We now apply the Runge-Kutta 4th order method similarly as Section B.1. Thus, the solution at $X = (j+1)\Delta X$ is given by

$$\hat{T}_{k,(j+1)\Delta X} = \hat{T}_{k,j\Delta X} + \frac{1}{6}(a_1 + 2b_1 + 2c_1 + d_1), \tag{B.16}$$

where a_i, b_i, c_i and d_i are functions of ν at X and are defined as

$$\begin{aligned} a_i &= \Delta X g\left(\hat{T}_{k,j\Delta T}\right), \quad b_i = \Delta X g\left(\hat{T}_{k,j\Delta T} + \frac{a_1}{2}\right), \\ c_i &= \Delta X g\left(\hat{T}_{k,j\Delta T} + \frac{b_1}{2}\right), \quad d_i = \Delta X g\left(\hat{T}_{k,j\Delta T} + c_1\right). \end{aligned} \tag{B.17}$$

where the function g represents $\hat{T}_X$.

B.3 Coupled Ostrovsky equations

Building on the previous sections, we now extend the pseudospectral scheme to the right-propagating coupled Ostrovsky equations, which are denoted by

$$(I_X + \alpha_1 I I_\xi + \beta_1 I_{\xi\xi\xi})_\xi - \delta(I - S) = 0, \tag{B.18}$$

$$(S_X + \alpha_2 S S_\xi + \beta_2 S_{\xi\xi\xi} + \omega S_\xi)_\xi + \gamma(I - S) = 0, \tag{B.19}$$

where ω represents the coefficient of the S_ξ term. The system above is presented in a general form that includes this additional term to accommodate all cases discussed in this thesis, as required in examples such as (5.46). In cases where this term is not present in the Ostrovsky equation, the same pseudospectral method can be applied by setting $\omega = 0$. For the left-propagating coupled Ostrovsky equations, a similar methodology is used, and so the details are omitted here. Transforming the spatial domain $\xi \in [-L, L]$ to $\tilde{\xi} \in [0, 2\pi]$ using the change of variables $\tilde{\xi} = \frac{\pi}{L}\xi + \pi$ and applying this to (B.18), while omitting the

tildes, gives

$$\begin{aligned}\left(I_X + \alpha_1 isk II_\xi - \beta_1 is^3k^3 I_{\xi\xi\xi}\right)_\xi - \frac{\delta}{isk}(I-S) = 0,\\ \left(S_X + \alpha_2 isk SS_\xi - \beta_2 is^3k^3 S_{\xi\xi\xi} + isk\omega S_\xi\right)_\xi + \frac{\gamma}{isk}(I-S) = 0,\end{aligned} \tag{B.20}$$

where, as previously defined, $s = \pi/L$ and k is an integer representing the wavenumber. While the DFT is

$$\begin{aligned}\hat{I}(k,X) = \frac{1}{\sqrt{N}}\sum_{j=0}^{N-1} I(\xi_j, X)e^{-ik\xi_j}, \quad -\frac{N}{2} \le k \le \frac{N}{2} - 1,\\ \hat{S}(k,X) = \frac{1}{\sqrt{N}}\sum_{j=0}^{N-1} S(\xi_j, X)e^{-ik\xi_j}, \quad -\frac{N}{2} \le k \le \frac{N}{2} - 1,\end{aligned} \tag{B.21}$$

and the IDFT is

$$\begin{aligned}I(\xi,X) = \frac{1}{\sqrt{N}}\sum_{k=-\frac{N}{2}}^{\frac{N}{2}-1} \hat{I}(k,X)e^{-ik\xi_j}, \quad j = 0,1,...,N-1,\\ S(\xi,X) = \frac{1}{\sqrt{N}}\sum_{k=-\frac{N}{2}}^{\frac{N}{2}-1} \hat{S}(k,X)e^{-ik\xi_j}, \quad j = 0,1,...,N-1,\end{aligned} \tag{B.22}$$

where k is defined as before. Thus applying the DFT to equation (B.18) with respect to ξ and denoting the nonlinear terms as $II_\xi = (z_a)_\xi = \left(\frac{(I)^2}{2}\right)_\xi$ and $SS_\xi = (z_b)_\xi = \left(\frac{(S)^2}{2}\right)_\xi$, we obtain

$$\begin{aligned}\hat{I}_X - \alpha_1 isk\hat{z}_a - \beta_1 is^3k^3\hat{I} = -\frac{i}{sk}\left(\hat{I} - \hat{S}\right),\\ \text{and } \hat{S}_X + isk\omega\hat{S} - \alpha_2 isk\hat{z}_b - \beta_2 is^3k^3\hat{S} = -\frac{i}{sk}\left(\hat{S} - \hat{I}\right).\end{aligned} \tag{B.23}$$

These can be used to find the functions F_i for $i = 1, 2$ as

$$F_1 = \hat{I}_X = -\frac{i}{sk}\left(\hat{I} - \hat{S}\right) + \alpha_1 isk\hat{z}_a + \beta_1 is^3k^3\hat{I}, \tag{B.24}$$

$$\text{and } F_2 = \hat{S}_X = -\frac{i}{sk}\left(\hat{S} - \hat{I}\right) - isk\omega\hat{S} + \alpha_2 isk\hat{z}_b + \beta_2 is^3k^3\hat{S}. \tag{B.25}$$

Next, applying the Runge-Kutta 4th-order method as before, we assume $\hat{I}_j = I(k, \Delta X)$ and $\hat{S}_j = S(k, \Delta X)$ represent the solutions at step X. Therefore, solution at $X = (j+1)\Delta X$ is given by

$$\begin{aligned}\hat{I}_{k,(j+1)\Delta X} = \hat{I}_{k,j\Delta X} + \frac{1}{6}\left(a_1 + 2b_1 + 2c_1 + d_1\right),\\ \hat{S}_{k,(j+1)\Delta X} = \hat{S}_{k,j\Delta X} + \frac{1}{6}(a_2 + 2b_2 + 2c_2 + d_2),\end{aligned} \tag{B.26}$$

where a_i, b_i, c_i and d_i are functions of ξ at time X and are defined as

$$\begin{aligned} a_i &= \Delta X F_i\left(\hat{I}_{k,j\Delta T}, \hat{S}_{k,j\Delta T}\right), \quad b_i = \Delta X F_i\left(\hat{I}_{k,j\Delta T} + \frac{a_1}{2}, \hat{S}_{k,j\Delta T} + \frac{a_2}{2}\right), \\ c_i &= \Delta X F_i\left(\hat{I}_{k,j\Delta T} + \frac{b_1}{2}, \hat{S}_{k,j\Delta T} + \frac{b_2}{2}\right), \quad d_i = \Delta X F_i\left(\hat{I}_{k,j\Delta T} + c_1, \hat{S}_{k,j\Delta T} + c_2\right). \end{aligned} \tag{B.27}$$

In summary, we have successfully extended the pseudospectral scheme for the KdV equation, single Ostrovsky equation, and coupled Ostrovsky equations by applying the DFT and the Runge-Kutta 4th-order method. This enabled us to derive solutions at each time step for the wave dynamics in the various structures explored in this thesis.

Bibliography

[1] J. S. Russell. Report of the fourteenth meeting of the British Association for the Advancement of Science. *London*, 1844.

[2] J. S. Russell. *The Wave of Translation in the Oceans of Water, Air, and Ether*. Trübner & Company, 1885.

[3] J. S. Russell. V. The Wave of Translation and the work It Does as the Carrier Wave of Sound. *Proceedings of the Royal Society of London*, 32(212-215):382–383, 1881.

[4] E. Olivier. *Report to the French Academy of Sciences on the Portion of Bazin's Treatise Relating to Surges and the Propagation of Waves*. Royal Institute of Engineers, 1869.

[5] J. V. Boussinesq. Théorie des ondes et des remous qui se propagent le long d'un canal rectangulaire horizontal, en communiquant au liquide contenu dans ce canal des vitesses sensiblement pareilles de la surface au fond. *J. Math. Pures Appl., ser. (2)*, 17:55–108, 1872.

[6] J. V. Boussinesq. Essai sur la théorie des eaux courantes. mémoires présentés par divers savants á l'Académie des Sciences. *Inst. NAT. France*, XXIII:1–660, 1877.

[7] Lord J. W. S. Rayleigh. On Waves. *Phil. Mag.*, 1:257–279, 1876.

[8] A. J. C. Saint-Venant. Théorie du mouvement non permanent des eaux, avec application aux crues des rivières et à l'introduction de marées dans leurs lits. *Comptes Rendus de l'Académie des Sciences*, 73:147–154, 237–240, 1871.

[9] E. Fermi, J. Pasta, and S. Ulam. Studies on nonlinear problems. *I. Los Alamos Scientific Laboratory*, LA-1940, 1955.

[10] T. Dauxois and S. Ruffo. Fermi-Pasta-Ulam nonlinear lattice oscillations. *Scholarpedia*, 3(8):5538, 2008.

[11] N. J. Zabusky and M. D. Kruskal. Interaction of "Solitons" in a Collisionless Plasma and the Recurrence of Initial States. *Phys. Rev. Lett.*, 15:240–243, 1965.

[12] C. S. Gardner, J. M. Greene, M. D. Kruskal, and R. M. Miura. Method for solving the Korteweg-de Vries equation. *Phys. Rev. Lett.*, 19:1095–1097, 1967.

[13] P. D. Lax. Integrals of nonlinear equations of evolution and solitary waves. *Commun. Pur. Appl. Math.*, pages 467–490, 1968.

[14] A. M. Krall and A. M. Krall. Hilbert Spaces. *Applied Analysis*, pages 127–157, 1986.

[15] V. E. Zakharov and A. B. Shabat. Exact theory of two-dimensional self-focusing and one-dimensional self-modulation of waves in nonlinear media. *Sov. Phys. JETP*, 34:62–69, 1972.

[16] M. J. Ablowitz, D. J. Kaup, A. C. Newell, and H. Segur. The Inverse Scattering Transform-Fourier Analysis for Nonlinear Problems. *Studies in Applied Mathematics*, 53(4):249–315, 1974.

[17] A. V. Bäcklund. On the Theory of Surface Transformations. *Mathematische Annalen*, 19(3):387–422, 1881.

[18] M. J. Ablowitz and H. Segur. *Solitons and the Inverse Scattering Transform*. Studies in Applied and Numerical Mathematics. Society for Industrial and Applied Mathematics, 2006. URL: `https://books.google.co.uk/books?id=Bzu4XAUpFZUC`.

[19] M. Toda. Vibration of a Chain with Nonlinear Interaction. *Journal of the Physical Society of Japan*, 22:431–436, 1967.

[20] D. Yagi and T. Kawahara. Strongly nonlinear envelope soliton in a lattice model for periodic structure. *Wave Motion*, 34:97–107, 2001.

[21] T. Gerkema. A unified model for the generation and fission of internal tides in a rotating ocean. *J. Marine Res.*, 54:421–450, 1996.

[22] L. A. Ostrovskii and A. M. Sutin. Nonlinear elastic waves in rods. *J. Appl. Math. Mech.*, 41:543–549, 1977.

[23] L. A. Ostrovsky. Nonlinear internal waves in a rotating ocean. *Oceanology*, 18:119–125, 1978.

[24] R. Grimshaw et al. Long Nonlinear Surface and Internal Gravity Waves in a Rotating Ocean. *Surveys in Geophysics*, 19:289–338, 1998. `doi:10.1023/A:1006587919935`.

[25] A. I. Leonov. The effect of the earth's rotation on the propagation of weak nonlinear surface and internal long oceanic waves. *Ann. NY Acad. Sci.*, 373:150–159, 1981.

[26] R. H. G. Grimshaw, E. Pelinovsky, and T. Talipova. Fission of a weakly nonlinear interfacial solitary wave at a step. *Geophys. Astrophys. Fluid Dyn.*, 102:179–194, 2008.

[27] K. R. Helfrich. Decay and return of internal solitary waves with rotation. *Phys. Fluids*, 19:026601, 2007.

[28] K. R. Khusnutdinova. Coupled Klein-Gordon equations and energy exchange in two-component systems. *Eur. Phys. J.*, 147:45–72, 2007.

[29] K. R. Khusnutdinova, A. M. Samsonov, and A. S. Zakharov. Nonlinear layered lattice model and generalized solitary waves in imperfectly bonded structures. *Phys. Rev. E*, 79:056606, 2009.

[30] A. Askar. *Lattice Dynamical Foundations of Continuum Theories*. World Scientific, Singapore, 1985.

[31] E. A. Il'yushina. *Towards Formulation of Elasticity Theory of Inhomogeneous Solids with Microstructure*. PhD thesis, Lomonosov Moscow State University, 1976. (in Russian).

[32] A. M. Samsonov. *Strain Solitons in Solids and How to Construct Them*. CRC Press, 2001.

[33] A. V. Porubov. *Amplification of Nonlinear Strain Waves in Solids*. World Scientific, 2003.

[34] N. Peake and S. V. Sorokin. A nonlinear model of the dynamics of a large elastic plate with heavy fluid loading. *P. Roy. Soc. A*, 462:2205–2224, 2006.

[35] D. A. Indejtsev, M. G. Zhuchkova, D. P. Kouzov, and S. V. Sorokin. Low-frequency wave propagation in an elastic plate floating on a two-layered fluid. *Wave Motion*, 62:98–113, 2016.

[36] T. Peets, K. Tamm, and J. Engelbrecht. On the role of nonlinearities in the boussinesq-type wave equations. *Wave Motion*, 71:113–119, 2017.

[37] Z. Abiza, M. Destrade, and R. W. Ogden. Large acoustoelastic effect. *Wave Motion*, 49(2):364–374, 2012.

[38] I. V. Andrianov, A. I. Manevich, Y. V. Mikhlin, and O. V. Gendelman. *Problems of Nonlinear Mechanics and Physics of Materials*. Springer, 1st edition, 2019.

[39] F. E. Garbuzov, K. R Khusnutdinova, and I. V. Semenova. On Boussinesq-type models for long longitudinal waves in elastic rods. *Wave Motion*, 88:129–143, 2019.

[40] G. A. Nariboli and A. Sedov. Burgers's-Korteweg-De Vries equation for viscoelastic rods and plates. *J. Math. Anal. Appl.*, 32:661–677, 1970.

[41] H. H. Dai and X. Fan. Asymptotically approximate model equations for weakly nonlinear long waves in compressible elastic rods and their comparisons with other simplified model equations. *Mathematics and Mechanics of Solids*, 9(1):61–79, 2004.

[42] V. I. Erofeev and N. V. Klyueva. Solitons and nonlinear periodic strain waves in rods, plates, and shells (a review). *Acoustical Physics*, 48(6):643–655, 2002.

[43] V. I. Erofeev, A. V. Leontieva, A. O. Malkhanov, and A. V. Shekoyan. Nonlinear longitudinal magnetoelastic waves in a rod with account of damage in its material. *Materials Physics and Mechanics*, 35(1):44–52, 2018.

[44] G. V. Dreiden, K. R. Khusnutdinova, A. M. Samsonov, and I. V. Semenova. Splitting induced generation of soliton trains in layered waveguides. *J. Appl. Phys.*, 107:034909, 2010.

[45] K. R. Khusnutdinova and A. M. Samsonov. Fission of a longitudinal strain solitary wave in a delaminated bar. *Phys. Rev. E*, 77:066603, 2008.

[46] G. V. Dreiden, K. R. Khusnutdinova, A. M. Samsonov, and I. V. Semenova. Bulk strain solitary waves in bonded layered polymeric bars with delamination. *J. Appl. Phys.*, 112:063516, 2012.

[47] K. R. Khusnutdinova and M. R. Tranter. Modelling of nonlinear wave scattering in a delaminated elastic bar. *P. Roy. Soc. A*, 471(2183):20150584, 2015.

[48] K. R. Khusnutdinova and M. R. Tranter. On radiating solitary waves in bi-layers with delamination and coupled Ostrovsky equations. *Chaos*, 27:013112, 2017.

[49] A. V. Belashov et al. Indirect assessment of bulk strain soliton velocity in opaque solids. *Applied Physics Letters*, 112(12), 2018.

[50] P. D. Weidman et al. Linear Waves and Nonlinear wave Interactions in a Bounded Three-Layer Fluid System. *Stud. Appl. Math.*, 128(4):385–406, 2011.

[51] M. J. Ablowitz. *Nonlinear dispersive waves: asymptotic analysis and solitons.* Cambridge University Press, 2011.

[52] M. J. Ablowitz and H. Segur. *Solitons and the Inverse Scattering Transform.* SIAM, 1981.

[53] P. G. Drazin and R. S. Johnson. *Solitons: An Introduction.* Cambridge University Press, 1989.

[54] R. H. J. Grimshaw. *Solitary Waves in Fluids*. WIT Press, Southampton, 2007.

[55] A. C. Newell. *Solitons in Mathematics and Physics*. SIAM, Philadelphia, 1985.

[56] J. Sherman and W. J. Morrison. Adjustment of an inverse matrix corresponding to a change in one element of a given matrix. *Ann. Math. Statist.*, 21(1):124–127, 1950.

[57] G. B. Whitham. *Linear and Nonlinear Waves*. Wiley, New York, 1974.

[58] A. Karczewska, P. Rozmej, and E. Infeld. Shallow-water soliton dynamics beyond the Korteweg–de Vries equation. *Phys. Rev. E*, 90:012907, 2014.

[59] T. B. Benjamin. Internal waves of permanent form in fluids of great depth. *J. Fluid Mech.*, 29:559–592, 1967.

[60] H. Ono. Algebraic solitary waves in stratified fluids. *J. Phys. Soc. Japan*, 39:1082–1091, 1975.

[61] G. I. Stegeman and M. Segev. Optical Spatial Solitons and Their Interactions: Universality and Diversity. *Science*, 286:1518–1523, 1999.

[62] J. Yang. *Nonlinear Waves in Integrable and Nonintegrable Systems*. SIAM, 2010.

[63] A. R. Champneys, P.J. McKenna, and P.A. Zegeling. Solitary Waves in Nonlinear beam equations: Stability, fission and fusion. *Nonlinear Dyn.*, 21:31–53, 2000.

[64] Q. Gong et al. Fracture and Delamination Assessment of Prestressed Composite Concrete for Use with Pipe Jacking Method. *Math. Probl. Eng.*, 2015:1–11, 2015.

[65] M. Yatomi and K.M. Nikbin. Sensitivity analysis of creep crack growth prediction using the statistical distribution of uniaxial data. *Fatigue Fract Eng M*, 2010.

[66] G. V. Dreiden, K. R. Khusnutdinova, A. M. Samsonov, and I. V. Semenova. Comparison of the effect of cyanoacrylate- and polyurethane-based adhesives on a longitudinal strain solitary wave in layered polymethylmethacrylate waveguides. *J. Appl. Phys.*, 104:086106, 2008.

[67] G. V. Dreiden, A. M. Samsonov, I. V. Semenova, and K. R. Khusnutdinova. Observation of a radiating bulk strain soliton in a solid-state waveguide. *Tech. Phys.*, 56:889–892, 2011.

[68] G. V. Dreiden, A. M. Samsonov, I. V. Semenova, and A. G. Shvartz. Strain solitary waves in a thin-walled waveguide. *Appl. Phys. Lett.*, 105:211906, 2014.

[69] R. H. J. Grimshaw, K. R. Khusnutdinova, and K. R. Moore. Radiating solitary waves in coupled Boussinesq equations. *IMA J. Appl. Math.*, 82:802–820, 2017.

[70] R. H. J. Grimshaw and K. R. Helfrich. The effect of rotation on internal solitary waves. *IMA J. Appl. Math.*, 77:326–339, 2012.

[71] M. R. Tranter. *Mathematical modelling of nonlinear waves in layered waveguides with delamination.* Thesis, Loughborough University, 2018.

[72] K. R. Khusnutdinova and K. R. Moore. Initial-value problem for coupled Boussinesq equations and a hierarchy of Ostrovsky equations. *Wave Motion*, 48:738–752, 2011.

[73] K. R. Moore. *Coupled Boussinesq equations and nonlinear waves in layered waveguides.* PhD thesis, PhD Thesis, Loughborough University, 2013.

[74] A. Alias, R. H. J. Grimshaw, and K. R. Khusnutdinova. On strongly interacting internal waves in a rotating ocean and coupled Ostrovsky equations. *Chaos*, 23(2):023121, 2013.

[75] R. H. J. Grimshaw and Y. A. Stephanyants. Emergence of Envelope Solitary Waves from Initial Localized Pulses within the Ostrovsky Equation. *Radiophys. Quantum. El*, 63:21–28, 2020.

[76] K. R. Khusnutdinova and M. R. Tranter. Periodic solutions of coupled Boussinesq equations and Ostrovsky-type models free from zero-mass contradiction. *Chaos*, 32:113132, 2022.

[77] M. R. Tranter. Solitary wave propagation in elastic bars with multiple sections and layers. *Wave Motion*, 86:21–31, 2019.

[78] I. S. Akhatov, V. A. Baikov, and K. R. Khusnutdinova. Non-linear dynamics of coupled chains of particles. *Journal of Applied Mathematics and Mechanics*, 59(3):353–361, 1995.

[79] I. Lurie. *Nonlinear Theory of Elasticity.* Elsevier, Amsterdam, 1990.

[80] F. D. Murnaghan. *Finite Deformations of an Elastic Solid.* Wiley, New York, 1951.

[81] A. E. H. Love. *Nonlinear Ocean Waves.* Dover, New York, 1944.

[82] E. Volterra. The equations of motions for curved and twisted elastic bar deduced by the use of the "method of internal constraints". *Ing. Arch.*, 24:392–400, 1956.

[83] E. Volterra and E. C. Zachmanoglou. *Dynamics of Vibrations.* Merrill, Columbus, 1965.

[84] H. N. Abramson, H. J. Plass, and E. A. Ripperger. Stress wave propagation in rods and beams. *Adv. Appl. Mech.*, 5:111–194, 1958.

[85] E. I. Grigolyuk and I. T. Selezov. *Non-Classical Theories of Vibrations of Rods, Plates and Shells.* VINITI, Moscow, 1973.

[86] J. W. Miles. Resonantly interacting solitary waves. *J. Fluid Mech.*, 79(1):171–179, 1977.

[87] T. B. Benjamin, J. L. Bona, and J. J. Mahony. Model equations for long waves in nonlinear dispersive systems. *Philos. Trans. R. Soc. Lond. A*, 272:47–48, 1972.

[88] M. A. Christou and C. I. Christov. Interacting localized waves for the regularized long wave equation via a Galerkin spectral method. *Math. Comp. Sim.*, 69:257–268, 2005.

[89] J. L. Bona, T. Colin, and D. Lannes. Long wave approximations for water waves. *Arch. Ration. Mech.*, 178:373–410, 2005.

[90] W. B. Youssef and T. Colin. Rigorous derivation of Korteweg-de Vries-type systems from a general class of nonlinear hyperbolic systems. *ESAIM: M2AN*, 34:873–911, 2000.

[91] K. R. Khusnutdinova and K. R. Moore. Weakly nonlinear extension of d'Alembert's formula. *IMA J. Appl. Math.*, 77:361–381, 2012.

[92] C. Köroğlu and T. Özis. A novel traveling wave solution for Ostrovsky equation using Exp-function method. *Comput. Math. Appl.*, 58(11-12):2142–2146, 2009. doi:10.1016/j.camwa.2009.06.026.

[93] J. S. Tamber and M. R. Tranter. Scattering of an Ostrovsky wave packet in a delaminated waveguide. *Wave Motion*, 114:103023, 07 2022.

[94] K. R. Khusnutdinova and M. R. Tranter. D'alembert-type solution of the cauchy problem for the boussinesq-klein-gordon equation. *Stud. Appl. Math.*, 142:551–585, 2019.

[95] K. R. Khusnutdinova and M. R. Tranter. Weakly-nonlinear solution of coupled Boussinesq equations and radiating solitary waves. In H. Altenbach, A. Belyaev, V. Eremeyev, A. Krivtsov, and A. Porubov, editors, *Dynamical Processes in Generalized Continua and Structures*, chapter 18, pages 321–343. Springer, 2019.

[96] K. R. Khusnutdinova, K. R. Moore, and D. E. Pelinovsky. Validity of the weakly nonlinear solution of the Cauchy problem for the Boussinesq-type equation. *Stud. Appl. Math.*, 133:52–83, 2014.

[97] J. Stoer and R. Bulirsch. *Introduction to Numerical Analysis*. Springer-Verlag, New York, 1980.

[98] L. D. Landau and E. M. Lifshitz. *Quantum Mechanics: Non-Relativistic Theory*. Elsevier Science, 2013.

[99] G. V. Dreiden, K. R. Khusnutdinova, A. M. Samsonov, and I. V. Semenova. Longitudinal Strain Solitary Wave in a Two-Layered Polymeric Bar. *Strain*, 46:589–598, 2010.

[100] G. V. Dreiden, A. M. Samsonov, and I. V. Semenova. Bulk Elastic Strain Solitons in Polycarbonate. *Tech. Phys. Lett.*, 37:500–502, 2011.

[101] A. M. Samsonov, I. V. Semenova, and A. V. Belashov. Direct determination of bulk strain soliton parameters in solid polymeric waveguides. *Wave Motion*, 71:120–126, 2017.

[102] J. S. Tamber, D. J. Chappell, and M. R. Tranter. Delamination detection in layered waveguides using ostrovsky wave packets. *Proceedings of the Royal Society A: Mathematical, Physical and Engineering Sciences*, 481:20240574, 2025.

[103] J. S. Tamber, D. J. Chappell, J. C. Poore, and M. R. Tranter. Detecting delamination via nonlinear wave scattering in a bonded elastic bar. *Nonlinear Dyn.*, 112:23–33, 2024. doi: 10.1007/s11071-023-08992-9.

[104] W. F. Ames. *Numerical Methods for Partial Differential Equations*. Academic Press, Inc., 2nd edition, 1977.

[105] J. W. Cooley and J. W. Tukey. An algorithm for the machine calculation of complex Fourier series. *Math. Comput.*, 19:297–301, 1965.